Doctoral Dissertation
Doctoral Program in Mechanical Engineering (36th Cycle)

Passive upper-limb exoskeleton based on Pneumatic Artificial Muscles

Maria Paterna
* * * * * *

Supervisors
Prof. Carlo Ferraresi, Supervisor
Prof. Daniela Maffiodo, Co-Supervisor
Prof. Walter Franco, Co-Supervisor

Politecnico di Torino
May 03, 2024

I hereby declare that, the contents and organisation of this dissertation constitute my own original work and does not compromise in any way the rights of third parties, including those relating to the security of personal data.

Maria Paterna
Turin, May 03, 2024

Summary

The thesis aims to describe a new passive upper-limb exoskeleton for industrial application. These devices can improve the workers' comfort and productivity by reducing muscle activity and intra-articular compressive force during overhead work. Passive industrial exoskeletons presented in literature or commercially available typically employ a spring-based mechanism to balance the gravitational torque acting on the shoulder. As an alternative, the exoskeleton described in this thesis aims to exploit the elastic characteristics of artificial pneumatic muscles (PAMs). The latter have several features that make their use within the exoskeleton structure fascinating: their intrinsic deformability and similarity to the skeletal muscles allow a safe human-exoskeleton interaction; in addition, PAMs have a high power-to-weight ratio and are easy to install, so they do not increase the bulkiness and the weight of the system; finally, the availability of PAMs with different sizes, characteristics, and load capabilities, as well as the possibility to regulate the internal pressure, allow for extensive customization of the actuator's response that can match several applications and working conditions. The final device shall also ensure an upper limb range of movement appropriate to its intended use, human-exoskeleton interaction forces less than the limits of safety and comfort, and a set of size regulations that allow adjusting the exoskeleton to fit users with different physical characteristics.

After a brief introduction to the physiological and biomechanical aspects of the shoulder joint and an overview of the state of the art of upper limbs industrial exoskeletons (Chapter 1), the thesis describes the design process of a PAMs-based exoskeleton prototype. Chapter 2 presents the mathematical model used to identify the type of PAM and the motion transmission that minimizes the mismatch between the gravitational torque acting on the shoulder and the support torque provided by the exoskeleton in a workspace suitable for most work tasks. Then, the kinematic chain design that allows the flexion-extension and abduction-adduction of the arm

is described in Chapter 3, and the effect of the possible misalignment between the exoskeleton and shoulder joint centers on the performance of the exoskeleton is discussed. In Chapter 4, the exoskeleton architecture is presented, together with the results of the analytical model used for the human-exoskeleton interaction forces estimation and the finite element static analysis. Analytical and numerical analyses demonstrated the exoskeleton feasibility and led to the development of a prototype of about 5.5 kg suitable for users with a height between 160 cm and 175 cm. Finally, the prototype is validated by bench tests (Chapter 5) and experimental laboratory tests involving voluntary subjects to perform static and dynamic tasks (Chapter 6). Validation tests showed that the exoskeleton can adequately support the user during overhead tasks. A shoulder muscle activity reduction of up to 75% has been detected, while there is no evident increase in lumbar muscle activity due to the transfer of loads by the exoskeleton. Moreover, subjects did not declare discomfort due to excessive pressure applied by the exoskeleton on the user's body.

Contents

1. Introduction....1

1.1 Shoulder biomechanics....2

1.1.1 Structure of the shoulder....2
1.1.2 Shoulder kinematics....3
1.1.2 Shoulder kinetics....7

1.2 Exoskeleton for overhead work....9

1.2.1 Design Features....9
1.2.2 Active exoskeletons....11
1.2.3 Passive exoskeletons....12

1.3 Pneumatic Artificial Muscle....16
1.4 Exoskeleton performance metrics....19
1.5 The aim of this work....22

2. Design of the torque generator....23

2.1 McKibben Muscle....24
2.2 Configuration A: pulley-based mechanism.....25
2.3 Configuration B: shoulder pad-based mechanism.....27
2.4 Configuration C: cam-based mechanism....29
2.5 Simulation results....32

2.5.1 Configuration A: pulley-based transmission....32
2.5.2 Configuration B: shoulder-pad-based transmission....34
2.5.3 Configuration C: cam-based transmission....36
2.5.4 Conclusion....38

2.6 PAM static experimental characteristic....38
2.7 Workspace evaluation....42

3. The kinematic chain....45

3.1 Joint misalignment....45
3.2 Exoskeleton joints mechanical design....51

4. Assembly of the exoskeleton 55
4.1 Architecture of the exoskeleton 56
4.2 Human-exoskeleton interaction force 58
4.2.1 Exo-arm 59
4.2.2 Back Frame 62
4.2.3 Contact pressure estimation 64
4.3 FEM structural analysis 66
4.3.1 Exo-arm structural analysis 67
4.3.2 Back frame structural analysis 73
4.4 Exoskeleton size 77
5. Test-bench analyses 79
6. Experimental validation 83
6.1 Data recording 83
6.1.1 EMG data 83
6.1.2 Kinematics data 86
6.1.3 Balance performance 96
6.2 Experimental protocol 97
6.3 Results 101
6.3.1 Exoskeleton assistive ability 101
6.3.2 Side effects 103
6.3.3 Kinematic matching 105
6.4 Discussion 106
6.4.1 Limitations of the experimental trials 107
7. Conclusion 109
8. References 111
9. Appendix A: markers trajectories post-processing algorithm 121

List of Tables

TABLE 1.1 PHYSIOLOGICAL MOVEMENTS OF THE UPPER ARM. 4
TABLE 1.2 SHOULDER MUSCLES ACTION 5
TABLE 1.3 ANTHROPOMETRIC DATA USED TO ESTIMATE THE JOINT TORQUE VALUES SHOWN IN FIGURE 1.5. EJC AND WJC REPRESENT THE ELBOW AND WRIST JOINT CENTERS, RESPECTIVELY, WHEREAS CoM_2 AND CoM_3 ARE THE CENTER OF MASS OF THE FOREARM AND HAND, RESPECTIVELY. 9
TABLE 2.1 TECHNICAL DATA OF COMMERCIAL FESTO MCKIBBEN MUSCLES. 24
TABLE 2.2 COEFFICIENT OF EQUATION 1.9 FOR APPROXIMATING THE STATIC CHARACTERISTICS OF COMMERCIAL FESTO MCKIBBEN MUSCLES. 25
TABLE 2.3 A AND A TESTED VALUES. 33
TABLE 2.4 STATIC CHARACTERIZATION DATA. M IS THE EXTERNAL LOAD; P IS THE SUPPLY PRESSURE; KS AND KD ARE THE CONTRACTION RATIO MEASURED DURING THE UP AND DOWN PRESSURE CYCLE, RESPECTIVELY. 40
TABLE 2.5 COEFFICIENT OF EQUATION 1.9 FOR APPROXIMATING THE EXPERIMENTAL STATIC CHARACTERISTICS OF COMMERCIAL FESTO MCKIBBEN MUSCLES (DMSP-10-350N-RM-CM) 41
TABLE 4.1 YOUNG'S MODULUS (E), POISSON'S RATIO (N), SHEAR MODULUS (G), YIELD STRENGTH (S_Y) AND ULTIMATE TENSILE STRENGTH (S_{UT}) OF THE IDENTIFIED MATERIALS. 67
TABLE 4.2 REACTION FORCES BETWEEN EXO-ARMS AND BACK FRAME. 73
TABLE 5.1 STATIC CHARACTERIZATION DATA. M IS THE EXTERNAL LOAD; P IS THE SUPPLY PRESSURE; K IS THE MKM CONTRACTION RATIO; F_{MKM} IS THE MKM TRACTION FORCE; Θ IS THE EXOSKELETON FLEXION ANGLE, ... 80
TABLE 6.1 MEAN SQUARE ERROR BETWEEN THE RECONSTRUCTED AND ACQUIRED TRAJECTORIES OF THE MARKER C7, RSHO, AND RELB 92
TABLE 6.2 SUBJECTS ANTHROPOMETRIC CHARACTERISTICS. R AND L APICES REFER TO THE RIGHT AND LEFT ARM, RESPECTIVELY. 97
TABLE 6.3 SHOULDER FLEXION AND ABDUCTION ANGLES MEASURED DURING STATIC TASK. POSITIVE VALUES INDICATE FLEXED AND ABDUCTED POSITION, WHILE NEGATIVE VALUES INDICATE EXTENDED AND ADDUCTED POSITION. 101
TABLE 6.4 DYNAMIC TEST WORKSPACE. 103
TABLE 6.5 SJC – EXOJC MISALIGNMENT IN THE ARM ELEVATION PLANE. POSITIVE VALUES INDICATE FORWARD AND UPPER DISPLACEMENT OF SJC WITH RESPECT EXOJC. 105

List of Figures

FIGURE 1.1 SHOULDER JOINT ANATOMY [26]..... 3
FIGURE 1.2 UPPER-ARM MOVEMENT. (A) EXTENSION-FLEXION; (B) ABDUCTION-ADDUCTION; (C) HORIZONTAL ABDUCTION-ADDUCTION; (D) MEDIAL-LATERAL ROTATION 4
FIGURE 1.3 SUPERFICIAL (A) AND DEEP (B) SHOULDER MUSCLES ILLUSTRATION. 5
FIGURE 1.4 SJC POSITION WITH RESPECT TO SC JOINT IN THE FRONTAL PLANE DURING ARM ELEVATION. DATA ARE ESTIMATED FOR A MAN OF 1.7 M. 7
FIGURE 1.5 GRAVITATIONAL TORQUE ON SHOULDER JOINT CENTER WITH RESPECT TO THE ELEVATION ANGLE OF THE UPPER ARM Θ_1 AND THE FOREARM FLEXION ANGLE Θ_2. SJC, EJC, AND WJC REPRESENT THE GLENOHUMERAL JOINT CENTER, THE ELBOW JOINT CENTER, AND THE WRIST JOINT CENTER RESPECTIVELY, WHEREAS CoM_1, CoM_2, AND CoM_3 ARE THE CENTERS OF MASS OF THE UPPER ARM, FOREARM, AND HAND. 8
FIGURE 1.6 ELECTRIC ACTIVE EXOSKELETONS PROTOTYPES [17, 59]. 11
FIGURE 1.7 THE DOUBLE PARALLELOGRAM LINKAGE DEVELOPED BY BAI ET AL [16]. 12
FIGURE 1.8 PASSIVE UPPER LIMB EXOSKELETONS. (A) PAEXO (OTTOBOCK, GERMANY) [22]; (B) MATE (COMAU, ITALY) [HTTPS://WWW.COMAU.COM/EN]; (C) H-VEX (HYUNDAI, SOUTH KOREA) [73]. 13
FIGURE 1.9 (A) MCKIBBEN MUSCLE; (B) STRAIGHT FIBERS MUSCLE; (C) BI-DIRECTIONAL ACTUATOR; (D) BENDING PNEUMATIC ACTUATOR; (E) AIR-POCKET; (F) BELLOW MUSCLE. [95] 16
FIGURE 1.10 MCKIBBEN'S TRACTION FORCE FOR DIFFERENT: (A) SUPPLY PRESSURE P [0.5; 1; 1.5; 2; 2.5] BAR; (B) WINDING ANGLE A OF THE INEXTENSIBLE FIBERS [45; 50; 55; 60; 65]°; (C) THICKNESS S OF THE INFLATABLE CHAMBER [1; 2; 3; 4; 5] MM. IN THE GRAPH, R_0 IS THE RESTING RADIUS, K IS THE CONTRACTION RATIO, AND THE MKM NOMINAL LENGTH IS 0.2 M. [95] 17
FIGURE 1.11 PASSIVE WALKING-ASSIST EXOSKELETON [102]. 18
FIGURE 1.12 EMG PROCESSING STEPS. 20
FIGURE 2.1 STATIC CHARACTERISTICS OF MCKIBBEN MUSCLES: DMSP-10 (A); DMSP-20 (B). 25
FIGURE 2.2 SCHEME OF THE PULLEY-BASED CONFIGURATION 26
FIGURE 2.3 SCHEME OF THE SHOULDER PAD-BASED CONFIGURATION 27
FIGURE 2.4 (A) SHOULDER-PAD PROFILE; (B) MKM FORCE LEVER ARM. RED DOTS REPRESENT THE DATA EXTRAPOLATED FROM THE CAD WHILE THE BLACK LINE IS THE RESULT OF RED DOTS INTERPOLATION. 29
FIGURE 2.5 CAM-BASED TRANSMISSION FOR DIFFERENT SHOULDER-FLEXION ANGLES: (A) $\Theta_1 = 135°$; (B) $\Theta_1 = 90°$; (C) $\Theta_1 = 45°$. 30
FIGURE 2.6 GRAPHICAL APPROACH TO DESIGN THE CAM PROFILE. 31

FIGURE 2.7 CAM PROFILE (A) ALONG WITH THE MKM FORCE LEVER ARM (B). THE RED DOTS ARE THE DATA EXTRAPOLATED FROM THE CAD WHILE THE BLACK LINE IS THE RESULT OF RED DOTS INTERPOLATION. 31
FIGURE 2.8 ROOT MEAN SQUARE ERROR BETWEEN THE GRAVITATIONAL TORQUE AND THE TORQUE GENERATED BY THE DMSP-10 (A), AND THE DMSP-20 (B) FOR DIFFERENT PARAMETER CONFIGURATIONS. DATA REFER TO THE PULLEY-BASED DESIGN OF THE TRANSMISSION SYSTEM. 34
FIGURE 2.9 GRAVITATIONAL TORQUE IN NO-LOAD (BLACK LINE), 1 KG LOAD (DASHED BLACK LINE), AND 2 KG LOAD (DOT-DASHED BLACK LINE) CONDITION AS WELL AS THE TORQUE EXERTED BY THE EXOSKELETON AT DIFFERENT SUPPLY PRESSURES (COLORED LINES) BY EMPLOYING THE DMSP-10 MKM AND THE PULLEY-BASED DESIGN OF THE TRANSMISSION. 34
FIGURE 2.10 ROOT MEAN SQUARE ERROR BETWEEN THE GRAVITATIONAL TORQUE AND THE TORQUE GENERATED BY THE DMSP-10 (A), AND THE DMSP-20 (B) FOR DIFFERENT PARAMETER CONFIGURATIONS. DATA REFERS TO THE CAM-BASED DESIGN OF THE TRANSMISSION SYSTEM..... 35
FIGURE 2.11 GRAVITATIONAL TORQUE IN NO-LOAD (BLACK LINE), 1 KG LOAD (DASHED BLACK LINE), AND 2 KG LOAD (DOT-DASHED BLACK LINE) CONDITION AS WELL AS THE TORQUE EXERTED BY THE EXOSKELETON AT DIFFERENT SUPPLY PRESSURES (COLORED LINES) BY EMPLOYING THE DMSP-10 MUSCLE AND THE SHOULDER PAD-BASED DESIGN OF THE TRANSMISSION. 36
FIGURE 2.12 ROOT MEAN SQUARE ERROR BETWEEN THE GRAVITATIONAL TORQUE AND THE TORQUE GENERATED BY THE DMSP-10 (A), AND THE DMSP-20 (B) FOR DIFFERENT PARAMETER CONFIGURATIONS. DATA REFERS TO THE CAM-BASED DESIGN OF THE TRANSMISSION..... 37
FIGURE 2.13 GRAVITATIONAL TORQUE IN NO-LOAD (BLACK LINE), 1 KG LOAD (DASHED BLACK LINE), AND 2 KG LOAD (DOT-DASHED BLACK LINE) CONDITION AS WELL AS THE TORQUE EXERTED BY THE EXOSKELETON AT DIFFERENT SUPPLY PRESSURES (COLORED LINES) BY EMPLOYING THE DMSP-10 MKM AND THE CAM-BASED TRANSMISSION..... 37
FIGURE 2.14 SKETCH OF THE TEST BENCH DEVELOPED TO CHARACTERIZE THE MKM. 39
FIGURE 2.15 (A) FESTO DMSP-10-350N-RM-CM EXPERIMENTAL STATIC CHARACTERISTIC (B) MKM HYSTERESIS ERROR EXPRESSED AS A PERCENTAGE OF THE CONTRACTION RATIO RANGE..... 41
FIGURE 2.16 MATHEMATICAL INTERPOLATION OF THE FESTO MCKIBBEN MUSCLES EXPERIMENTAL STATIC CHARACTERISTIC..... 41
FIGURE 2.17 GRAVITATIONAL TORQUE IN NO-LOAD (BLACK LINE), 1 KG LOAD (DASHED BLACK LINE), AND 2 KG LOAD (DOT-DASHED BLACK LINE) CONDITION AS WELL AS THE TORQUE EXERTED BY THE EXOSKELETON AT DIFFERENT SUPPLY PRESSURES (COLOURED LINES) BY EMPLOYING THE MKM EXPERIMENTAL CHARACTERISTIC AND THE SHOULDER PAD-BASED DESIGN OF THE TRANSMISSION. 42
FIGURE 2.18 PERCENTAGE OF THE GRAVITATIONAL TORQUE PROVIDED BY THE EXOSKELETON IN THE UNLOADED CONDITION (A) AND WITH 1 KG (B) AND 2 KG (C) IN THE HAND. THE MKM SUPPLY PRESSURE IS EQUAL TO 4.3 BAR (A), 6 BAR (B), AND 7.7 BAR (C). BLACK DOTS REPRESENT THE STATIC EQUILIBRIUM IN WHICH THE EXOSKELETON PROVIDES 100% OF THE TORQUE NEEDED TO KEEP THE ARM IN THAT POSITION. 43
FIGURE 2.19 SYSTEM BEHAVIOR FOR ELEVATION ANGLES LESS THAN 90°. THE BLACK LINE REPRESENTS THE GRAVITATIONAL TORQUE IN THE UNLOADED CONDITION WHILE THE COLORED LINES REPRESENT THE MKM TORQUE AT DIFFERENT SUPPLY PRESSURES. 44
FIGURE 3.1 UPWARD (BLUE LINE) AND MEDIALLY (BLACK LINE) SJC TRANSLATION IN THE EXOSKELETON WORKING RANGE CALCULATED CONSIDERING A MAN OF 1.7 M. 46

FIGURE 3.2 ILLUSTRATION OF A JOINT MISALIGNMENTS BETWEEN EXOSKELETON AND THE HUMAN LIMB (A). THE ANALYTICAL MODEL TO ASSESS THE MAGNITUDE OF CONSTRAINTS DISPLACEMENTS D (B) AND THE EXOSKELETON SUPPORT TORQUE (C)..... 47
FIGURE 3.3 THE ESTIMATED SHEAR FORCE AT THE BRACELET-UPPER ARM INTERFACE..... 48
FIGURE 3.4 PERCENTAGE OF THE GRAVITATIONAL TORQUE PROVIDED BY THE EXOSKELETON IN THE UNLOADED CONDITION (A) AND WITH 1 KG (B) AND 2 KG (C) IN THE HAND, TAKING INTO ACCOUNT SJC-EXOJC MISALIGNMENT. BLACK DOTS REPRESENT THE STATIC EQUILIBRIUM OF THE SYSTEM (I.E., THE EXOSKELETON PROVIDES 100% OF THE TORQUE NEEDED TO KEEP THE ARM IN THAT POSITION)..... 49
FIGURE 3.5 MAPS OF THE EXOJC POSITIONS..... 49
FIGURE 3.6 PERCENTAGE OF THE GRAVITATIONAL TORQUE PROVIDED BY THE EXOSKELETON FOR DIFFERENT EXOJC POSITIONS: $EXOJC_1$ (A); $EXOJC_2$ (B); $EXOJC_3$ (C); $EXOJC_4$ (D); $EXOJC_5$ (E); $EXOJC_6$ (F); $EXOJC_7$ (G); $EXOJC_8$ (H). BLACK DOTS REPRESENT THE STATIC EQUILIBRIUM OF THE SYSTEM (I.E., THE EXOSKELETON PROVIDES 100% OF THE TORQUE NEEDED TO KEEP THE ARM IN THAT POSITION)..... 50
FIGURE 3.7 THE ESTIMATED SHEAR FORCE MAGNITUDE FOR THE DIFFERENT EXOJC POSITION ILLUSTRATED IN FIGURE 3.5..... 51
FIGURE 3.8 FIRST DESIGN OF THE KINEMATIC CHAIN. THE GREEN DOT IS THE ROTATION AXES INTERSECTION WHICH SHOULD BE ALIGNED WITH THE SJC..... 52
FIGURE 3.9 EXAMPLES OF THE KINEMATIC CHAIN MOVEMENT. (A) FLEXION; (B) ABDUCTION..... 52
FIGURE 3.10 FINAL DESIGN OF THE KINEMATIC CHAIN (A) AND DETAILS OF THE ABDUCTION (B) AND FLEXION (C) JOINT. THE GREEN DOT IS THE ROTATION AXES INTERSECTION WHICH SHOULD BE ALIGNED WITH THE SJC..... 53
FIGURE 3.11 EXAMPLES OF THE KINEMATIC CHAIN MOVEMENT. (A) FLEXION. (B) ABDUCTION..... 54
FIGURE 4.1 EXOSKELETON STRUCTURE (A) CONSISTING OF TWO EXOSKELETON ARMS (B), A BACK FRAME (C), AND A COMMERCIAL HARNESS (D)..... 55
FIGURE 4.2 EXOSKELETON STRUCTURE..... 56
FIGURE 4.3 ADJUSTMENT ELEMENTS. (A) ADJUSTMENT OF THE LONGITUDINAL POSITION OF THE BRACELET. (B) ADJUSTMENT OF THE SHOULDER WIDTH. (C) ADJUSTMENT OF THE SHOULDER-PELVIS DISTANCE..... 58
FIGURE 4.4 GRAPHICAL REPRESENTATION OF THE EXOSKELETON. 59
FIGURE 4.5 REPRESENTATION OF THE EXOSKELETON ARM. RA AND MA ARE THE FIXED SUPPORT CONSTRAINING REACTIONS; F_W IS THE USER'S ARM GRAVITATIONAL LOAD; F_M IS THE USER'S MUSCULAR FORCE; F_{MKM} IS THE CABLE TRACTION FORCE. A IS THE ANGLE BETWEEN THE CABLE AND THE Y-AXIS; B IS THE ANGLE BETWEEN THE PROJECTION OF THE CABLE ON THE TRANSVERSE PLANE AND THE X-AXIS; L_{SP} IS THE CAM-LENGTH; Θ_F AND Θ_A ARE THE SHOULDER FLEXION AND ABDUCTION ANGLE, RESPECTIVELY..... 60
FIGURE 4.6 REPRESENTATION OF THE BACK FRAME. RA AND MA ARE THE FIXED SUPPORT CONSTRAINING REACTIONS; F_{MKM} IS THE MKM TRACTION FORCE; R_{1X} AND R_{1Y} ARE THE X AND Y COMPONENTS OF THE REACTION FORCE EXCHANGED BETWEEN THE BACK-FRAME AND THE PELVIC BELT; R_{2X} AND R_{2Z} ARE THE X AND Z COMPONENTS OF THE REACTION FORCE EXCHANGED BETWEEN THE BACK-FRAME AND THE THORACIC BELT; A IS THE ANGLE BETWEEN F_{MKM} AND THE Y-AXIS; B IS THE ANGLE BETWEEN THE PROJECTION OF F_{MKM} ON THE TRANSVERSE PLANE AND THE X-AXIS. THE SUBSCRIPTS R AND L REFER TO THE RIGHT AND LEFT SIDES..... 63
FIGURE 4.7 A SKETCH OF THE USER HIGHLIGHTING THE CONTACT SURFACES BETWEEN THE EXOSKELETON AND THE UPPER ARM (A), THE THORAX (B), AND THE PELVIS (C) OF THE USER..... 65
FIGURE 4 8 THE PRESSURE EXERTED ON THE LEFT (A) AND RIGHT (B) UPPER ARM OF THE USER TO VARY BOTH FLEXION (Θ_F) AND ABDUCTION (Θ_A) OF THE SHOULDER. THE BLACK LINE REPRESENTS THE PAIN DETECTION THRESHOLD (PDT)..... 65

FIGURE 4.9 THE PRESSURE EXERTED ON THE CHEST (A) AND PELVIS (B) OF THE USER TO VARY BOTH FLEXION (Θ_F) AND ABDUCTION (Θ_A) OF THE SHOULDER. THE BLACK LINE REPRESENTS THE PAIN DETECTION THRESHOLD (PDT).. 66
FIGURE 4.10 CAD MODEL OF THE EXO-ARM WITH CONSTRAINTS AND LOADS HIGHLIGHTED BY GREEN AND RED ARROWS, RESPECTIVELY. 67
FIGURE 4.11 VON MISES STRESSES EXPRESSED IN MPA IN THE WHOLE RIGHT EXO-ARM. 69
FIGURE 4.12 VON MISES STRESS EXPRESSED IN MPA IN THE STAINLESS STEEL COMPONENT. 70
FIGURE 4.13 VON MISES STRESS EXPRESSED IN MPA IN THE ALUMINUM ALLOY COMPONENT..... 70
FIGURE 4.14 SHOULDER PAD MAXIMUM NORMAL STRESS IN THE FIBER (A) AND TRANSVERSAL DIRECTION (B - C). STRESSES ARE IN MPA..... 71
FIGURE 4.15 BRACELET MAXIMUM NORMAL STRESS IN THE FIBER (A) AND TRANSVERSAL DIRECTION (B-C). STRESSES ARE IN MPA. 71
FIGURE 4.16 DISPLACEMENT IN X (A) AND Y (B) DIRECTION. DATA ARE EXPRESSED IN MM..... 72
FIGURE 4.17 CAD MODEL OF THE BACK FRAME. THE GREEN ARROWS REPRESENT THE MODEL CONSTRAINTS, WHILE RED AND BLUE ARROWS REPRESENT FORCES AND TORQUES ACTING ON THE STRUCTURE..... 73
FIGURE 4.18 VON MISES STRESS EXPRESSED IN MPA IN THE STAINLESS STEEL COMPONENT OF THE BACK FRAME.... 75
FIGURE 4.19 VON MISES STRESS EXPRESSED IN MPA IN THE ALUMINUM ALLOY COMPONENT OF THE BACK FRAME. 75
FIGURE 4.20 DISPLACEMENT MAGNITUDE OF THE BACK FRAME. DATA ARE EXPRESSED IN MM. 76
FIGURE 4.21 DISPLACEMENT IN X (A), Z (B), AND Y (C) DIRECTION. DATA ARE EXPRESSED IN MM. 76
FIGURE 4.22 REAR (A), LEFT SIDE (B) AND UPPER (C) VIEW OF THE PROTOTYPE. 77
FIGURE 5.1 TEST-BENCH DEVELOPED FOR THE TORQUE GENERATOR CHARACTERIZATION..... 79
FIGURE 5.2 MUSCLE SHORTENING MEASURED DURING STATIC CHARACTERIZATION TESTS..... 81
FIGURE 5.3 MEASURED (BLACK LINES) AND ESTIMATED (RED LINES) MKM TRACTION FORCES AT DIFFERENT SUPPLY PRESSURES. (A) P = 3 BAR; (B) P = 4 BAR; (C) P = 5 BAR. 82
FIGURE 6.1 EMG ELECTRODES LOCATION IN ANTERIOR DELTOID. BLACK CROSS INDICATES ACROMION POSITION. .. 84
FIGURE 6.2 EMG ELECTRODES LOCATION IN MIDDLE DELTOID. BLACK CROSS INDICATES ACROMION POSITION. BLUE CROSS INDICATES LATERAL EPICONDYLE OF THE ELBOW POSITION. 84
FIGURE 6.3 EMG ELECTRODES LOCATION IN LATISSIMUS DORSI. GREY DASHED LINE INDICATES THE LOWER EDGE OF THE SCAPULA. 85
FIGURE 6.4 EMG ELECTRODES LOCATION IN LONGISSIMUS. BLACK CROSS INDICATES L1 POSITION. 85
FIGURE 6.5 EMG ELECTRODES LOCATION IN ILIOCOSTALIS. BLACK CROSS INDICATES THE LOWEST POINT OF THE LAST RIB. LIGHT BLUE CROSS INDICATES THE POSTERIOR ILIAC SPINE. YELLOW CROSS INDICATE L1 POSITION..... 86
FIGURE 6.6 BACK (A), FRONT (B), AND RIGHT-SIDE VIEW (C) OF THE MARKER SET PLACED ON THE SUBJECT..... 87
FIGURE 6.7 MARKER SET PLACED ON THE EXOSKELETON. 88
FIGURE 6.8 COORDINATES IN THE GLOBAL REFERENCE SYSTEM OF THE LABORATORY OF THE MARKERS C7 (A), RSHO (B), AND RELB (C). THE CONTINUOUS LINES REPRESENT THE ACQUIRED TRAJECTORIES, WHILE THE THICK DASHED LINES REPRESENT THE RECONSTRUCTED TRAJECTORIES. THE X, Y, AND Z COORDINATES ARE SHOWN IN RED, BLUE AND GREEN, RESPECTIVELY. 91
FIGURE 6.9 DESCRIPTIVE SCHEME OF THE CHORD FUNCTION. I, J, AND K (RED DOTS) ARE THE COORDINATES OF THE POINTS THE FUNCTION REQUIRES. S, R, AND T (BLUE ARROWS) DEFINE THE RIGHT-HAND REFERENCE SYSTEM BASED ON THE COORDINATES OF POINTS I, J, AND K. FINALLY, JC IS THE POSITION OF THE REQUIRED JOINT CENTER (GREEN DOT). 92
FIGURE 6.10 DESCRIPTIVE SCHEME OF THE ALGORITHM USED FOR THE CALCULATION OF SJC (A), EJC (B) AND WJC (C)..... 94

FIGURE 6.11 STATIC TASK. THE SHOULDER FLEXION ANGLE IS EQUAL TO 90° (A) OR 110° (B)..... 98
FIGURE 6.12 A REPRESENTATIVE RECORDING OF THE EMG SIGNAL (A), SHOULDER AND ELBOW ANGLES (B), COP DISPLACEMENT (C), AND SJC (RED DOTS) AND EXOJC (BLUE DOT) POSITION IN THE UPPER-ARM ELEVATION PLANE (D) OBSERVED DURING STATIC TASKS. IN (A) AND (B), THE GREEN DOTS DEFINE THE RANGE WITHIN THE MEAN VALUES OF THE RECTIFIED EMG AND JOINT ANGLES ARE CALCULATED. 99
FIGURE 6.13 A REPRESENTATIVE RECORDING OF THE EMG SIGNAL (A), SHOULDER AND ELBOW ANGLES (B), COP DISPLACEMENT (C), AND SJC (COLORED DOTS) AND EXOJC (BLUE DOT) POSITION IN THE UPPER-ARM ELEVATION PLANE (D) OBSERVED DURING DYNAMIC TASKS. IN (A) AND (B), THE GREEN DOTS DEFINE THE CYCLES START INSTANTS WHILE THE YELLOW DOTS ARE THE END CYCLES INSTANTS. 100
FIGURE 6.14 SHOULDER MUSCLES ARV PERCENTAGE VARIATION BETWEEN THE FREE AND EXO STATIC TRIAL OF SUBJECT 1 (BLUE BARS) AND SUBJECT 2 (RED BARS). (A) 90° OF SHOULDER FLEXION; (B) 110° OF SHOULDER FLEXION. GRAPHS ON THE LEFT REFERS TO LEFT USERS ARM WHILE GRAPHS ON THE RIGHT REFERS TO RIGHT ARM. 102
FIGURE 6.15 SHOULDER MUSCLES ARV PERCENTAGE VARIATION BETWEEN THE FREE AND EXO DYNAMIC TRIAL OF SUBJECT 1 (BLUE BARS) AND SUBJECT 2 (RED BARS). (A) WITHOUT HAND-TOOL; (B) WITH HAND-TOOL..... 103
FIGURE 6.16 LUMBAR MUSCLES ARV PERCENTAGE VARIATION BETWEEN THE FREE AND EXO STATIC TRIAL OF SUBJECT 1 (BLUE BARS) AND SUBJECT 2 (RED BARS). (A) 90° OF SHOULDER FLEXION; (B) 110° OF SHOULDER FLEXION. GRAPHS ON THE LEFT REFERS TO MUSCLE ON THE LEFT SIDE OF THE BODY WHILE GRAPHS ON THE RIGHT REFERS TO MUSCLES ON THE RIGHT SIDE OF THE BODY. 104
FIGURE 6.17 RIGHT SIDE LUMBAR MUSCLES ARV PERCENTAGE VARIATION BETWEEN THE FREE AND EXO DYNAMIC TRIAL OF SUBJECT 1 (BLUE BARS) AND SUBJECT 2 (RED BARS). (A) WITHOUT HAND-TOOL; (B) WITH HAND-TOOL..... 104
FIGURE 6.18 COP_{RMS} PERCENTAGE VARIATION BETWEEN THE FREE AND EXO TRIAL OF SUBJECT 1 (BLUE BARS) AND SUBJECT 2 (RED BARS). (A) 90° OF SHOULDER FLEXION; (B) 110° OF SHOULDER FLEXION; (C) DYNAMIC TASK; (D) DYNAMIC TEST WITH HAND-TOOL. 105

Chapter 1

Introduction

In recent years, work-related musculoskeletal disorders (MSDs) represent a health, demographic, and social challenge. MSDs reduce the workers' quality of life and can result in different injuries or pathologies, such as dislocations, sprains, strains, bone fractures, sarcopenia, inflammations, degenerative tendinitis, osteoarthritis, and osteoporosis [1]. In addition to health consequences, MSDs lead to high costs to enterprises and society due to absenteeism, production and productivity losses, and increased healthcare costs. Nowadays, the MSDs impact cannot be neglected since three in five workers suffer from MSDs in Europe [1]. In addition, the incidence of MSDs is age-related and may increase in the following years due to the aging population and increased retirement age. Finally, about 40% of MSDs cases concern the upper limbs and shoulder. The main risk factor is the high compressive load on the shoulder joint during activities that require lifting the arms above the shoulders [1, 2].

Several strategies have been proposed to mitigate this scenario. For example, cooperative robotic systems spread in Industry 4.0 [3, 4] to replace humans in repetitive tasks. However, manufacturing automation is limited by frequent variations in the production systems and the increasing need for product customization. Moreover, some working activities require decision-making skills and flexibility. In all these cases, wearable robots could represent a valid alternative [5, 6]. The concept of using technological equipment to aid human movement is not new. In the last century, portable aid devices were utilized in medical care [7] and designed for military applications [8]. On the other hand, using exoskeletons to safeguard workers' physical health is a relatively recent concept.

Regardless of the intended use, exoskeletons can be classified according to the assisted body part into lower-limb, upper-limb, and full-body exoskeletons. The primary purpose of a lower-limb exoskeleton generally consists of assisting

locomotion, providing stability, and supporting user weight. On the other hand, the upper-limb exoskeleton must ensure a wide range of motion of the upper limb to reduce the load on the shoulder [9] and the shoulder muscle activity [10–15] during manipulation tasks. Finally, full-body exoskeletons are generally developed to assist users in standing, walking, handling tasks, or lifting heavy loads. They can transfer the internal forces due to the exoskeleton mass or the assistive torque generated directly to the ground without over-soliciting other body parts. On the other hand, their structures are usually very complex, heavy, and bulky. Full-body and lower-limb exoskeletons will not be discussed further because they are not among the aims of this dissertation.

Exoskeletons can also be differentiated into active or passive. In the first case, they actively assist human movements thanks to one or more actuators [16–20]. In other words, an external power source supplies the energy needed to perform the movement. In the second case, passive elastic systems [13, 21–25] counterbalance the gravitational torque acting on the assisted human joint. Thus, the user performs the movement while the exoskeleton assists him in doing it.

The following sections of Chapter 1 present the basic principles of shoulder biomechanics, the upper limb industrial exoskeleton design challenges, and state-of-the-art.

1.1 Shoulder biomechanics

1.1.1 Structure of the shoulder

The upper limb must ensure adequate positioning in the space of the hands for the performance of all functional activities. The high physiological shoulder range of motion comes from the interaction of four different joints (Figure 1.1): the glenohumeral (GH), the sternoclavicular (SC), the acromioclavicular (AC), and the scapulothoracic (ST) joint.

The GH joint is an enarthrosis and articulates the humerus hemispherical head with the glenoid fossa of the scapula. The surface of the humerus head is three times larger and has a smaller radius of curvature than the surface of the glenoid fossa. In this way, the humerus can rotate freely in all directions and slide on the glenoid fossa surface. This high mobility is obtained at the expense of poor stability of the joint that is guaranteed only by the presence of numerous ligaments and tendons of the rotator cuff muscles (supraspinatus, infraspinatus, teres minor, and subscapularis). These muscles and the biceps contract to push the humerus head against the glenoid fossa and reduce the risk of joint dislocation before any humerus movement.

The SC joint is the saddle joint between the proximal end of the clavicle and the sternum. It allows the clavicle rotation on the frontal and transverse planes.

The AC joint is the diarthrodial joint between the acromion process of the scapula and the distal end of the clavicle. It allows gliding movements of the clavicula.

The ST joint articulates the scapula and the chest wall and permits the scapula translation on the sagittal and frontal planes.

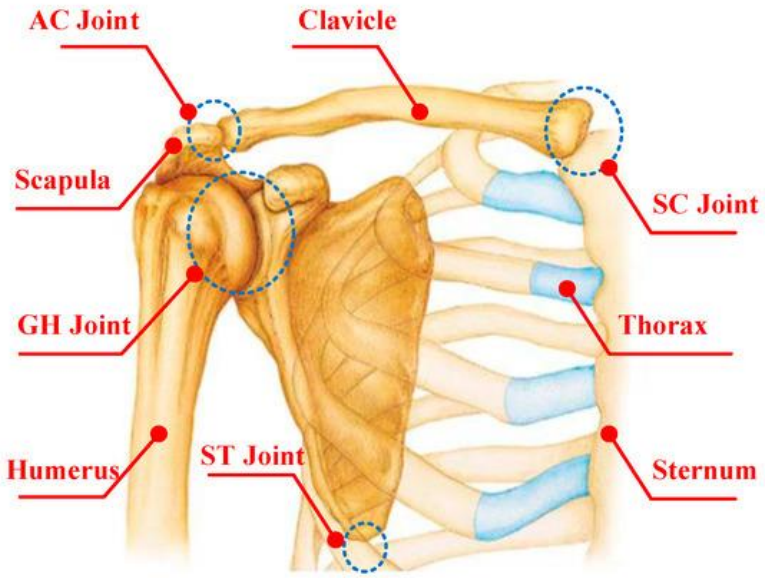

Figure 1.1 Shoulder joint anatomy [26].

1.1.2 Shoulder kinematics

The interaction between the four shoulder joints grants the arms the highest range of movement in the human body. The motility of the arm results in the degrees of freedom (DoFs) shown in Figure 1.2.

The upper-arm flexion/extension (Figure 1.2 a) occurs in the sagittal plane and moves the arm forward/backward. The upper arm flexion range is about 180°, and it is mainly generated by the anterior deltoid and the pectoralis major contraction. The maximum extension instead is about 60° and is due to the action of the sternocostal pectoralis, latissimus dorsi, and teres major.

The upper-arm abduction moves the limb away from the body, while adduction brings the arm closer to the body. The abduction/adduction can take place both on the frontal (Figure 1.2 b) and on the transverse (Figure 1.2 c) plane. In the first case, the abduction is caused by the contraction of the middle deltoid and supraspinatus. On the contrary, the adduction is generated by the latissimus dorsi, teres major, and sternocostal pectoralis action. In the second case, the movement is called horizontal abduction/adduction, and the muscles involved are the middle and posterior deltoid, infraspinatus, and teres minor for the horizontal abduction; and the pectoralis major, the anterior deltoid, and the coracobrachialis for the horizontal adduction. The

shoulder can attain up to 180° of abduction, 50° of adduction, and 90° of horizontal abduction and adduction.

The upper-arm medial and lateral rotation is the humerus rotation around its longitudinal axis. Medial rotation derives mainly from the action of the subscapularis and teres major. On the contrary, infraspinatus and teres minor produce lateral rotation. Both medial and lateral rotation can achieve 90°.

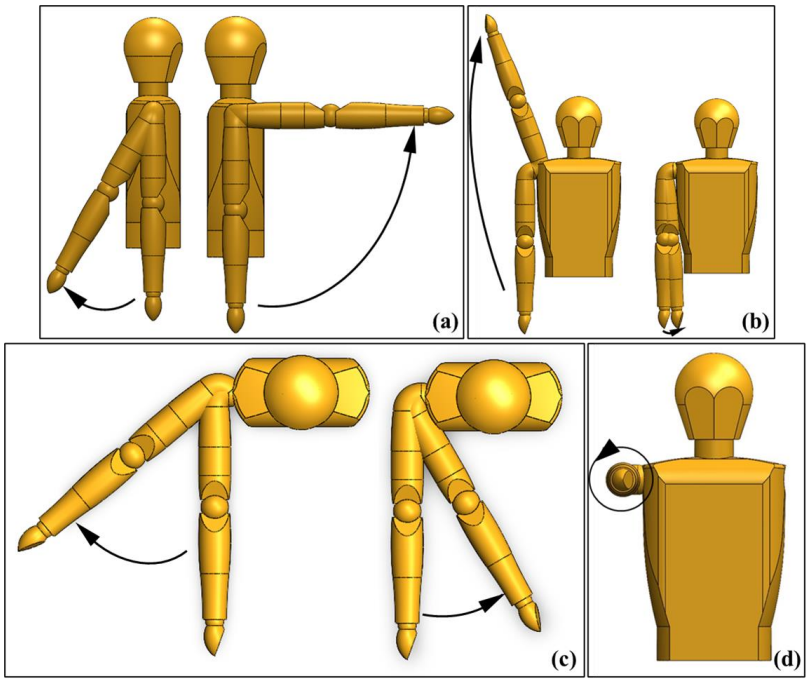

Figure 1.2 Upper-arm movement. (a) Extension-Flexion; (b) Abduction-Adduction; (c) Horizontal Abduction-Adduction; (d) Medial-Lateral Rotation

In addition to the activity of the muscles listed above, the movement of the arm is possible thanks to the action of numerous other muscles that help to stabilize the joint during movement (Figure 1.3). The upper limb range of movement and the shoulder muscles' action are summarized in Table 1.1 and 1.2, respectively.

Table 1.1 Physiological movements of the upper arm.

Movement of the shoulder	Mobility range
Flexion	0° - 180°
Extension	0° - 60°
Abduction (frontal plane)	0° - 180°
Adduction (frontal plane)	0° - 50°
Abduction (transverse plane)	0° - 90°
Adduction (transverse plane)	0° - 90°
Internal Rotation	0° - 90°
External Rotation	0° - 90°

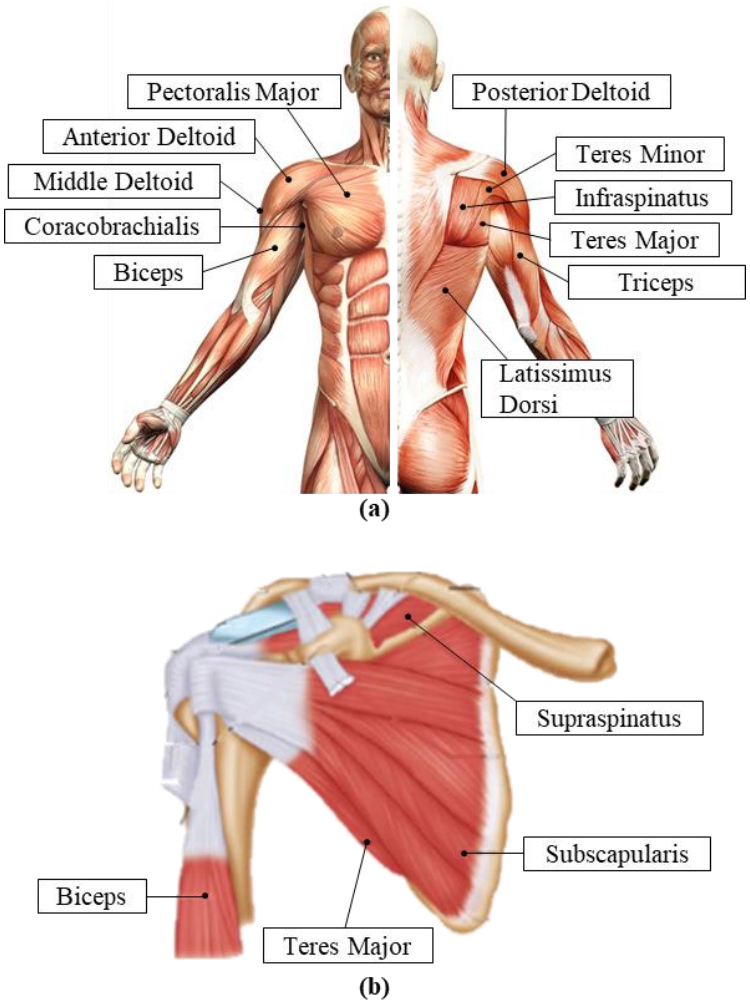

Figure 1.3 Superficial (a) and deep (b) shoulder muscles illustration.

Table 1.2 Shoulder muscles action

Function	Muscles
Flexors	Anterior Deltoid, Pectoralis Major, Coracobrachialis, Biceps.
Extensor	Posterior Deltoid, Pectoralis Major, Latissimus Dorsi, Teres Major, Triceps.
Abductors	Middle Deltoid, Supraspinatus, Biceps.
Adductors	Pectoralis Major, Coracobrachialis, Latissimus Dorsi, Teres Major, Biceps, Triceps.
Horizontal Abductors	Middle Deltoid, Posterior Deltoid, Latissimus Dorsi, Infraspinatus, Teres Minor.
Horizontal Adductors	Anterior Deltoid, Pectoralis Major, Coracobrachialis, Biceps.
Medial Rotators	Anterior Deltoid, Pectoralis Major, Latissimus Dorsi, Teres Major, Subscapularis, Biceps.
Lateral Rotators	Posterior Deltoid, Infraspinatus Teres Major.

Regardless of the arm elevation plane considered, humerus elevation involved the rotation of the scapula and clavicula [27].

This synchronism is called scapulohumeral rhythm and has as a direct consequence the shoulder joint center (SJC) movement in both vertical and horizontal directions during arm elevation. Although the humerus and scapula positions depend on the anatomical characteristics of the subject, several models have been developed to quantitatively describe the relationship between the SJC displacement and the arm elevation angle [28–31].

Nef and Riener [32] developed a mathematical model in which the GH joint, the SC joint, and the AC joint were modeled as ball and socket joints. The authors derived the relation reported in Equation (1.1) by assuming that subjects with the same body size have the same SJC movement pattern, and the SJC movement is independent of the elevation plane, the internal/external shoulder rotation, and additional masses.

$$\begin{cases} x_{SJC} = (-14.94 * \sin(\alpha) + 6.68 * \sin(\alpha + \beta)) * \dfrac{h}{h_{ref}} \\ y_{SJC} = (-14.94 * \cos(\alpha) + 6.68 * \cos(\alpha + \beta)) * \dfrac{h}{h_{ref}} \end{cases} \tag{1.1}$$

$$\begin{cases} \alpha = 0.13 * \theta_1 + 99° & 0° \leq \theta_1 \leq 30° \\ \alpha = 0.22 * \theta_1 + 96.4° & 30° \leq \theta_1 \leq 80° \\ \alpha = 114° & 80° \leq \theta_1 \leq 140° \\ \alpha = 0.225 * \theta_1 + 82.5° & 140° \leq \theta_1 \leq 180° \end{cases} \tag{1.2}$$

$$\begin{cases} \beta = 143° & 0° \leq \theta_1 \leq 30° \\ \beta = 143° & 30° \leq \theta_1 \leq 80° \\ \beta = 0.58 * \theta_1 + 96.4° & 80° \leq \theta_1 \leq 140° \\ \beta = 178° & 140° \leq \theta_1 \leq 180° \end{cases} \tag{1.3}$$

In Equations (1.1) (1.2) (1.3), x_{SJC} and y_{SJC} are the SJC coordinates expressed in a plane parallel to the frontal plane and with origin in SC-joint; α and β are the SC and AC joint angle, respectively; h is the height of the considered subject while h_{ref} is equal to 180 cm; θ_1 is the arm elevation angle.

As shown in Figure 1.4, the SJC vertical translation is not negligible. Exploring the entire shoulder flexion range (0° – 180°), the SJC vertical displacement for a 170 cm high subject is about 11 cm. On the other hand, its horizontal displacement is just 2 cm and occurs mainly above 130° of flexion.

In conclusion, the shoulder can be modelized as a mechanism with a total of 5 degrees of freedom: the three humerus rotations, namely the upper-arm flexion-extension, abduction-adduction, and internal-external rotation (see Figure 1.2), and the two translational movements of the SJC (see Figure 1.4).

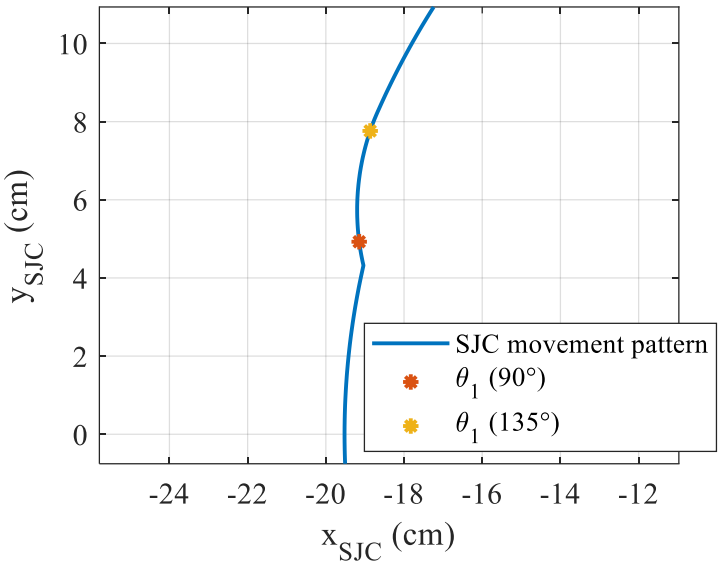

Figure 1.4 SJC position with respect to SC joint in the frontal plane during arm elevation. Data are estimated for a man of 1.7 m.

1.1.2 Shoulder kinetics

The GH joint directly mechanically supports the upper arm and sustains most of the load acting on the entire shoulder joint. Although the arm weight represents only about 5% of body weight, the high lever arms of gravitational forces produce high gravitational torque in the shoulder. When the shoulder muscles contract to support the extended arm, the compressive load on the GH joint can be worth 50% of the total body weight [33]. This value is halved when the elbow is flexed. Therefore, the shoulder gravitational torque (M_g) depends on the subject anthropometry and the upper-arm and forearm flexion angle and can be calculated by solving Equations (1.4 – 1.8):

$$l_f = \sqrt{L_1^2 + b_2^2 - 2 * L_1 * b_2 * \cos(\pi - \theta_2)} \tag{1.4}$$

$$\alpha_f = \operatorname{acos}\left(\frac{L_1^2 + l_f^2 - b_2^2}{2 * L_1 * l_f}\right) \tag{1.5}$$

$$l_h = \sqrt{L_1^2 + (L_2 + b_3)^2 - 2 * L_1 * (L_2 + b_3) * \cos(\pi - \theta_2)} \tag{1.6}$$

$$\alpha_h = \operatorname{acos}\left(\frac{L_1^2 + l_h^2 - (L_2 + b_3)^2}{2 * L_1 * l_h}\right) \tag{1.7}$$

$$M_g = m_1 * g * b_1 * \sin(\theta_1) + m_2 * g * l_f * \sin(\theta_1 + \alpha_f) + m_3 * g * l_h * \sin(\theta_1 + \alpha_h) \quad (1.8)$$

In Equations (1.4 – 1.8), l_f is the distance between SJC and the forearm center of mass (CoM_2); l_h is the distance between SJC and the hand center of mass (CoM_3); L_1 and L_2 are the upper arm and the forearm lengths, respectively; b_2 is the distance between CoM_2 and the elbow joint center (EJC); b_3 is the distance between CoM_3 and the wrist joint center (WJC); θ_1 and θ_2 are the shoulder and the elbow flexion angles, respectively; α_f is the angle between l_f and L_1 (see Figure 1.5); α_h is the angle between l_h and L_1 (see Figure 1.5); m_1, m_2 and m_3 are the upper arm, forearm, and hand masses; g is the standard gravity acceleration.

The shoulder gravitational torque M_g reaches its maximum value when the shoulder elevation angle θ_1 and the elbow flexion angle θ_2 are 90° and 0°, respectively. For the sake of clarity, the M_g pattern calculated for a subject of 1.7 m height and body mass equal to 70 kg is shown in Figure 1.5. The anthropometric distance and the inertial parameters required by Equations (1.4 – 1.8) are calculated based on the parameters identified by Winter [34] and listed in Table 1.3

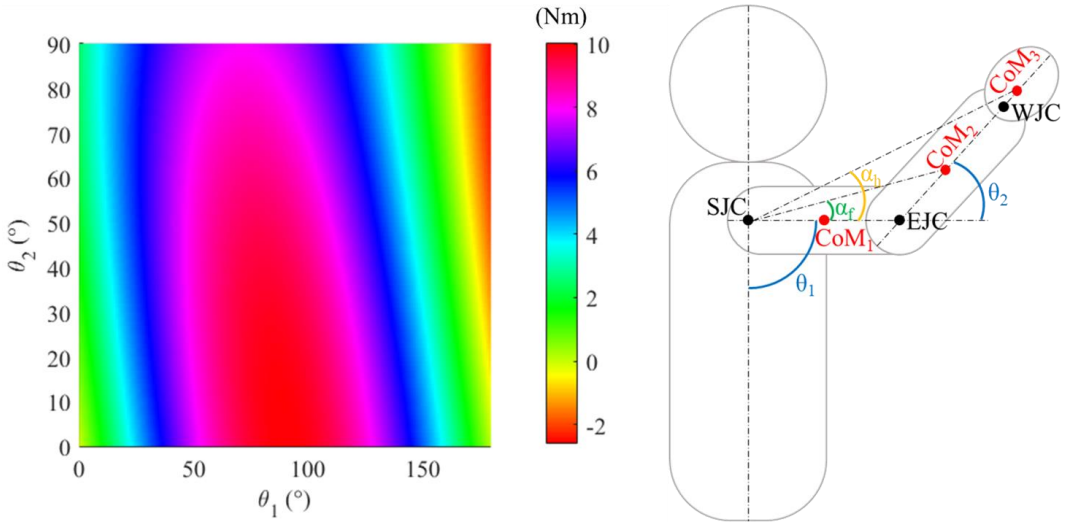

Figure 1.5 Gravitational torque on shoulder joint center with respect to the elevation angle of the upper arm θ_1 and the forearm flexion angle θ_2. SJC, EJC, and WJC represent the glenohumeral joint center, the elbow joint center, and the wrist joint center respectively, whereas CoM_1, CoM_2, and CoM_3 are the centers of mass of the upper arm, forearm, and hand.

Table 1.3 Anthropometric data used to estimate the joint torque values shown in Figure 1.5. EJC and WJC represent the elbow and wrist joint centers, respectively, whereas CoM_2 and CoM_3 are the center of mass of the forearm and hand, respectively.

Symbol	Definition	Value
m_1	Upper arm weight	1.96 kg
m_2	Forearm weight	1.12 kg
m_3	Hand weight	0.42 kg
L_1	Upper arm length	0.32 m
L_2	Forearm length	0.25 m
b_2	EJC – CoM_2 distance	0.11 m
b_3	WJC – COM_3 distance	0.66 m

1.2 Exoskeleton for overhead work

1.2.1 Design Features

Upper limb exoskeletons aim to replicate human kinematics and kinetics to support arm movement and empower the user. Achieving this aim requires the application of external forces to the musculoskeletal system. The close physical human-robot interaction and the fact that the human being is an integral part of the system impose several requirements and constraints in the design of exoskeletons. The most challenging features that should be considered in the design of this kind of device are:

- *Safety.* The exoskeleton must not induce movements outside the physiological range of motion of the human joints. Moreover, the forces that the exoskeleton applies to the user must be well-defined in magnitude and point of application since high mechanical loads can damage the soft tissues. The injury risk depends not only on the load magnitude but also on the duration of the load application [35, 36]. However, it is supposed that below the pain detection threshold (i.e., the pressure level beyond which the subject begins to feel pain, PDT), there is no risk of soft tissue damage regardless of the application duration [37]. In recent years, many researchers have attempted to determine a generalized PDT value. For this purpose, a single-point pressure algometry (SPA), which applies pressure on the human body through a surface of 1 cm, can be used [38, 39]. Alternatively, to account for the larger exoskeleton interaction surfaces, computerized cuff pressure algometry (CPA) can be used to exert pressure on the human limb through a pneumatically controlled sleeve [40, 41]. However, a standard

is hard to define due to the high inter-subject PDT variability. In addition, PDT also depends on the solicited body point and the characteristics of the interface. For example, soft materials increase PDT by about 13% compared to rigid interface [37]. Therefore, in many cases, padding helps to prevent soft tissue injuries [42]. However, based on the recent results presented in the literature, when designing an exoskeleton, it must be ensured that the maximum pressures applied on the user's body are less than 6 kPa for the trunk [37], 15 kPa for the pelvis [37], and 30 kPa for the upper arm [43].

Regardless of the magnitude of the applied load, it is necessary to avoid bony prominences, tendons, and areas with surface vessels or nerves as load application points.

- *Ergonomics and comfort.* The exoskeleton joints should be aligned with the anatomical joints of the user's upper limbs to avoid undesired forces that may cause pain, dislocation, fracture [44–47], or the reduction of the range of movement. However, it is not easy to achieve perfect human-exoskeleton kinematic compatibility due to the intersubject variability and the difficulty in identifying the exact position of the joint axes. The misalignment between the exoskeleton and human joint axes can be macro or micro [39]. The former occurs when the exoskeleton's kinematic chain is oversimplified compared to the limb one. The second derives from the impossibility of exactly knowing the SJC position and from the exoskeleton attachment point slippage during movement. Given the complex kinematics of the shoulder, misalignment is hard to avoid. However, exoskeletons with high degrees of redundancy have been developed to improve the fit between the human limb and the robotic device [48]. The improvement of the range of motion and ergonomics are achieved at the cost of a complex and heavier mechanism.

  Finally, it is also necessary not over-soliciting the other body parts to reduce the load on the shoulder. Previous studies have shown that upper-limb exoskeletons increase lumbar muscle activity and lower limb stresses [49–52]. In addition, the presence of the exoskeleton can affect balance performance and increase cardiovascular demands [14, 50, 51]. However, by limiting the weight and bulk of the exoskeleton and appropriately designing the human-exoskeleton interface, it is possible to reduce the action of the shoulder muscles without altering the functioning of other physiological structures [53].
- *Usability*. Exoskeletons should be easy and quick to wear, light and compact. They should also adapt to different user physical characteristics, and they do not negatively affect human mobility

because fast and complex movements may be necessary in industrial environments to ensure the productivity and safety of the workers. Finally, users should be trained to wear and use the exoskeleton properly to avoid affecting the device's effectiveness.
All these features are essential to improve the exoskeletons usability and acceptability and then ensure exoskeletons use over long periods and in different workplaces. Many studies [22, 23, 54–56] investigated the user experience through qualitative questionnaires and interviews to estimate the device's usability. The results show that the participants in the studies generally positively rated the exoskeleton's usability and comfort after the experimental session. However, long-term surveys are necessary to confirm the results.

1.2.2 Active exoskeletons

Active exoskeletons are currently more widespread than passive ones [57, 58] and can be classified based on the actuation system source into electrical [17, 18, 59], pneumatic [19], or hydraulic [60, 61] exoskeletons. Electric actuators are preferred among all power technologies due to their high dynamic, precision, and ease of control. As can be seen from the prototypes shown in Figure 1.6, an electric actuator is generally placed close to each rotational DoF, increasing the bulk and inertia of the system. On the other hand, pneumatic and hydraulic actuators are strongly discouraged due to their encumbrance power source.

Figure 1.6 Electric active exoskeletons prototypes [17, 59].

Regardless of the power technologies employed, active exoskeletons are generally closed-loop controlled [62–64] and require sensors to acquire signal feedback useful to predict the user’s intention. The assisted segment angular position, rotational speed, and exoskeleton-human interaction forces are frequently used for this aim [65, 66]. In some cases, EMG muscle activity is also detected [67–69].

The complexity of the control system increases as the degrees of freedom increase, so in some cases, passive DoFs are integrated into the exoskeleton structure to give greater mobility to the user without increasing the system encumbrance. An example is the double parallelogram linkage used by Bai et al. [16] to connect two active revolute joints. The double parallelogram, shown in Figure 1.7, makes the exoskeleton range of movement comparable to that of a spherical joint with a remote center of rotation.

However, active exoskeletons have little practical relevance in the industrial environment due to some technical problems related to low power-to-weight ratio, high reaction forces, and battery support [70–72]. In addition, they involve additional biomechanical constraints to meet the requirements in terms of ergonomics and safety.

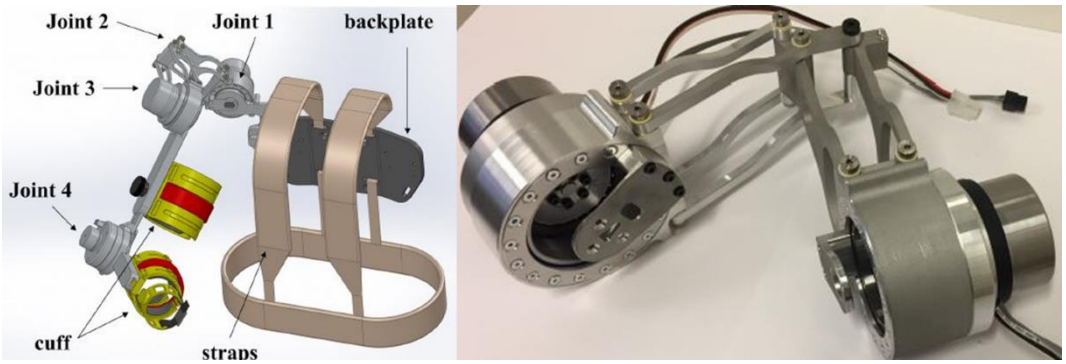

Figure 1.7 The double parallelogram linkage developed by Bai et al [16].

On the other hand, passive exoskeletons are potentially less effective, but they are lighter and less bulky than active ones. In addition, there are no batteries to charge or to change during the work shift.

All these features make passive exoskeletons particularly suitable for use in industrial applications.

1.2.3 Passive exoskeletons

During the past few years, many new passive exoskeletons have been developed to improve ergonomics in repetitive, overhead, and physically demanding tasks.

In this section, the structure of a passive upper limbs exoskeleton for overhead work is analyzed focusing on three commercial devices: PAEXO (Ottobock, Germany, shown in Figure 1.8a); MATE (Comau, Italy, shown in Figure 1.8b); H-Vex (Hyundai, South Korea, Figure 1.8c).

It is possible to identify four main components in their structures: torque generator; physical human-exoskeleton interface (pHEI); kinematic chain; and adjustable systems.

Figure 1.8 Passive upper limb exoskeletons. (a) PAEXO (Ottobock, Germany) [22]; (b) MATE (Comau, Italy) [https://www.comau.com/en]; (c) H-Vex (Hyundai, South Korea) [73].

The *torque generator* is the passive actuation unit and produces the support torque needed to balance the gravitational torque. It generally consists of one or more parallel springs and a transmission to transform the elastic energy into an assistive action. It can be placed behind the back or on the arm of the subject. For instance, PAEXO [22], shown in Figure 1.8a, involves a spring on the back whose lower end is fixed to the hip belt while the upper end is attached to a cable linked to the rear end of the arm bar (Figure 1.8a - point B). The latter is connected anteriorly (Figure 1.8a - point A) to the user's arm. Finally, the arm bar is also hinged with the vertical support bar (Figure 1.8a - point C). The cable applies a downward force on the arm bar, making it rotate around the hinge. The torque magnitude depends on the AC distance. The latter, and consequently the torque profile, can be modified to suit the specific task. The torque generator of MATE [74], shown in Figure 1.8b, is instead located inside the exoskeleton arm and is made up of two connected gears and a set of two parallel springs. The first gear is coupled with the SJC, while the other is not concentrically bonded to the springs set. Due to this misalignment, the elastic force induces the rotation of the second gear around the first one, and hence the arm rises. When the elevation angle is 0°, the elastic force reaches its maximum value while its moment arm is null. As the elevation angle increases, the elastic force decreases, and the moment arm increases. The maximum value of the support torque is reached at 90°, and its magnitude can be adjusted from 3.2 Nm to 5.5 Nm by changing the spring's initial length. H-Vex [73], shown in Figure 1.8c, also has the torque generator inside the exoskeleton arm. The mechanism includes three parallel springs, and five rigid links hinged each other. Some hinges are fixed to the cover frame (Figure 1.8c, grey circles), while others are floating (Figure 1.8c, green circles). The springs are stretched throughout the working range, and their length decreases as the arm elevation angle increases. The tensile force exerted by the springs generates a supporting torque whose profile depends on the position of the joints and the length of the links.

The support torque provided by PAEXO, MATE, and H-Vex reduces muscular activity by about 55%, 43%, and 47%, respectively.

The *pHEI* connects the exoskeleton to the human body and transfers the reaction forces produced by the torque generator to the user's pelvic area. Upper limb exoskeletons are generally linked to the user's arms and pelvis through custom straps. In some cases, a chest belt is also present. In addition, free revolute joints between the rigid structure and the pHEI guarantee the user greater mobility and better comfort.

The *kinematic chain* allows limb movement. As stated before, the exoskeleton should be kinematically compatible with the human body. To this aim, H-Vex [73] implements a four-bar poly-centric structure to track the SJC movement on the transverse plane and prevent misalignment between the shoulder joint axes and the

exoskeleton joint axes of rotation. On the contrary, MATE [74] has the flexion/extension axis aligned with the anatomical joint. The hinge responsible for the abduction/adduction instead is not aligned with any anatomical axis. However, the hinge is combined with a horizontal slider so as not to interfere with the movement of the human arm. Different is the design approach of PAEXO [22]. Only one hinge with a fixed axis of rotation links the arm bar and the support bar. Although the kinematic chain of the exoskeleton does not reflect that of the human joint, the ball joints between the bars and the pHEIs joined to the absence of rigid elements behind the back give the user a high number of degrees of freedom and mobility.

While PAEXO and MATE do not significantly alter the arm's range of motion, H-Vex reduces the maximum flexion angle to 150°.

Adjustable systems are essential to adapt the exoskeleton to different subjects' physical characteristics. Linear guides or telescopic roads are usually implemented to adjust the exoskeleton structure to different heights and widths of the back. The length of the straps that anchor the exoskeleton to the human body is also adjustable.

As inferred from the cases described, a passive exoskeleton often employs a spring-based mechanism to balance gravitational forces. Springs have a lot of advantages. They have linear behavior, store energy without adding inertia, and regain their shape after bending (till certain limits). On the other hand, they have a low energy density, a preload system is required to regulate the exoskeleton's supporting action, and their elastic features could degrade with time.

Thanks to their elastic characteristics, pneumatic artificial muscles (PAM) should be used as passive elements within the exoskeleton structure [75, 76]. They have a lot of advantageous features. Their softness and similarity to the human skeletal muscles allow for safe human interaction. They have also a high power-to-weight ratio and are easy to install, so they do not adversely affect the weight and overall size of the final structure. In addition, the availability of PAM in different sizes and the possibility to change the action level by changing the supply pressure allow for extensive customization of the actuator's response that can match several applications and working conditions. Therefore, by changing the working pressure, the user could tune a priori the magnitude of the support torque over a continuous range of levels. Finally, PAMs are cheap, not sensitive to high temperatures and thermal gradients, dusty and dirty environments so they are suitable to be employed in industrial environments. The main drawbacks of PAMs are the nonlinear behavior and the reduced stroke that could restrict the upper-arm range of movement.

1.3 Pneumatic Artificial Muscle

The general structure of Pneumatic Artificial Muscles (PAMs) consists of a deformable inflatable chamber strengthened with polymeric fibers [77, 78], inextensible fabrics [79], or stiff rings [80, 81]. PAM pressurization results in chamber expansion in the low stiffness direction and axial [82], bending [83], or torsional [84] deformation. The deformation type is determined by the inflatable chamber shape and the reinforcement material arrangement on its surface. The wide variety of sizes and shapes, combined with the multitude of movements and action forces has led to widespread diffusion of these actuators in different fields such as medical research [85], clinical treatment [86], minimally invasive surgery [87–90], rehabilitation and wearable devices [75, 76, 91, 92], extreme environment exploration [80, 81], and grippers [93, 94].

Based on their geometry, PAMs can be classified into McKibben muscle (Figure 1.9a), straight fibers muscle (Figure 1.9b), linear bi-directional actuator (Figure 1.9c), bending pneumatic actuator (Figure 1.9d), air-pocket (Figure 1.9e), and bellows muscle (Figure 1.9f) [95]. Among all these types, the McKibben's muscle (MKM) is the most common.

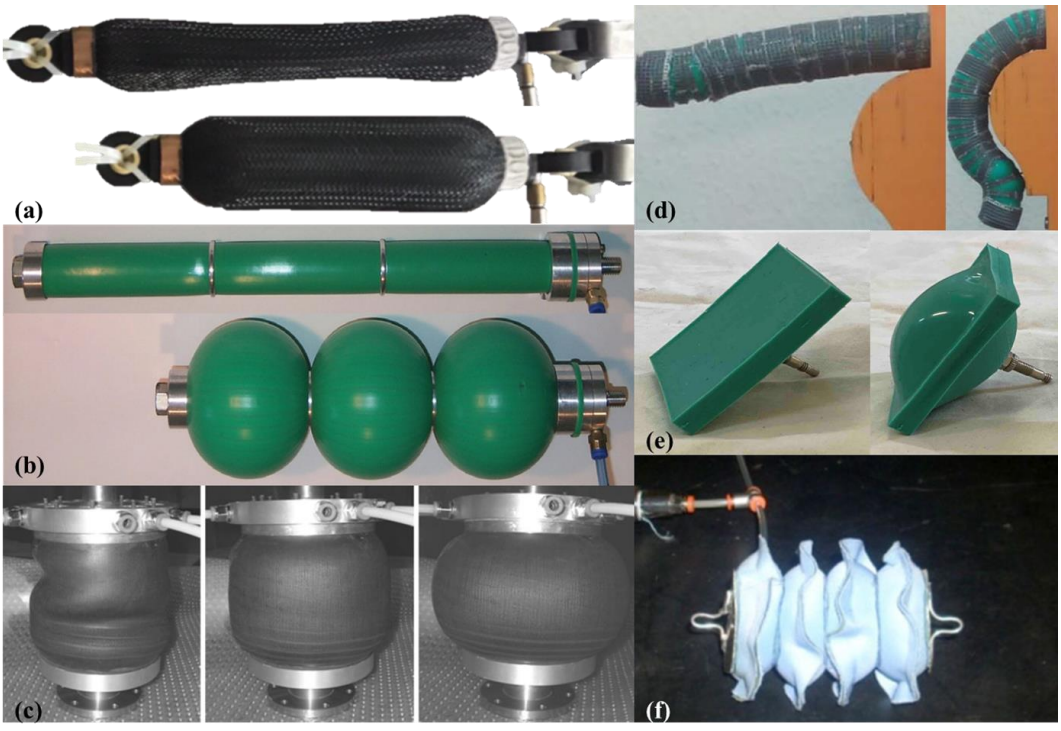

Figure 1.9 (a) McKibben muscle; (b) Straight fibers muscle; (c) Bi-directional actuator; (d) Bending pneumatic actuator; (e) Air-pocket; (f) Bellow muscle. [95]

MKM consists of an elastomeric cylindrical chamber, two heads to fix and pressurize the actuator, and an external net of not lengthening fibers (e.g., nylon) wrapped in a helical configuration around the inflatable chamber and anchored to

the two heads. If pressurized, MKM expands radially. Along the MKM axis, the radial expansion remains constant due to the inextensibility of the fibers. In addition, it is accompanied by an axial contraction. The latter generates a pulling force whose trend is shown in Figure 1.10.

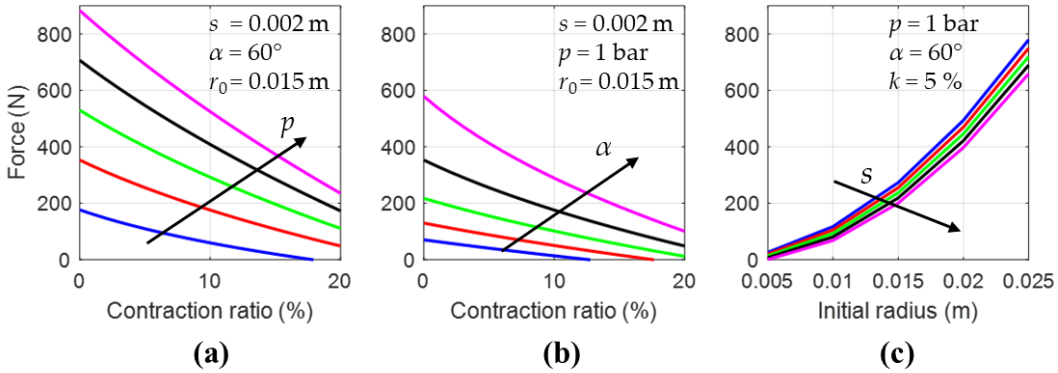

Figure 1.10 McKibben's traction force for different: (a) supply pressure p [0.5; 1; 1.5; 2; 2.5] bar; (b) winding angle α of the inextensible fibers [45; 50; 55; 60; 65]°; (c) thickness s of the inflatable chamber [1; 2; 3; 4; 5] mm. In the graph, r_0 is the resting radius, k is the contraction ratio, and the MKM nominal length is 0.2 m. [95]

The tensile force increases as the initial radius, the winding angle, and the supply pressure increase, and the contraction ratio and chamber thickness decrease. At the same time, the winding angle should not exceed 75° to avoid excessive inflatable chamber strain [78].

The relationship between geometrical and functional parameters and the MKM tensile force is not linear. In addition, hysteretic properties caused by the friction between the elastomeric chamber and the net can be relevant. For these reasons, in the last few years, many studies have presented MKM models to help researchers choose the most suitable actuator for the specific application.

Ferraresi et al. [78] formulated a mathematical model in which the actuator was a homogeneous isotropic tube with constant thickness. Belforte et al. [96] devised a model based on the virtual work principle. Conversely, Antonelli et al. [97] developed a 3D non-linear parametric finite element model. All these models depend on the geometrical properties, the constructive materials, and physical processes occurring within the muscle. On the contrary, Pitei and Tóthová [98] approximated the static characteristic of McKibben PAM produced by FESTO through the exponential function reported in Equation 1.9.

$$F_{MKM} = (a_1 p + a_2)e^{a_3 k} + (a_4 kp) + (a_5 p) + a_6 \qquad (1.9)$$

The a_i coefficients, i =1, …, 6, depend on the specific actuator and can be obtained by interpolating its static characteristic.

In recent years, several studies [99–101] have exploited MKMs to construct active exoskeletons for medical rehabilitation. However, they are relegated to fixed platforms due to the heaviness and bulkiness of the pressurized air power supply. To the author's knowledge, there was only one previous effort to use MKMs as passive elements within an exoskeleton structure. Pardoel and Duomit [102] proposed a passive ankle exoskeleton, shown in Figure 1.11, to assist plantarflexion during walking.

The MKM acts like the gastrocnemius, so it harvests energy between heel-strike and mid-stance and releases it during the push-off and early-swing phases. By reference to Figure 1.11, the MKM upper end is connected to the calf cuff while its lower end is attached to a rod that extends backward the exoskeleton ankle joint, past the heel. The distance between the MKM lower end and the ankle joint defines the traction force lever arm and, hence, the ankle assist torque. Finally, a clutch mechanism ensures that MKM does not hinder the foot plantarflexion during the swing phase. The device produces an assist torque of about 25% of the maximal healthy joint torque when the supply pressure is 70 kPa. The assistance level can theoretically be set by adjusting the supply pressure. However, results highlighted that the ankle range of movement decreases as the supply pressure increases. Thus, a compromise must be found.

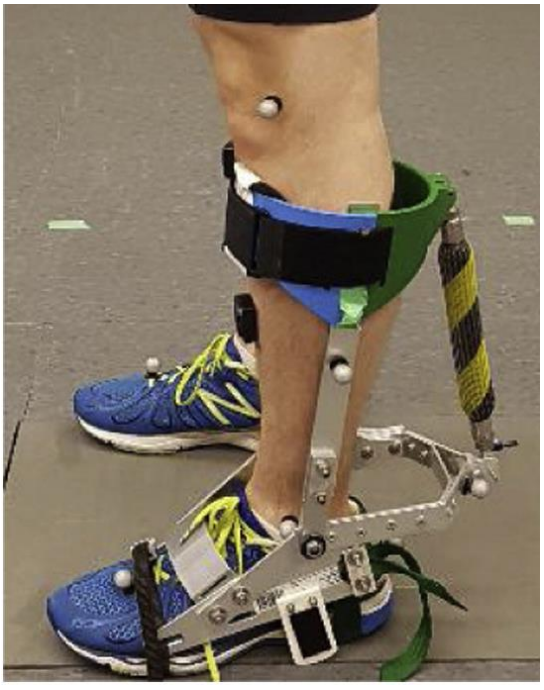

Figure 1.11 Passive walking-assist exoskeleton [102].

In conclusion, attention must be paid to the motion transmission design to avoid an unforeseen range of movement reduction when MKMs are employed as passive elements within an exoskeleton structure.

1.4 Exoskeleton performance metrics

As stated before, industrial exoskeletons aim to reduce the effort in the targeted limb. At the same time, it is crucial to avoid increasing the strain on other body areas, causing awkward postures, decreasing the joint range of motion, and negatively impacting task performance and productivity. Furthermore, exoskeletons should minimize the overall workload, which encompasses both physical and cognitive factors. Users should experience improved physical and mental health while working with an exoskeleton to decide to use it over long periods. Each of the mentioned criteria (i.e., assistive action, balance, joint range of motion, task performance, and user experience) can be objectified by one or more performance metrics.

Measurement of muscle activation is usually employed to quantify both the assistive effects of the exoskeleton on the targeted muscles and the possible extra efforts required in the non-target ones. Muscle activity is typically studied through surface electromyography (sEMG) performed with electrodes placed on the skin. The sEMG signal has a bandwidth between 0 Hz and 500 Hz and can be affected by many factors, such as electrode location, subcutaneous tissue, and skin preparation. The skin is generally shaved and smoothed to improve the quality of sEMG. In addition, to avoid incorrectly positioned or oriented electrodes adversely affecting the quality and amplitude of the signal, the guidelines provided by the European project SENIAM should be followed. Finally, the signal-noise ratio can be increased by filtering sEMG with a band-pass filter with cut-off frequencies of 10 Hz and 500 Hz to reduce aliasing and motion artifacts.

If properly post-processed, the sEMG signal provides information about the magnitude of muscular force and muscle fatigue [34, 39].

The sEMG amplitude in the time domain is proportional to the muscle strength. The first processing step is usually rectification (i.e., the absolute value) of sEMG (Figure 1.12, middle). Unlike the raw signal, the rectified EMG (rEMG) has a non-zero bias whose level depends on the strength of muscle contraction. However, rEMG is typically the input of subsequent processing steps. For example, it can be filtered with a low pass (cutting frequency between 2.3 and 7.8 Hz) or a moving average filter to obtain the linear envelope (eEMG, Figure 1.12 - bottom). By imposing a threshold value on eEMG, it is possible to identify the beginning and end of the contraction (Figure 1.12, red dots). Two issues need to be addressed during this process. The first is the delay introduced by the filter, and the second is the adequate identification of the threshold value, which can be a percentage of the maximum voluntary contraction or the baseline. If the signal is particularly noisy, it may be advantageous to impose two different thresholds, the first to identify the muscle activation, and the second to determine the muscle deactivation. Muscle contraction magnitude can be evaluated through the rEMG time integral (iEMG) or

the rEMG mean value (ARV). While iEMG estimates the muscle contraction energy, ARV is a muscle strength index. Alternatively, the root mean square value of the non-rectified EMG (EMG_{rms}) can be used. The EMG processing steps in the time domain are summarized in Figure 1.12 while the mathematical formulations of iEMG, ARV, and EMG_{rms} are reported in Equations 1.10, 1.11, and 1.12, respectively.

$$\mathrm{iEMG} = \sum_{i=1}^{N} \mathrm{rEMG(i)} \tag{1.10}$$

$$\mathrm{ARV} = \frac{1}{N}\sum_{i=1}^{N} \mathrm{rEMG(i)} \tag{1.11}$$

$$EMG_{rms} = \sqrt{\frac{1}{N}\sum_{i=1}^{N} \mathrm{sEMG(i)}^2} \tag{1.12}$$

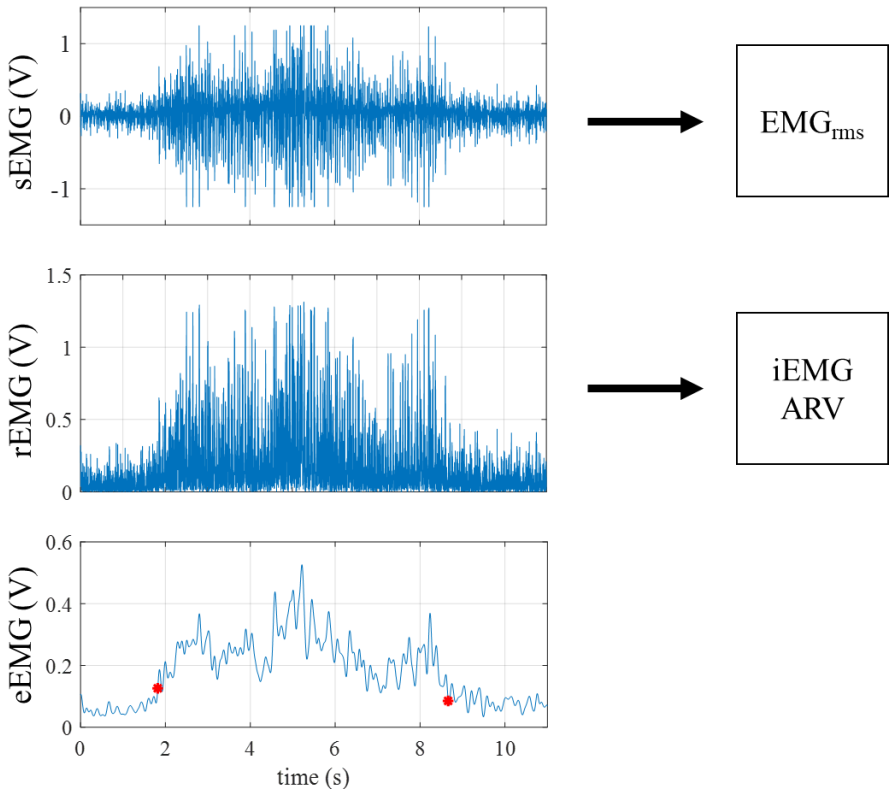

Figure 1.12 EMG processing steps.

On the other hand, the sEMG must be analyzed in the frequency domain to estimate muscle fatigue. The motor unit's firing rate decreases due to fatigue, and

the central nervous system recruits new motor units to compensate for this reduction. The newly recruited motor units are generally made up of slow muscle fibers, so the net result is an increase in sEMG amplitude and a decrease in the sEMG frequency spectrum [103]. Therefore, the trend of the mean or median frequency of the power spectral density function indicates muscle fatigue.

Exoskeleton use may also affect balance due to the additional weight of the device [51]. The center of pressure (CoP) coordinates acquired through a force platform are used to evaluate postural control [104–108]. The most common parameters obtained by the CoP displacement are the maximum amplitude, the RMS amplitude, the mean velocity, and the ellipse area. The first two parameters represent the maximum and RMS displacement of the CoP from its average position, respectively. The ellipse area instead represents the area of the smallest ellipse containing 95% of the CoP trajectory. In all cases mentioned, an increase in the parameter implies worsening balance performance.

Motion range measurements are usually made through stereophotogrammetry, which reconstructs the bone segments' kinematics starting from the markers' three-dimensional trajectories. Generally, at least three markers for each anatomical segment are used. Moreover, the markers are placed on anatomical landmarks to ensure inter-subject repeatability. Although stereophotogrammetry still represents the golden standard in motion capture techniques, there are some issues related to the poor visibility of markers. One or more markers could be occluded by other body segments or the exoskeleton during movement trials hence cameras may not capture them. Another issue is the impossibility of placing the marker on the anatomical landmarks due to the presence of the exoskeleton’s structure. For these reasons, Inertial Measurement Units are sometimes used in the assessment of human kinematics [53]. Motion capture techniques have also been used to evaluate if the user properly wears the exoskeleton and the magnitude of the relative motions between the exoskeleton and the user during the test [74].

Task performance metrics depend on the specific task and can be onset fatigue time [23, 109], number of errors [51], number of repetitions during a time period [23], and execution time [14, 23, 33, 51].

On the other hand, the user acceptance level is often evaluated through subjective measures, such as the Borg CR-10 scale to assess the perceived workload, pressure, or discomfort [12, 19, 23, 51]. The Borg scale ranges from 0 (not perceived at all) to 10 (extremely strong). The user’s experience and the intention to use the exoskeleton instead are usually investigated through the Technology Acceptance Model (TAM) [22, 23]. It consists of a 12-item questionnaire, six regarding the perceived usefulness and the others on the perceived ease of use of the device. In the first half of the test, users are asked to rate the influence of the exoskeleton on task speed, job performance, productivity, effectiveness, and task difficulty using a Likert scale to determine the perceived

usefulness. In the second half, how easily the users learn to interact and use the device correctly is rated. Finally, the System Usability Scale (SUS) is also used to measure the perceived ease of use [12]. It consists of 10 statements to which the user must associate a number between 1 (strongly agree) and 5 (strongly disagree). A SUS score above 70 indicates a good acceptance level.

1.5 The aim of this work

This work of dissertation aims to design and develop a passive upper-limb exoskeleton, based on two MKMs, for assisting workers during a long-lasting overhead task. The two MKMs can be pressurized at a given value and used as pre-loaded non-linear springs.

The exoskeleton must be light and compact, must adapt to the anthropometry of the user, and provide a support torque equal to at least 50 % of the gravitational torque acting on the shoulder during overhead work. In addition, the support torque must be configurable so that it can be adapted to the user's constitution or specific task. The user must be assisted throughout the permitted range of motion and even when holding a tool of about 1 or 2 kg in his/her hands.

The dissertation will present the design, development, and construction of the exoskeleton. Chapter 2 presents the torque generator and the design of the transmission that minimizes the mismatch between the support torque exerted by the exoskeleton and the shoulder gravitational torque. The kinematic chain with two rotational DoFs, which allows the flexion-extension of the arms between 90° and 135° and the abduction-adduction between 0° and 30° is presented in Chapter 3. The axes of rotation of the two joints must be as aligned as possible with the joint axes to ensure the correct functionality of the device. Chapter 4 shows the hardware of the structure, including the adjustment systems necessary to adapt the size of the exoskeleton to the anthropometric characteristics of the user. The sizing of the different parts of the structure and the prototype materials choice are performed through a finite element method (FEM) static analysis. A study of the forces exchanged between the exoskeleton and the user at the contact points is also presented. Preliminary tests that helped verify the resistance to the loads and the functionality of the mechanism are presented in Chapter 5. On the other hand, the exoskeleton effectiveness has been evaluated through experimental tests on volunteer subjects conducted in the laboratory (Chapter 6). Finally, conclusions and suggestions for future work are presented in Chapter 7.

Chapter 2

Design of the torque generator

This section presents the torque generator design, which consists of a passive actuation unit plus a motion transmission.

MKM is chosen as a passive actuation unit among the several mechanical components available to counterbalance gravitational energy due to the advantageous features described in Section 1.2. However, MKM traction force depends on many parameters, such as the MKM diameter and nominal length, the supply pressure, and the contraction ratio (see Section 1.3 for more details). Therefore, commercial MKMs with different diameters and nominal lengths have been considered to identify the muscle with the force-contraction characteristic more suitable for the application. The overall bulkiness is also taken into account. Modeling the MKM behavior is necessary to choose the actuator appropriate for the application. Therefore, in Section 2.1, the static characteristic of two commercial MKMs produced by FESTO is approximated by the Pitei and Tóthová [98] MKM model.

In addition, the transmission significantly affects the device's performance. The torque provided by the actuation unit should be as close as possible to the gravitational torque to properly support the user. Therefore, a transmission able to adapt the MKM characteristics to the gravitational load is required. Three transmission designs are evaluated, aiming at reducing the mismatch between the torque provided by the MKM and the gravitational torque as much as possible. The pneumatic muscles are placed behind the back of the user in all cases, and the traction force is transmitted by a tendon cable that slides on a pulley (configuration A), on a fixed shoulder pad (configuration B), or wraps on a cam that rotates about the shoulder flexion axis (configuration C). The three configurations are described in Sections 2.2, 2.3, and 2.4, respectively. Then, the numerical simulations performed to compare the different MKM-transmission combinations are presented

and discussed in Section 2.5. The system performances are evaluated in the heaviest working conditions to choose the torque generator architecture. In other words, the system behavior is studied by changing the shoulder flexion angle while the elbow is extended. Finally, in Sections 2.6 and 2.7, the torque generator behavior has been evaluated over the entire range of movement (i.e., varying both the shoulder and elbow flexion angle).

2.1 McKibben Muscle

The fluidic muscle DMSP produced by FESTO is selected. The cylindrical inflatable chamber consists of a rubber sheath incorporating a non-crimped fabric made of aramid fibers. The sheath seals the actuator, while the fibers provide reinforcement and power transmission. Among the available DMSP sizes, the DMSP-10 and DMSP-20, with internal diameters equal to 10 and 20 mm, respectively, are considered in this work.

The maximum permissible contraction is 25% of the nominal length for both sizes, while the maximum pre-tensioning increases with the muscle's internal diameter. It is 3% and 4% of the nominal length for DMSP-10 and DMSP-20, respectively. The theoretical force at maximum permissible operating pressure depends also on the actuator's size. It is 630 N (DMSP-10, 8 bar) and 1500 N (DMSP-20, 6 bar). The main characteristics of the selected MKMs are collected in Table 2.1

Table 2.1 Technical data of commercial FESTO McKibben muscles.

	DMSP-10	**DMSP-20**
Internal diameter (mm)	10	20
Nominal length (mm)	40 – 9000	60 – 9000
Max contraction (%)	25	25
Operating pressure (bar)	0 – 8	0 – 6
Maximum force (N)	630	1500

The unknown a_i coefficients of Equation 1.9 are obtained by interpolating the static characteristics provided by the manufacturer with MATLAB Curve Fitting Toolbox. The a_i coefficients are listed in Table 2.2, while the curves obtained with the model are shown in Figure 2.1.

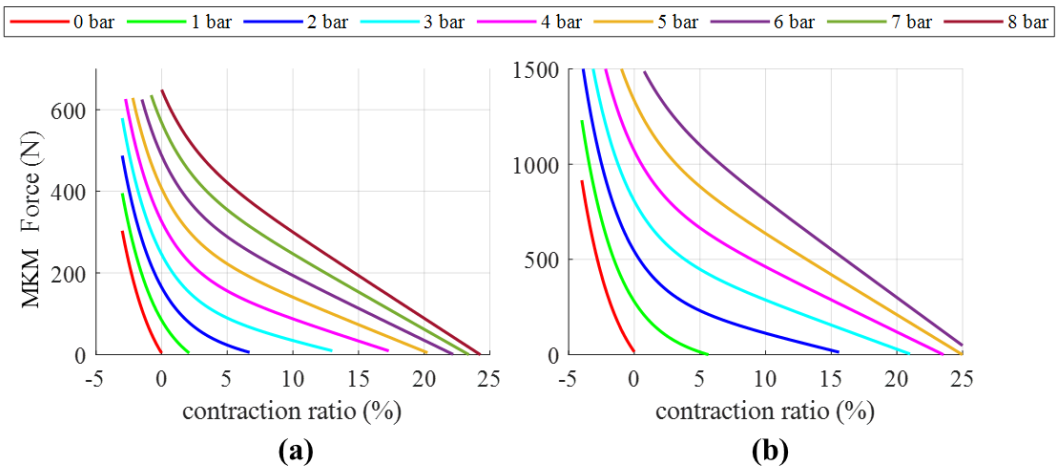

Figure 2.1 Static characteristics of McKibben muscles: DMSP-10 (a); DMSP-20 (b).

Table 2.2 Coefficient of Equation 1.9 for approximating the static characteristics of commercial FESTO McKibben muscles.

	DMSP-10	DMSP-20
a_1	0.01534	0.0524
a_2	130.8	257.6
a_3	-0.3972	-0.3758
a_4	-0.02605	-0.08396
a_5	0.7911	2.583
a_6	-127.1	-242.6

2.2 Configuration A: pulley-based mechanism.

A simple representation of configuration A in the sagittal plane is shown in Figure 2.2. Two MKMs, one for each arm, are on the user's back. Their lower ends are connected to the frame; the upper end of each actuator is instead connected to an inextensible cable that wraps around pulley P and joins the bracelet that supports the subject's arm in point B. Therefore, the MKM traction force is transmitted to the arm bracelets through the cable. Referring to Figure 2.2, a, l, r_b, and α are geometrical characteristics of the device. Specifically, a is the distance between SJC and the pulley, l is the distance between SJC and the bracelet, r_b is the bracelet radius, and α is the angle between a and the vertical axes. On the other hand, b and r are functions of the shoulder flexion angle θ_1 and represent the distance between the pulley (P) and the attachment point of the cable on the bracelet (B) and the lever arm of the MKM force with respect to the SJC, respectively.

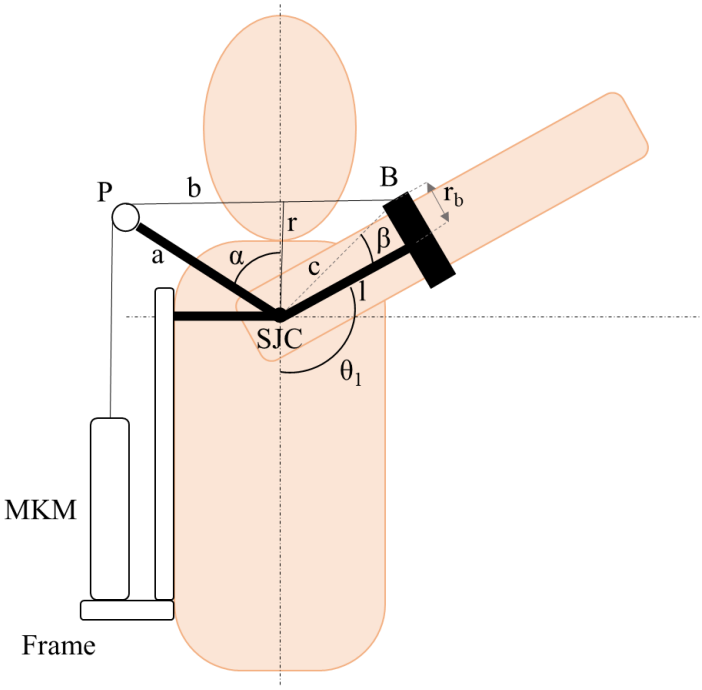

Figure 2.2 Scheme of the pulley-based configuration.

By neglecting the pulley radius, b and r can be calculated as:

$$b = \sqrt{a^2 + c^2 + 2 * a * c * \cos(\theta_1 + \beta - \alpha)} \tag{2.1}$$

$$\beta = \operatorname{atan}\left(\frac{r_b}{l}\right); \qquad c = \frac{l}{\cos(\beta)} \tag{2.2}$$

$$r = \frac{2A}{b} \tag{2.3}$$

$$A = \sqrt{S(S-a)(S-b)(S-c)}; \qquad S = \frac{a+b+c}{2} \tag{2.4}$$

In Equations. 2.1 – 2.4, c is the distance between B and SJC, β is the angle between c and l, A and S are the area and semi-perimeter of the triangle (P-B-SJC), respectively.

The geometrical model of Equations (2.1) - (2.4) requires the definition of parameters a, l, r_b, and α. While l and r_b depend on the anthropometric measure of the user and for a 1.7 m height subject and can be respectively set equal to 0.25 m and 0.06 m, a and α can be varied to optimize the match between exoskeleton support torque and gravitational torque. Moreover, the shortening of the distance Δb will be equal to the MKM contraction for geometric congruity between the inextensible cable and MKM. For each of the two MKMs presented in section 2.1,

the supply pressure, the nominal length, and the initial contraction ratio have been defined to assess the MKM force over the working range.

2.3 Configuration B: shoulder pad-based mechanism.

In configuration B, shown in Figure 2.3, the inextensible cable is again connected between the MKM upper end and the bracelet. However, in this case, the cable slides on a shoulder pad. The latter must be centered in the SJC to avoid the onset of undesired forces and limb movement that could cause discomfort [10, 45].

It should be noted that by raising the arm, the MKM shortens by an amount equal to the variation of b (Figure 2.3). Therefore, both the gravitational torque and the MKM traction force decrease due to the arm elevation. However, they do not do so equally: the MKM traction force decreases more than the gravitational one. Since the reduction in gravitational torque above 90° does not accurately match the decrease in PAM force, the shoulder pad profile has been designed with a variable curvature radius to obtain a force lever arm that increases with the arm lifting to balance the MKM traction force reduction.

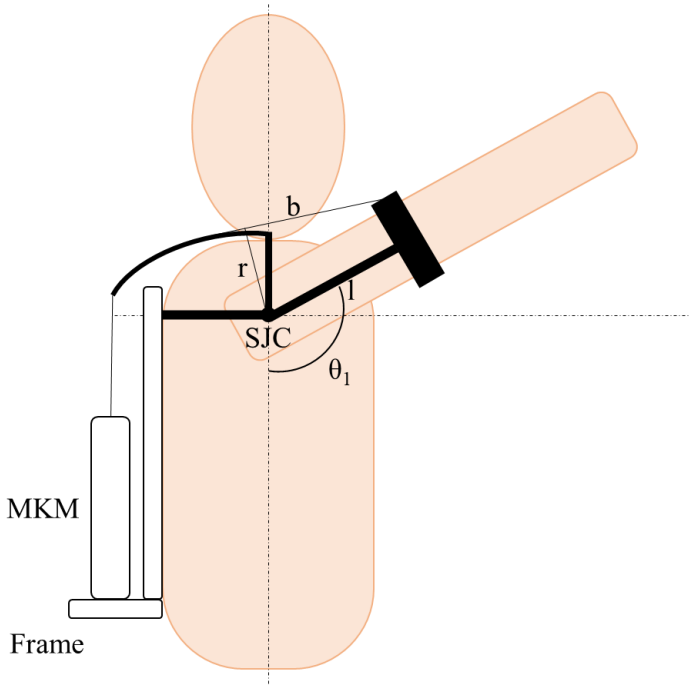

Figure 2.3 Scheme of the shoulder pad-based configuration.

The shoulder-pad profile has been designed through a graphical method to optimize the match between gravitational and support torques. First, the initial shoulder pad radius (θ1 = 90°) has been imposed. To be centered in the SJC without touching the shoulder of the worker, the initial radius must be greater than the distance between the SJC and the acromion (i.e., the highest point of the shoulder complex). This distance is equal to 0.0345 m for a man of medium height [110].

Furthermore, the shoulder pad profile must not exceed the position of the eyes with respect to the shoulder (d = 0.15 m) [34]. For these reasons, 0.045 m has been chosen as the initial cam radius. It coincides with the initial lever arm r_i. This relation is not verified for any other elevation angle. Then, the MKM force lever arm at 135° (r_f) is tuned between 0.065 m and 0.075 m. Higher r_f values are not considered because the shoulder pad could be bulky and hard to integrate into the exoskeleton structure. Once r_i and r_f have been defined, the shoulder pad profile has been obtained graphically by circular interpolation, ensuring its tangency with the cable. At this point, the coordinates of the tangency point, the MKM contraction, and the lever arm at the initial, final, and two other intermediate points (θ_1 = 105°; θ_1 = 120°) can be obtained from the CAD. Finally, interpolating the values measured by the CAD with a fourth-degree polynomial, the pattern of the three mentioned variables is achieved over the entire working range.

The r_f value has been selected to minimize the root mean square error between the gravitational and the exoskeleton assistive torque. The MKM's nominal length, the initial contraction ratio, and the supply pressure must be defined to determine the muscle force. The first variable is set equal to 0.35 m. The supply pressure and the contraction ratio are chosen to obtain forces and contractions achievable by the MKM considered. Regarding DMSP-10 muscle, p and k_i are set equal to 4.5 bar and 2%, respectively. The RMS error was 1.73 Nm with r_f = 0.065 m, 1.36 Nm with r_f = 0.07 m, and 1.40 Nm with r_f = 0.075 m. Concerning DMSP-20 muscle, p and k_i were equal to 2 bar and 4%. The error was 3.53 Nm with r_f = 0.065 m, 3.14 Nm with r_f = 0.07 m, and 3.48 Nm with r_f = 0.075 m.

r_f = 0.07 m provides the best results for both muscles. Increases in the lever arm cannot compensate for the decrease in the traction force caused by muscle contraction above this value. The shoulder pad profile with r_f = 0.07 m is shown in Figure 2.4a alongside the corresponding lever arm r (Figure 2.4b).

In Section 2.5.2, the supply pressure (p), the MKM nominal length (L_{MKM}), and the initial contraction ratio (k_i) values are tuned to minimize the torque error expressed by Equations (2.5) for each of the two MKM presented in Section 2.1.

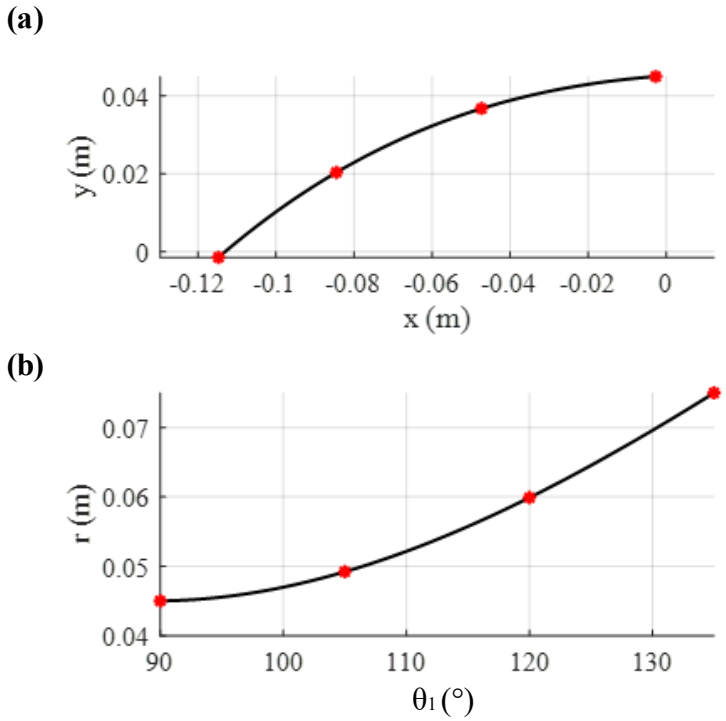

Figure 2.4 (a) Shoulder-pad profile; (b) MKM force lever arm. Red dots represent the data extrapolated from the CAD while the black line is the result of red dots interpolation.

2.4 Configuration C: cam-based mechanism

In configuration C, illustrated in Figure 2.5, one end of the cable is linked to the MKM lower end, while the other end runs inside a sheath attached to the exoskeleton arm via a sheath clip (1) and connects to the cam (2). The latter, in turn, is attached to the strut (3) that supports the bracelet (4). As a result of the MKM contraction, the cam rotates causing the user's arm elevation. The cam adoption attempts to increase the exoskeleton's workspace. Figure 2.5 shows that the cam profile, as well as its capacity to move around the shoulder flexion axis, contribute significantly to diminishing the MKM force lever arm below 90°.

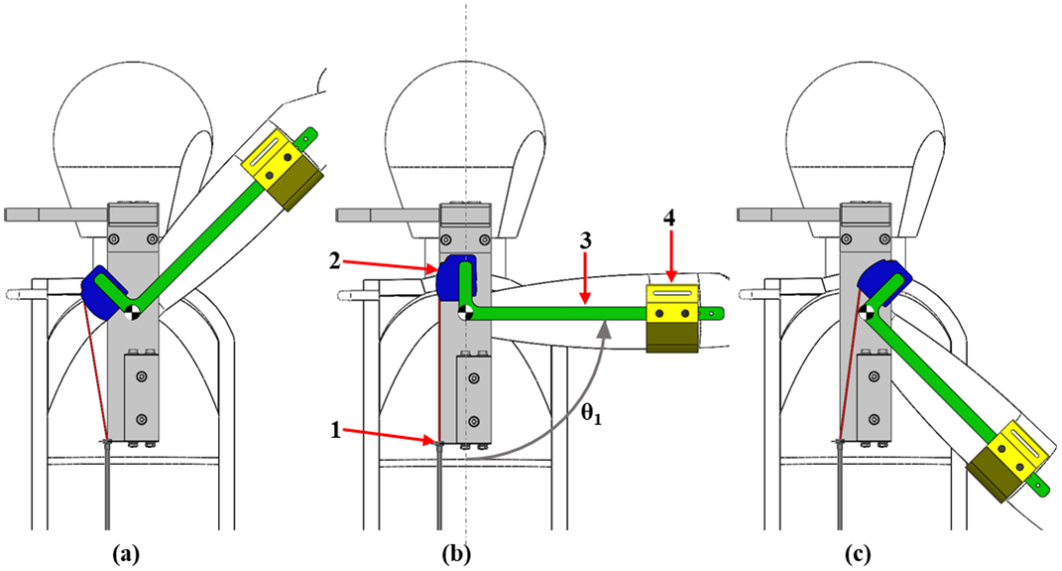

Figure 2.5 Cam-based transmission for different shoulder-flexion angles: (a) $\theta_1 = 135°$; (b) $\theta_1 = 90°$; (c) $\theta_1 = 45°$.

The cam profile that minimizes the mismatch between the gravitational torque and the support torque is again identified through a graphical approach. Referring to Figure 2.6, O is the cam center of rotation, A is the position of the sheath clip, and BC is the cam long axis. To obtain an MKM lever arm that increases as the shoulder flexion angle increases, BC should be vertical if $\theta_1 = 90°$. The OB and OC distances depend on the desired lever arm at the maximum (r_f) and minimum (r_i) flexion angle, respectively. For a defined working range of flexion angle ($\theta_1 \in [45; 135]$), $r_f = 50$ mm. Lower values do not generate an assistive torque sufficient to balance the gravitational ones, while higher values result in a large cam that could obstruct the view. Defined r_f, the OB distance is equal to the distance between O and the intersection (B') between the line passing through O inclined 135° and the tangent to the circumference of radius r_f and passing through A. Conversely, OC and r_i are 10 mm. This value is selected to get force and contraction values that could be achieved by the MKM static characteristics shown in Figure 2.1. The arc BC tangent, at point T, to the line passing through A and distant r_{90} from O can be tracked. r_{90} represents the PAM force lever arm at a 90° shoulder flexion angle. r_{90} is 30 mm. The first part of the cam profile (i.e., the part on which the cable wraps for θ_1 between 90° and 135°) coincides with the TB arc. Finally, the second part of the cam profile, on which the cable wraps for θ_1 between 45° and 90°, has been defined as the arc tangent to both T'B'' (rotated by 45° compared to TB) and the tangent t to the circumference of radius r_i and passing through A. Called T'' the point of intersection between the second arc and the t-line, the total cam profile is T''B''.

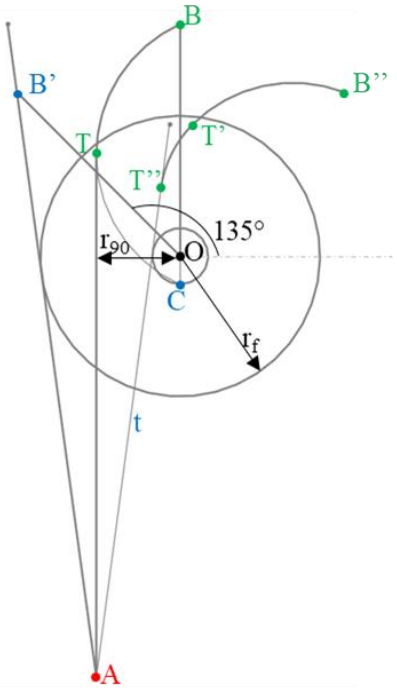

Figure 2.6 Graphical approach to design the cam profile.

The MKM shortening and lever arm are extrapolated from CAD design for six shoulder flexion angles (45°,60°, 75°, 90°, 105°, 120°, 135°). Finally, interpolating the values measured by the CAD with a fourth-degree polynomial, the pattern of the mentioned variables is achieved over the entire working range. The obtained cam profile and the MKM force lever arm are shown in Figure 2.7.

In Section 2.5.3, the supply pressure (p), the MKM nominal length (L_{MKM}), and the muscle contraction ratio at 90° shoulder flexion (k_{90}) values are tuned to minimize the torque error expressed by Equations (2.5) for each of the two MKM presented in Section 2.1

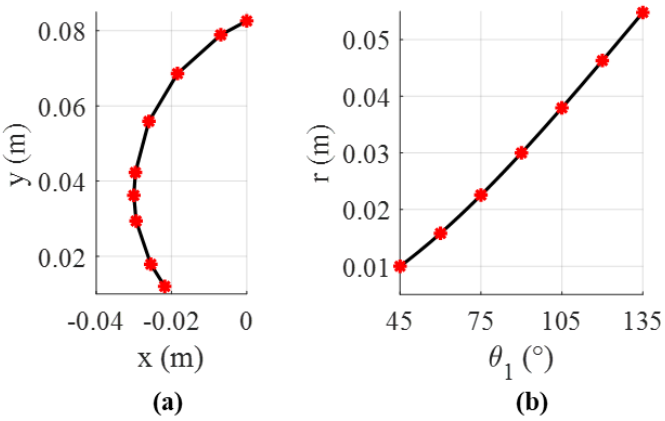

Figure 2.7 Cam profile (a) along with the MKM force lever arm (b). The red dots are the data extrapolated from the CAD while the black line is the result of red dots interpolation.

2.5 Simulation results

Simulations are performed to analyze the two commercial MKMs and the three transmission configurations presented.

The characteristic parameters of each configuration are tuned to minimize the root mean square error (E) between the gravitational torque (M_g) and the support torque (M_{MKM}) expressed in Equation 2.5:

$$E = \sqrt{\frac{1}{N} * \sum_{i=1}^{N} \left(M_{MKM_{(\theta_1)}} - M_{g_{(\theta_1)}} \right)^2} \quad (2.5)$$

N is the number of samples.

The system performance has been evaluated for shoulder elevation angles θ_1 comprised between 90° and 135° for configurations A and B, and between 45° and 135° for configuration C. In addition, the behavior of the three configurations is evaluated in different loaded conditions: unloaded condition, considering only the user's arm weight, and two loaded conditions, in which the user holds a tool of 1 or 2 kg in the hand.

All the simulations have been performed in the MATLAB environment.

2.5.1 Configuration A: pulley-based transmission

Regarding configuration A, different combinations of a, α, p, k_i, and L_{MKM} are performed to find a solution that minimizes the objective function expressed by Equation (2.5). For encumbrance reasons and to avoid contact between the user's shoulder and the pulley, a and α ensure that the vertical distance between the pulley and SJC measures 0.065 m or the horizontal distance is 0.1 m. Thus, the nine pulley positions listed in Table 2.3 have been identified. The pressure upper and lower limits instead depend on the MKM diameter. Higher pressure values are required to provide the proper traction force when a more compact MKM is chosen. The identified pressure ranges are 4-5 bar and 1-2 bar for DMSP-10 and DMSP-20, respectively. Finally, k_i ranged between 0 - 2% and L_{MKM} between 0.20 m and 0.35 m. Muscles with higher nominal lengths are not considered because they would be too bulky to be placed behind the back of the user.

Table 2.3 a and α tested values.

Position	Pulley-SJC vertical distance (m)	Pulley-SJC horizontal distance (m)	a (m)	α (°)
1	0.065	0.01	0.07	22
2	0.065	0.02	0.07	22
3	0.065	0.04	0.08	36
4	0.065	0.06	0.09	44
5	0.065	0.08	0.11	54
6	0.065	0.10	0.12	61
7	0.040	0.10	0.11	69
8	0.020	0.10	0.11	80
9	0.010	0.10	0.11	85

Figure 2.8 shows the influence of the optimized parameters on the torque error for the DMSP-10 (Figure 2.8a) and DMSP-20 (Figure 2.8b).

It can be noted that the DMSP-10 minimizes the effort on the shoulder joint. Among the different parameters to be optimized, the position of the pulley has more influence than the other parameters. Regarding DMSP-10 (Figure 2.8a), by increasing α from 50° to 85° (graph on the left, dotted line), the torque provided by the user to maintain the static balance of the system is reduced by about 5 Nm. The MKM nominal length also affects the exoskeleton performance. The increase of L_{MKM} from 0.2 to 0.35 m decreases the root mean square error by about 4 Nm. Finally, the supply pressure and the initial contraction ratio must be set to 4.2 bar and 0 %, respectively.

Figure 2.9 shows the gravitational torque in the unloaded and loaded conditions, along with the torque values exerted by the MKM in the best parameters configuration (DMSP-10; k_i = 0%; α = 85°; a = 0.11 m; L_0 = 0.35 m) at different supply pressures. As signaled by the curves presented in Figure 2.9, the device action adapts to the weight of the user's arms and operating conditions through appropriate supply pressure regulation. However, the mismatch between gravitational and support torque increases with the load in the hand. The root mean square error between the gravitational and assistive torque in the considered working range passes from 0.53 Nm to 1.74 Nm to 3.22 Nm as the load in the hand increases from 0 to 1 kg to 2 kg.

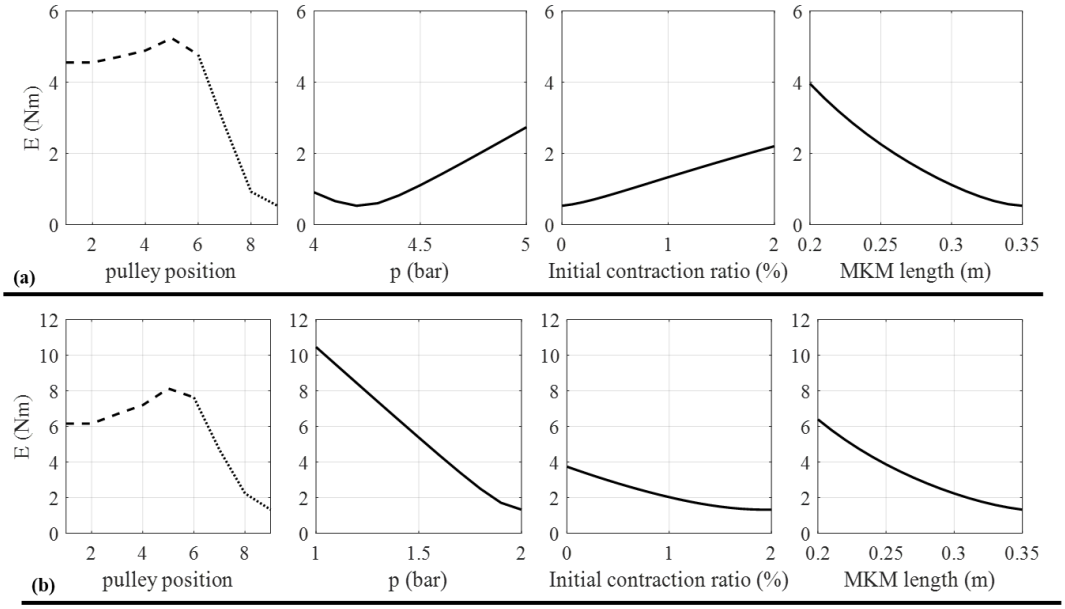

Figure 2.8 Root mean square error between the gravitational torque and the torque generated by the DMSP-10 (a), and the DMSP-20 (b) for different parameter configurations. Data refer to the pulley-based design of the transmission system.

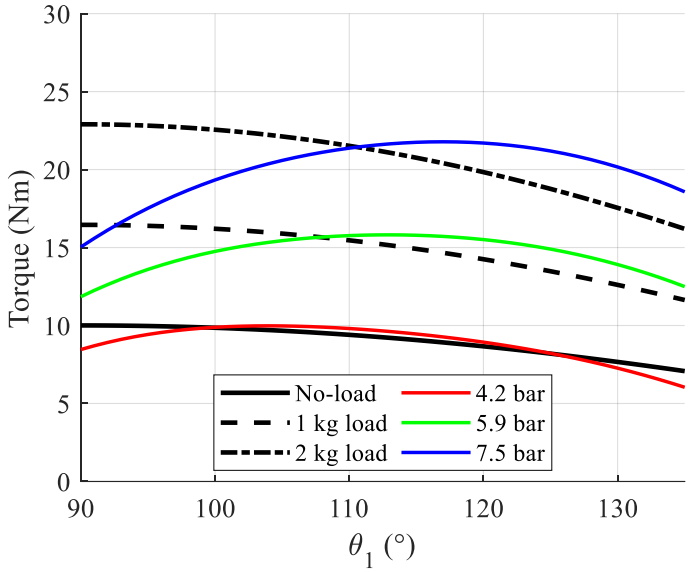

Figure 2.9 Gravitational torque in no-load (black line), 1 kg load (dashed black line), and 2 kg load (dot-dashed black line) condition as well as the torque exerted by the exoskeleton at different supply pressures (colored lines) by employing the DMSP-10 MKM and the pulley-based design of the transmission.

2.5.2 Configuration B: shoulder-pad-based transmission

Regarding configuration B, different combinations of p, k_i, and L_{MKM} are performed to find a solution that minimizes the objective function expressed by Equation 2.5 by considering the shoulder-pad profile shown in Figure 2.4. The upper and lower boundaries of p, k_i, and L_{MKM} are the same as those described in

Section 2.5.1 for the pulley-based mechanism. Figure 2.10 shows the influence of the optimization parameters on the torque error for the DMSP-10 (Figure 2.10a) and DMSP-20 (Fig. 2.10b). The more compact muscle reduces user efforts and provides the best results among the tested MKMs. Unlike configuration A, the error decreases as the contraction ratio increases. Then k_i and L_{MKM} equal to 2% and 0.35 m provide the best performances. The best parameter set has been used to make the curves shown in Figure 2.11. The mismatch between the exoskeleton support torque and the gravitational torque does not worsen as the magnitude of the latter increases. By properly adjusting the supply pressure, the root mean square error between the gravitational and assistive torque is 1.03 Nm, 0.79 Nm, and 1.72 Nm when the load in the hand is 0 kg, 1 kg, and 2 kg, respectively.

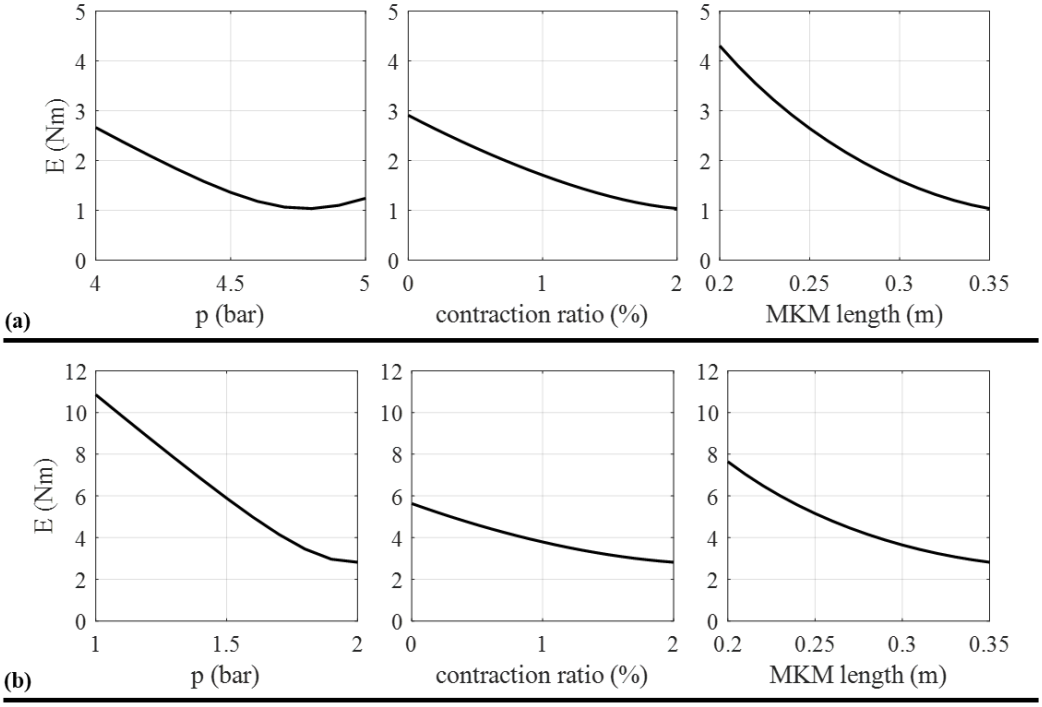

Figure 2.10 Root mean square error between the gravitational torque and the torque generated by the DMSP-10 (a), and the DMSP-20 (b) for different parameter configurations. Data refers to the cam-based design of the transmission system.

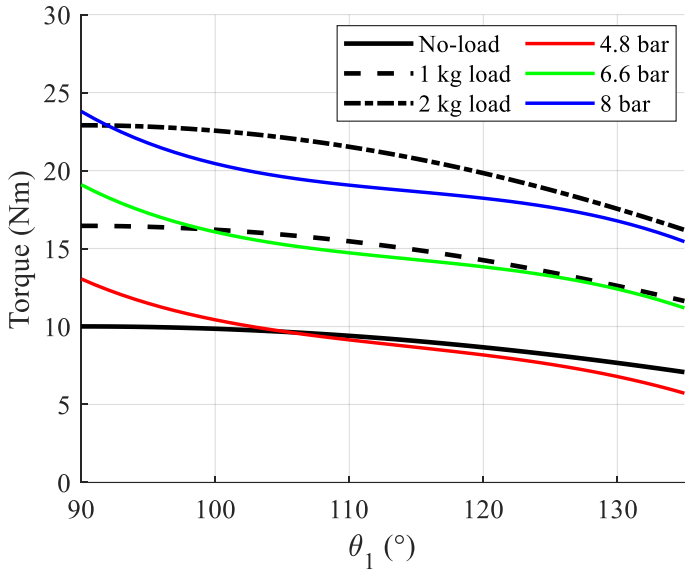

Figure 2.11 Gravitational torque in no-load (black line), 1 kg load (dashed black line), and 2 kg load (dot-dashed black line) condition as well as the torque exerted by the exoskeleton at different supply pressures (colored lines) by employing the DMSP-10 muscle and the shoulder pad-based design of the transmission.

2.5.3 Configuration C: cam-based transmission

Regarding configuration C, different combinations of p, k_{90}, and L_{MKM} are performed to find a solution that minimizes the objective function expressed by Equation 2.5 by considering the cam profile shown in Figure 2.7. The upper and lower boundaries of p, k_{90}, and L_{MKM} are the same as those described in Sections 2.5.1.

Figure 2.12 shows the influence of the optimization parameters on the torque error for the DMSP-10 (Figure 2.12a) and DMSP-20 (Fig. 2.12b). Once again, the more compact muscle reduces user efforts and provides the best results among the tested MKMs. The effect of optimized parameters on the torque error is similar to that observed in configuration B. The best performance is obtained with k_{90} and L_{MKM} equal to 2% and 0.35 m, respectively. The best parameter set has been used to make the curves shown in Figure 2.13. In the unloaded condition, configuration C allows accurate tracking of the gravitational torque in an extended range of movement. However, the exoskeleton assistive action worsens as the load in the hand increases. The root mean square error between the gravitational and assistive torque goes from 0.34 Nm to 1.41 Nm, to 5.60 Nm when the load in the hand is 0 kg, 1 kg, and 2 kg, respectively.

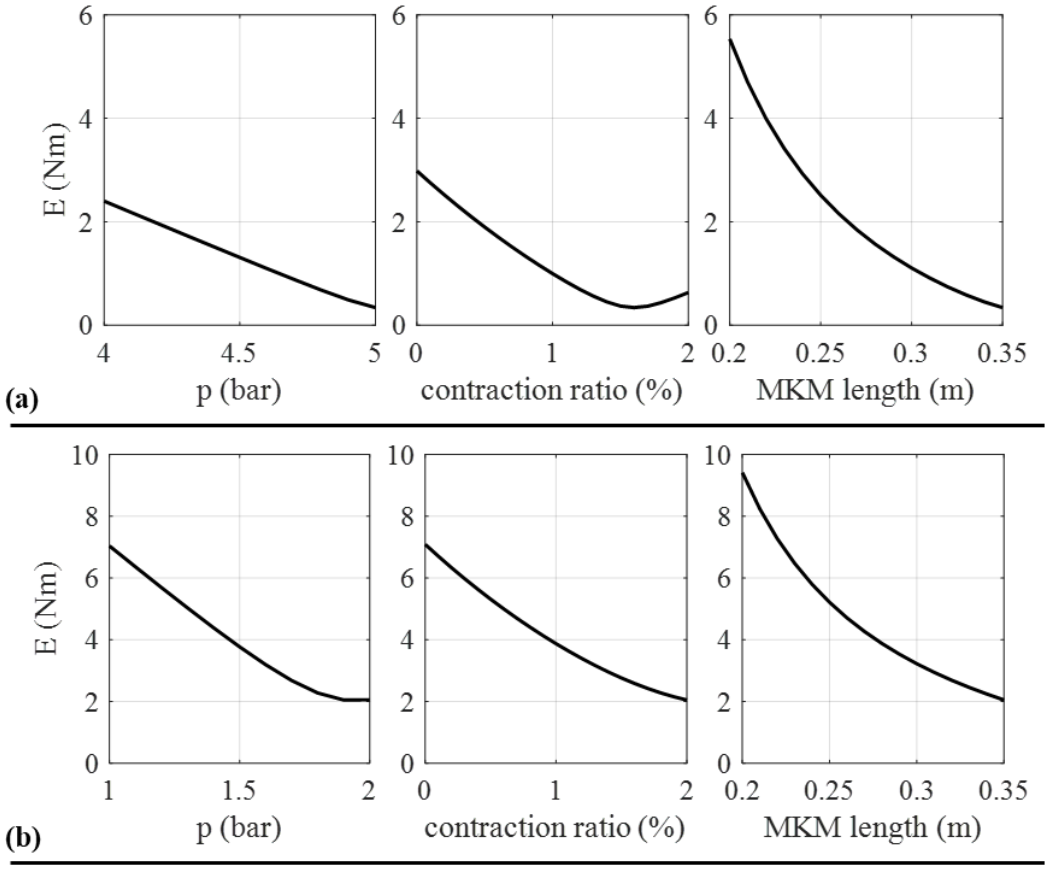

Figure 2.12 Root mean square error between the gravitational torque and the torque generated by the DMSP-10 (a), and the DMSP-20 (b) for different parameter configurations. Data refers to the cam-based design of the transmission.

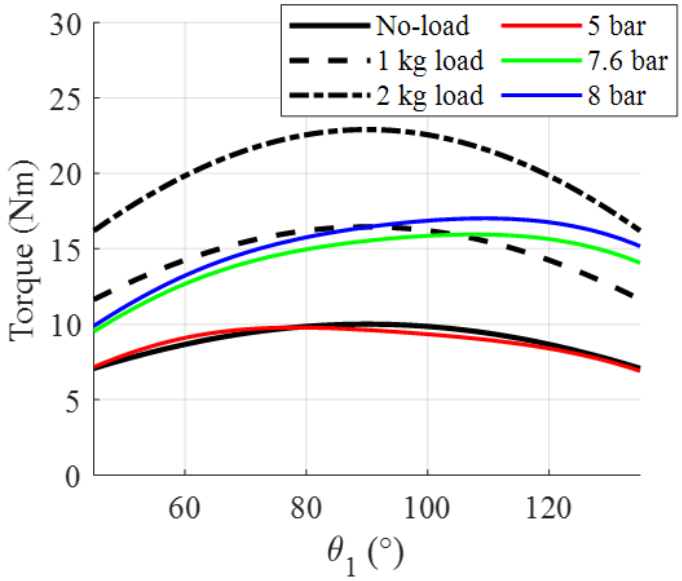

Figure 2.13 Gravitational torque in no-load (black line), 1 kg load (dashed black line), and 2 kg load (dot-dashed black line) condition as well as the torque exerted by the exoskeleton at different supply pressures (colored lines) by employing the DMSP-10 MKM and the cam-based transmission.

2.5.4 Conclusion

Configuration C is the most convenient in terms of operating range. In the unloaded conditions, the exoskeleton appropriately supports the user for shoulder flexion angles between 45° and 135°, while in the other two configurations, the working range is limited between 90° and 135°. Below 90°, the torque generated by configuration A decreases faster than the gravitational torque, so the support action of the exoskeleton fails. The support torque provided by configuration B instead increases, so the user should apply considerable muscle force to lower the arms.

On the other hand, the performance of both configurations A and C worsens as the gravitational torque increases. The torque generator is not able to adequately balance the gravitational torque under loaded conditions, even at the maximum permissible supply pressure. Only configuration B allows to adapt the device action to the operating conditions through adequate supply pressure regulation.

Among the presented solutions, the configuration B is also the most promising in reducing the system footprint. The shoulder pad does not require the presence of a support bar like that shown in Figure 2.2. In addition, thanks to its size, the shoulder pad can be mounted above the user's shoulder, while the cam should be placed laterally. Therefore, configuration C results in a more complex and bulky structure as well as cause a parasitic abduction torque on the user's shoulder.

In conclusion, a transmission based on a cable sliding on a shoulder pad is particularly convenient since it adequately supports the user within a workspace large enough to accomplish most of the working tasks regardless of load condition. For these reasons, it will be the only one further developed in this work.

2.6 PAM static experimental characteristic

The most suitable MKM (DMSP-10-350N-RM-CM, Festo AG & Co. KG, Esslingen am Neckar, Germany), identified in Section 2.4, has been experimentally characterized to validate the theoretical relationship between pressure, tensile force, and contraction ratio shown in Figure 2.1a.

The MKM static characterization can be carried out at constant load (isotonic test) or constant length (isometric test). In the first case, only one end of the actuator is fixed, while the other is free to move and connected to a known load kept constant while the supply pressure and the MKM length vary during the test. In the other case, both MKM extremities are fixed to a rigid frame: the MKM length is constant, while the other two parameters vary during the test.

The isotonic test better reproduces the MKM working condition since the MKM length changes during user arm elevation. Therefore, the test bench shown in Figure 2.14 is built to obtain the MKM static characteristics.

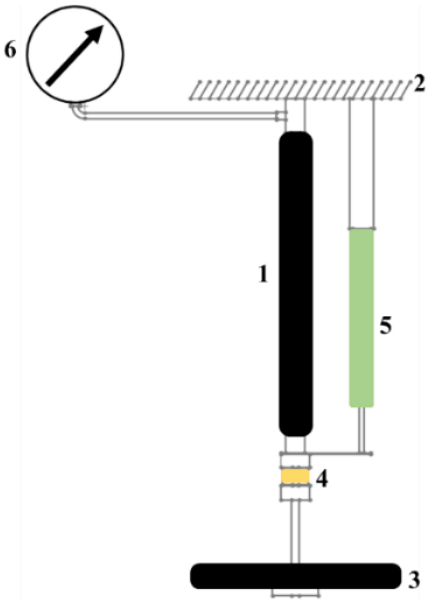

Figure 2.14 Sketch of the test bench developed to characterize the MKM.

The MKM (1) upper end is screwed to a fixed frame (2), while its lower end is connected to an external load (3). A uniaxial load cell (UMM, 100 kgf, Dacell Co. Ltd., Cheongju, Korea) (4) mounted between the muscle and the external weight measured the MKM tensile force. In addition, a linear displacement transducer (PZ-34-A-100, Gefran S.p.A., Provaglio D'Iseo, Italy) (5) is linked in parallel to the MKM to measure its length variation. Finally, the supply pressure is manually adjusted through a reducer and measured through a pressure gauge (6) installed near the muscle. The signals of the transducers are acquired through a digital multimeter.

The progressive sequence of loads from 0 to 60 kg listed in Table 2.4 is applied to the MKM. For each load, the supply pressure is increased from a minimum pressure value to 8 bar in steps of 1 bar and then reduced to the initial pressure value. The minimum pressure values are imposed so as not to exceed an elongation of 3% of the MKM nominal length, as recommended by the manufacturer.

The experimental static characteristic, shown in Figure 2.15a, is slightly different from that in Figure 2.1a. The maximum contraction ratio is greater than 25%, and there is a bit of hysteresis. The latter can be attributed to the elastomeric chamber deformation, the rearrangement of the fibers constituting the net surrounding the elastomeric chamber, and the friction between the net and the chamber. The hysteresis error decreases as the supply pressure increases, and it is lower than 10% of the full scale in the exoskeleton working range ($p > 4$ bar) (Figure 2.15b).

Table 2.4 Static characterization data. m is the external load; p is the supply pressure; ks and kd are the contraction ratio measured during the up and down pressure cycle, respectively.

m (kg)	p (bar)	k_{up} (%)	k_{down} (%)	m (kg)	p (bar)	k_{up} (%)	k_{down} (%)
0	0	0.0	1.2	4	0	-1.6	-1.3
	1	1.4	5.2		1	-0.9	0.5
	2	5.9	13.3		2	1.7	5.7
	3	14.4	19.5		3	7.6	12.6
	4	20.0	22.7		4	13.6	17.2
	5	22.8	24.9		5	17.5	20.2
	6	25.1	26.2		6	20.1	22.1
	7	26.7	27.1		7	22.1	23.4
	8	27.8	27.8		8	24.2	24.2
10	0	-2.4	-1.9	20			
	1	-1.8	-0.8		1	-2.6	-2.3
	2	0.0	2.7		2	-1.5	-0.6
	3	3.9	6.3		3	0.3	1.7
	4	9.3	12.4		4	3.2	5.5
	5	13.6	15.7		5	7.6	9.5
	6	16.8	18.1		6	11.4	12.5
	7	19.3	20.0		7	14.4	14.8
	8	20.9	20.9		8	16.7	16.7
30	2	-2.7	-2.1	40			
	3	-1.6	-0.7		3	-3.0	-2.4
	4	0.1	1.5		4	-2.0	-1.1
	5	2.8	4.5		5	-0.5	0.7
	6	6.1	7.3		6	1.8	3.1
	7	9.5	10.0		7	4.7	5.7
	8	12.2	12.2		8	7.5	7.5
50	4	-2.9	-2.3	60			
	5	-1.9	-1.1		5	-2.9	-2.5
	6	-0.5	0.4		6	-2.0	-1.4
	7	1.5	2.4		7	-0.7	-0.1
	8	4.0	4.0		8	1.1	1.1

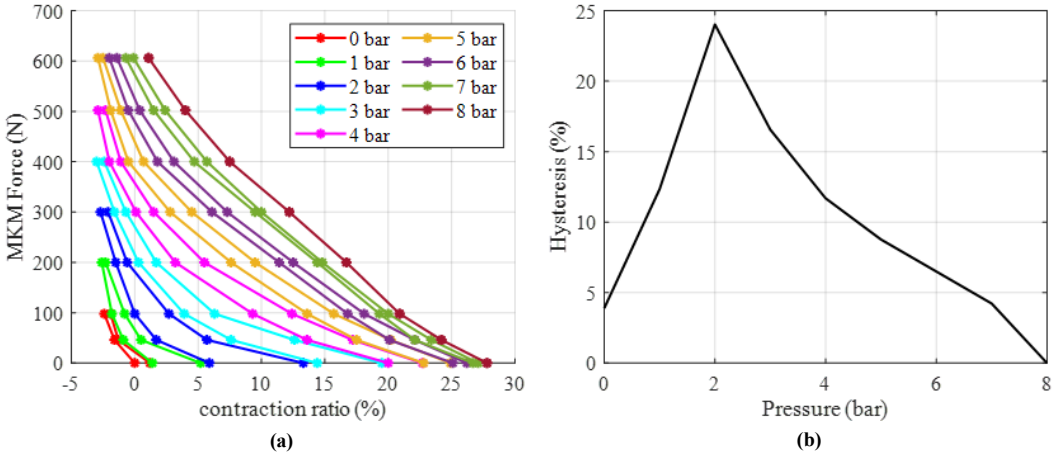

Figure 2.15 (a) FESTO DMSP-10-350N-RM-CM experimental static characteristic (b) MKM hysteresis error expressed as a percentage of the contraction ratio range.

Finally, the experimental data are used to recalculate the six coefficients a_i of Eq. 2.1. The a_i values and the corresponding curves are listed in Table 2.5 and shown in Figure 2.16, respectively.

Table 2.5 Coefficient of Equation 1.9 for approximating the experimental static characteristics of commercial FESTO McKibben muscles (DMSP-10-350N-RM-CM).

	DMSP-10
a_1	0.01823
a_2	110.8
a_3	-0.3065
a_4	-0.02541
a_5	0.8416
a_6	-129

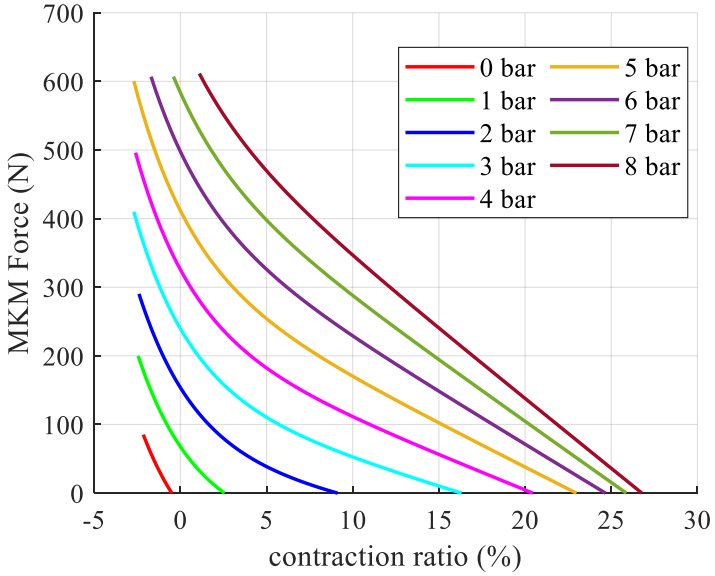

Figure 2.16 Mathematical interpolation of the FESTO McKibben muscles experimental static characteristic

2.7 Workspace evaluation

This section evaluates the support torque provided by the shoulder pad-based transmission with the characterized actuator for different shoulder and elbow flexion angles. The shoulder elevation angle θ_1 varied between 90° and 135° while the elbow flexion angle θ_2 varied between 0° and 90°.

First, the supply pressure values that minimize the error between the gravitational and the exoskeleton support torque have been recalculated, and the results are shown in Figure 2.17. The comparison between Figure 2.11 and Figure 2.17 highlights that the supply pressure and the mismatch between the gravitational and support torque decrease with the experimental characteristics. In particular:

- In the unloaded condition, the best supply pressure decreases from 4.8 bar to 4.3 bar while the root mean square error between the gravitational and assistive torque decreases from 1.03 Nm to 0.86 Nm.
- With 1kg in the user's hand, the best supply pressure decreases from 6.6 bar to 6 bar and the error from 0.79 Nm to 0.66 Nm.
- With 2kg in the user's hand, the best supply pressure decreases from 8 bar to 7.7 bar and the error from 1.72 Nm to 0.95 Nm.

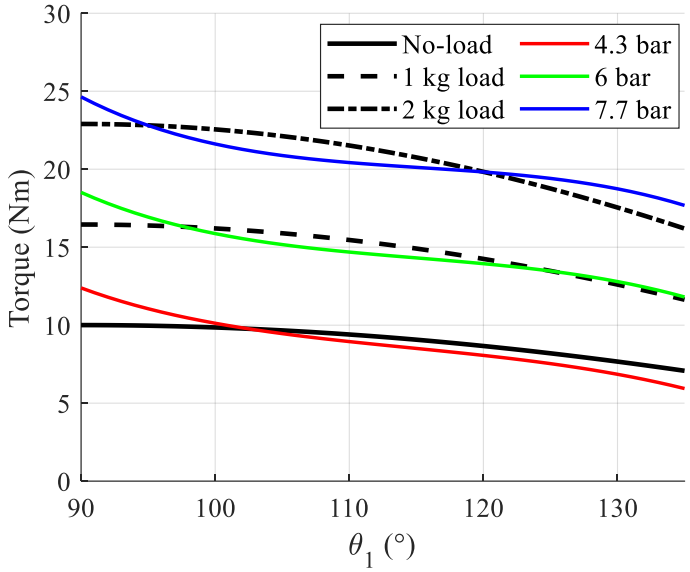

Figure 2.17 Gravitational torque in no-load (black line), 1 kg load (dashed black line), and 2 kg load (dot-dashed black line) condition as well as the torque exerted by the exoskeleton at different supply pressures (coloured lines) by employing the MKM experimental characteristic and the shoulder pad-based design of the transmission.

It should be noted that the MKM is pressurized at almost the maximum allowable supply pressure to balance the gravity in the 2 kg load condition. Therefore, the DMSP-10 is not able to fully balance the gravitational torque if the additional load in the user's hand exceeds 2 kg. However, since the exoskeleton

aims to support the user during lightweight repetitive tasks, it is appropriate for the application.

The assistance level (AL) provided by the exoskeleton is then evaluated for several combinations of shoulder and elbow flexion angles. The absolute difference between the gravitational torque (M_g, shown in Figure 1.5) and the exoskeleton assistive torque (M_{MKM}) is calculated for each position of the theoretical workspace. After that, the absolute difference is expressed as a percentage of the gravitational torque at the shoulder (Eq 2.6).

$$AL_{\%} = \left(1 - \frac{\left|M_{g_{(\theta_1,\theta_2)}} - M_{MKM_{(\theta_1,\theta_2)}}\right|}{M_{g_{(\theta_1,\theta_2)}}}\right) \cdot 100 \qquad (2.6)$$

The assistance level, shown in Figure 2.18, has been evaluated for different loading conditions.

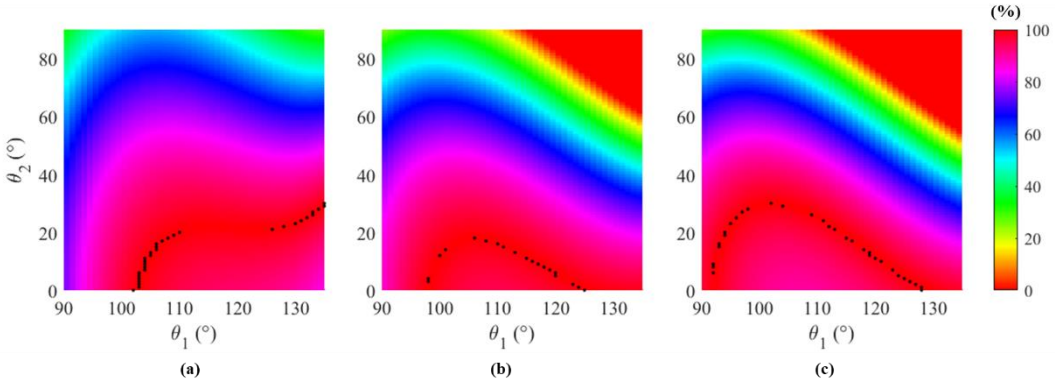

Figure 2.18 Percentage of the gravitational torque provided by the exoskeleton in the unloaded condition (a) and with 1 kg (b) and 2 kg (c) in the hand. The MKM supply pressure is equal to 4.3 bar (a), 6 bar (b), and 7.7 bar (c). Black dots represent the static equilibrium in which the exoskeleton provides 100% of the torque needed to keep the arm in that position.

Regarding the unloaded condition (Figure 2.18a), the exoskeleton balances at least 70% of the shoulder gravitational torque in almost the entire working range. In the loaded conditions (Figure 2.18b-c), the working range in which the support action is more than 70% shrinks. At such high supply pressures, even slight variations in the tensile force of MKM generate a considerable MKM length and shoulder elevation angle variation. However, the support action is higher than 60% in more than half the working range. It falls below 20% only for combinations of shoulder and elbow flexion angles that would carry the hands exactly above the head, which are not a position generally taken during work activities.

Finally, the system behavior for elevation angles less than 90° has been studied. Below 90 °, the support torque lever arm remains almost constant while the MKM

length and its traction force increase. As a result, the support torque provided by the exoskeleton increases. Conversely, the gravitational torque is reduced. Therefore, the user must apply considerable muscle force to compensate for the mismatch between the gravitational torque (Figure 2.19, black line) and the exoskeleton torque at the pressure of 4.3 bar (Figure 2.19, red line). As a consequence, the exoskeleton operating range is limited to flexion angles greater than 90°. A supply pressure reduction (Figure 2.19, blue line) or an MKM release mechanism shall be integrated into the exoskeleton to allow the user to easily reach the arm resting position.

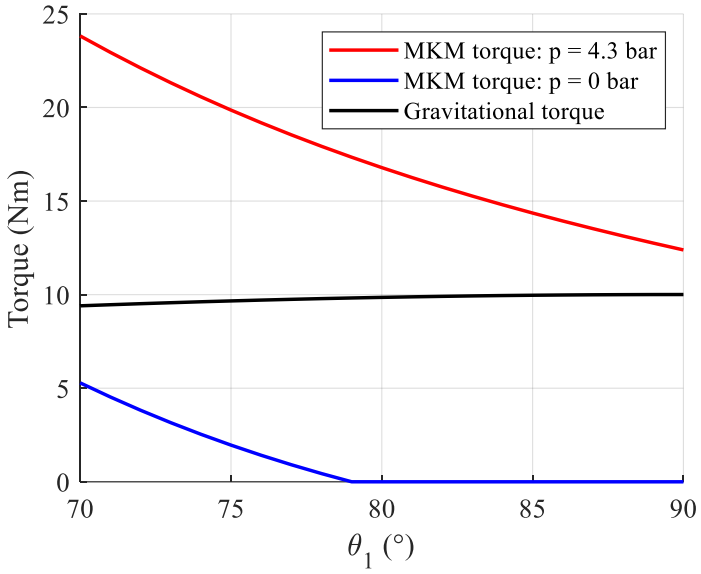

Figure 2.19 System behavior for elevation angles less than 90°. The black line represents the gravitational torque in the unloaded condition while the colored lines represent the MKM torque at different supply pressures.

Chapter 3

The kinematic chain

This section presents the kinematic chain design that must allow an arm range of movement appropriate for the considered application.

A driving goal of the exoskeleton is to assist workers during overhead activities, maintaining the structure of the exoskeleton compact and simple. Therefore, a kinematic chain with only two rotational DoFs has been designed. The first one consists of a hinge with a horizontal axis aligned with the shoulder flexion-extension axis to guarantee shoulder flexion between 90° and 135°. The other is a vertical hinge axis aligned with the shoulder abduction axis to ensure horizontal plane abduction between 0° and 30°.

As stated in Section 1.1.1, the shoulder can be modelized as a 5 DOFs mechanism due to the SJC movement during arm elevation. A 2 DOF upper limb exoskeleton has the advantage of being compact and simple. Still, misalignment between exoskeleton and limb rotation axes inevitably occurs during arm movement due to the oversimplified exoskeleton's kinematic chain compared to the limb one. Any offset between SJC and the exoskeleton joint center (ExoJC) causes the displacement of the bracelet along the upper arm. The bracelet displacement induces the onset of shear forces on the user's arm and, at the same time, affects the exoskeleton's performance. Misalignment magnitude and its effects are presented and discussed in Section 3.1. The mechanical design of the joints is instead presented in Section 3.2.

3.1 Joint misalignment

As stated in Section 1.1.1, the SJC position depends on the shoulder flexion angle. SJC moves about 2.8 cm upwards (Figure 3.1 blue line) and 0.3 cm medially (Figure 3.1 black line) in the working range considered.

For the sake of simplicity and considering the limited displacement in the mediolateral direction, the misalignment effects on the abduction-adduction joint may be overlooked. Therefore, this section focuses on the consequence of the misalignment between SJC and the exoskeleton flexion-extension joint center in the sagittal plane.

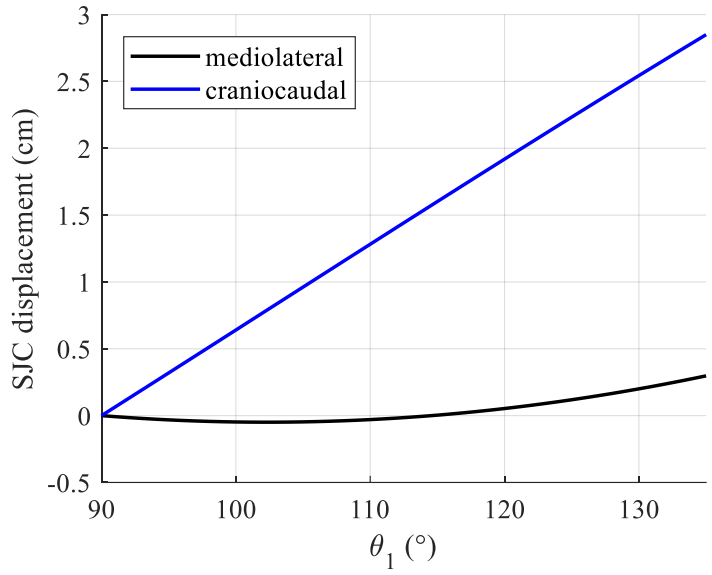

Figure 3.1 Upward (blue line) and medially (black line) SJC translation in the exoskeleton working range calculated considering a man of 1.7 m.

SJC and the exoskeleton joint (ExoJC) are supposed to coincide when the shoulder flexion angle is 90°. In addition, a rigid fixing of the exoskeleton frame on the user trunk and a compliant fixing of the exoskeleton bracelet on the upper arm is assumed. As the user lifts the arm, SJC moves upwards while ExoJC is fixed. As a result, the bracelet moves along the upper arm to allow shoulder flexion and generates shear stresses between the bracelet and the upper arm. This scenario is modeled as a static mechanical issue in Figure 3.2.

The known parameters are the shoulder elevation angle θ_1 and the length of the exoskeleton link l (i.e., the distance between the bracelet and ExoJC, l = 0.25 m). The offset Δy between SJC and ExoJC can be calculated by Equation 1.1 by imposing a perfect alignment between ExoJC and SJC when $\theta_1 = 90°$. On the other hand, the angle β between the exoskeleton link and the horizontal axes, the distance l_v between SJC and the bracelet, and the bracelet displacement d along the upper arm vary with θ_1 and can be obtained by the geometry (Equations 3.1 – 3.3).

$$\left(-\frac{l}{\tan(\theta_1)}-\Delta y\right)*\tan^2\left(\frac{\beta}{2}\right)+2*l*\tan\left(\frac{\beta}{2}\right)-\frac{l}{\tan(\theta_1)}-\Delta y=0 \qquad (3.1)$$

$$l_v = \frac{l * \cos(\beta)}{\sin(\theta_1)} \tag{3.2}$$

$$d = l - l_v \tag{3.3}$$

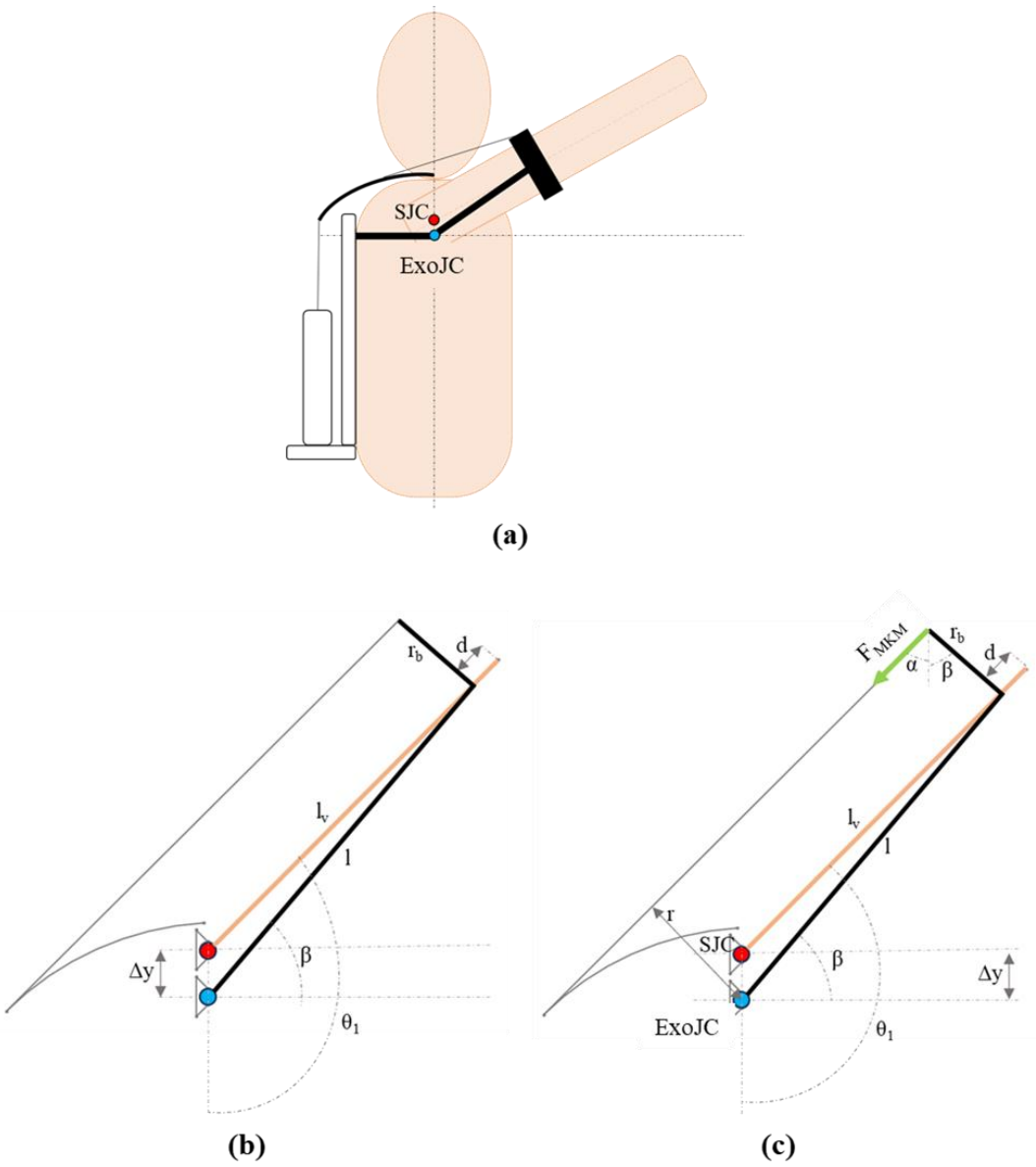

Figure 3.2 Illustration of a joint misalignments between exoskeleton and the human limb (a). The analytical model to assess the magnitude of constraints displacements d (b) and the exoskeleton support torque (c).

The interaction force produced by the misalignment is transmitted to the soft tissues of the user. Its value can be estimated if d is known, and a human-exoskeleton interface model is imposed. From a mechanical point of view, soft tissues can be described as viscoelastic elements in which the induced force is

proportional to its deformation and deformation rate. The shear force F_d, applied on the arm can be evaluated through Equation 3.4 in which k_{arm} and b_{arm} represent the stiffness and damping of the human-exo contact surface, so they must consider both the soft tissue composition and the exoskeleton bracelet constitutive material.

$$F_d = k_{arm} * d + b_{arm} * \dot{d} \tag{3.4}$$

The shear force F_d, shown in Figure 3.3, is estimated in quasi-static condition ($\dot{d} = 0$) and setting k_{arm} equal to 222 N/m according to the literature [48]. It can be seen that F_d is less than 5 N in the entire working range and does not pose a danger to the user.

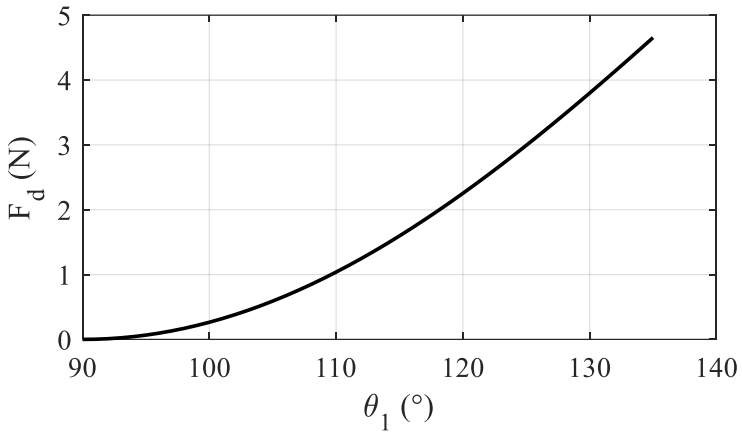

Figure 3.3 The estimated shear force at the bracelet-upper arm interface.

The distance d allows to determine the exact location of the contact point between the upper arm and the exoskeleton. This, in turn, aids in identifying the torque transmitted to SJC via the bracelet. The diagram shown in Figure 3.2 (c) highlights that as the misalignment between the two joints increases, the lever arm of the MKM traction force is reduced. In the new condition, the support torque can be calculated as expressed by Equation 3.5:

$$M_{MKM} = (F_{MKM} * \sin(\alpha) * (-l_v * \cos(\theta_1) + r_b * \cos(\beta)) - (F_{MKM} * \cos(\alpha) * (l_v * \sin(\theta_1) - r_b * \sin(\beta)) \tag{3.5}$$

$$\alpha = \operatorname{asin}\left(\frac{r}{\sqrt{l^2 + r_b^2}}\right) + \operatorname{asin}\left(\frac{l}{\sqrt{l^2 + r_b^2}}\right) - \beta \tag{3.6}$$

Figure 3.4 shows the percentage of the gravitational torque provided by the exoskeleton taking into account the SJC-ExoJC misalignment.

The assistance level is greater than 80% in a narrower workspace with respect to the perfect alignment cases (Figure 2.18). At the same time, the workspace where the support torque is less than 60% also decreases. In addition, the static equilibrium is reached at a lower elbow flexion angle as the load in the hand increases. This exoskeleton behavior could induce a change in the user arm kinematic arrangement during the exoskeleton usage session. In the loaded conditions, lower elbow flexion angles may be preferred to reach the same hand position with respect to the unloaded condition.

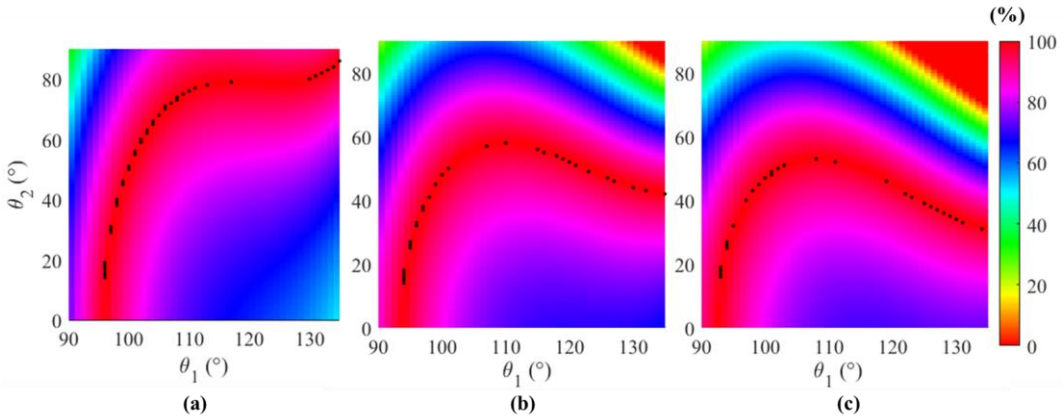

Figure 3.4 Percentage of the gravitational torque provided by the exoskeleton in the unloaded condition (a) and with 1 kg (b) and 2 kg (c) in the hand, taking into account SJC-ExoJC misalignment. Black dots represent the static equilibrium of the system (i.e., the exoskeleton provides 100% of the torque needed to keep the arm in that position).

Since the exact location of SJC is unknown, SJC and ExoJC may not be perfectly aligned even in the initial position. Therefore, the effect of the eight different initial ExoJC positions, represented in Figure 3.5, on the exoskeleton support action has been evaluated. Each of them is at a distance of 1 cm from SJC.

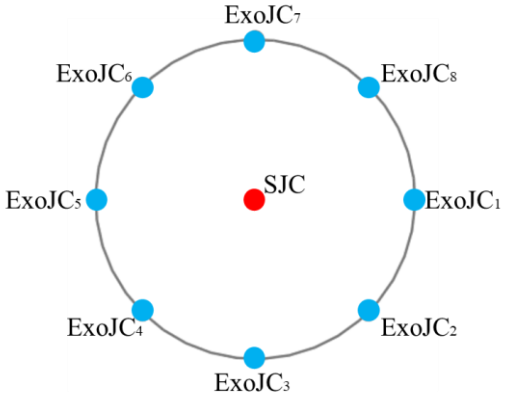

Figure 3.5 Maps of the ExoJC positions

For each ExoJC position, the percentage of gravitational torque balanced by the exoskeleton is shown in Figure 3.6. The maximum shear stress applied on the user's arm at the contact point with the exoskeleton is instead represented in Figure 3.7.

The performance worsened compared to the case in which a perfect initial alignment is assumed (Figure 3.4a). In particular, if ExoJC is over SJC (Figure 3.6 f, g, h), the exoskeleton does not effectively support the user if the shoulder and elbow flexion angles are simultaneously close to 90°. In these cases, the support torque is about twice the gravitational torque of the shoulder. As a consequence, the subject must push down the exoskeleton bracelet to avoid the upper arm elevation. Therefore, the reduction of the activity of the shoulder flexor muscles would occur at the expense of an excessive increase in the activity of the extensor muscles.

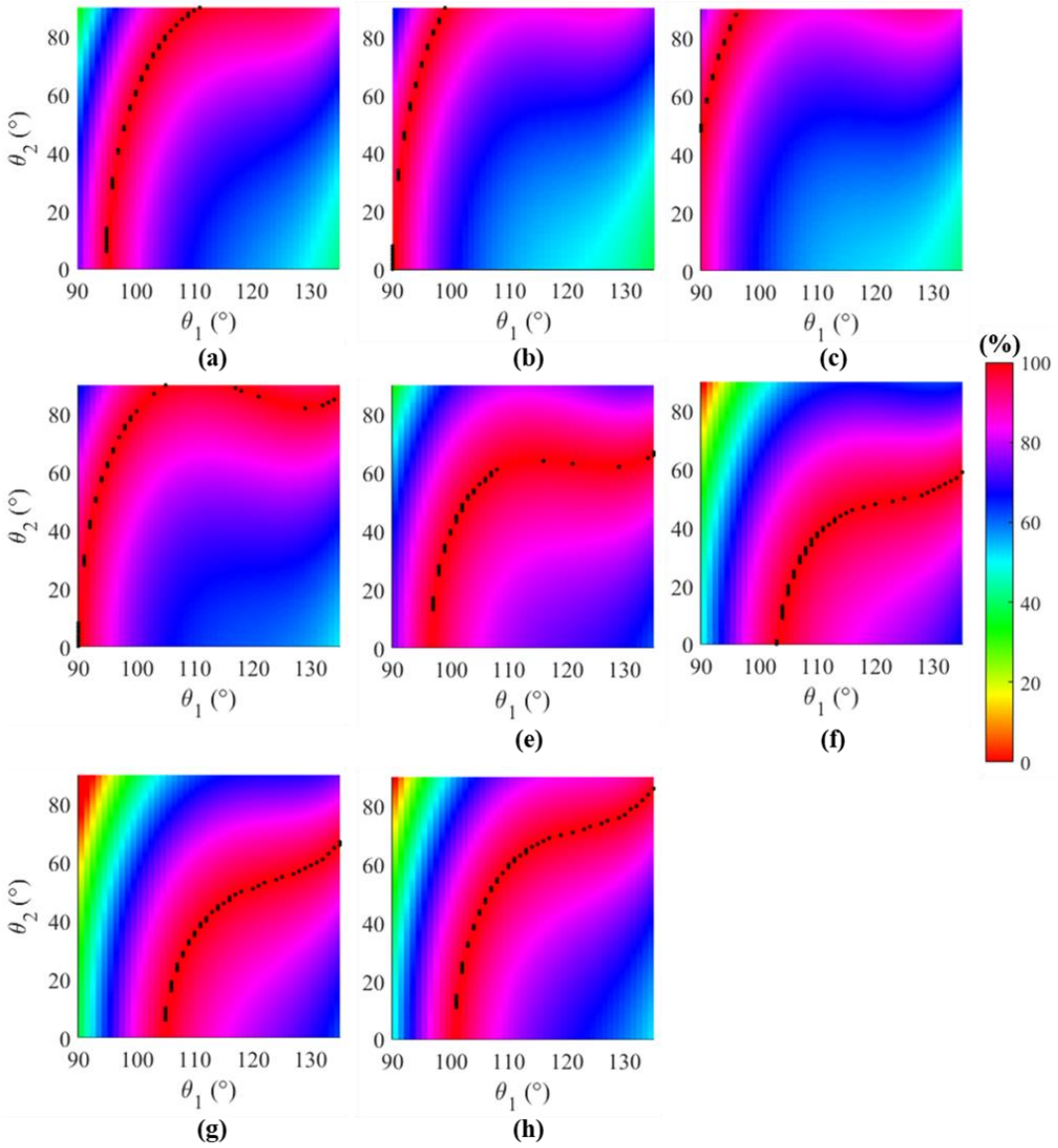

Figure 3.6 Percentage of the gravitational torque provided by the exoskeleton for different ExoJC positions: $ExoJC_1$ (a); $ExoJC_2$ (b); $ExoJC_3$ (c); $ExoJC_4$ (d); $ExoJC_5$ (e); $ExoJC_6$ (f); $ExoJC_7$ (g); $ExoJC_8$

(h). Black dots represent the static equilibrium of the system (i.e., the exoskeleton provides 100% of the torque needed to keep the arm in that position).

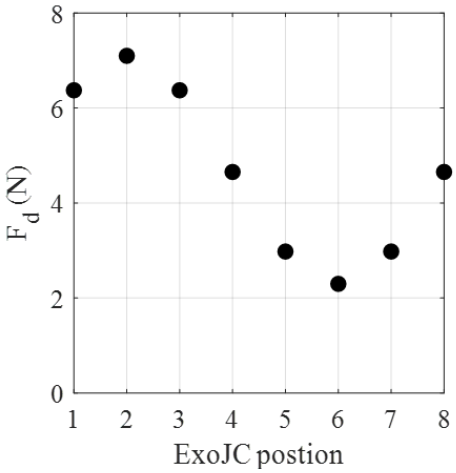

Figure 3.7 The estimated shear force magnitude for the different ExoJC position illustrated in Figure 3.5.

In general, except for some specific positions, the exoskeleton addresses quite well with misalignments, and the support torque is higher than 50% in most working conditions. Moreover, the shear force acting on the arm (Figure 3.7) does not reach excessive values.

3.2 Exoskeleton joints mechanical design

As stated before, the kinematic chain must allow shoulder flexion between 90° and 135° and shoulder horizontal abduction up to 30°. In addition, to ensure the correct functionality of kinematics, the rotation axes of these two joints must be orthogonal and, as much aligned as possible with the anatomical joint axes when the shoulder is 90° flexed.

The shoulder pad and bracelet positions must also comply with certain project specifications.

The shoulder pad must be placed over the shoulder of the user. If the shoulder pad is not above SJC, the distance between the cable and SJC on the transverse plane would give rise to a parasitic torque that would abduct the user's arm.

For the same reason and to reduce both the friction due to a misalignment between the shoulder pad profile and the cable, and the probability that the cable slips off the shoulder pad, it is necessary that the latter follows the arm abduction.

Finally, the shoulder pad must not be in contact with the shoulder of the user in order not to hinder arm flexion and to prevent the cable tension forces from being discharged onto the shoulder of the user.

On the other hand, the bracelet must be connected to the flexion-extension joint through a rigid link to prevent it from translating along the longitudinal arm direction due to the traction force exerted by the wire.

A universal joint, shown in Figure 3.8 and Figure 3.9, consisting of two arches and two bushings held in place by Seager rings is first proposed to meet the above-mentioned project features.

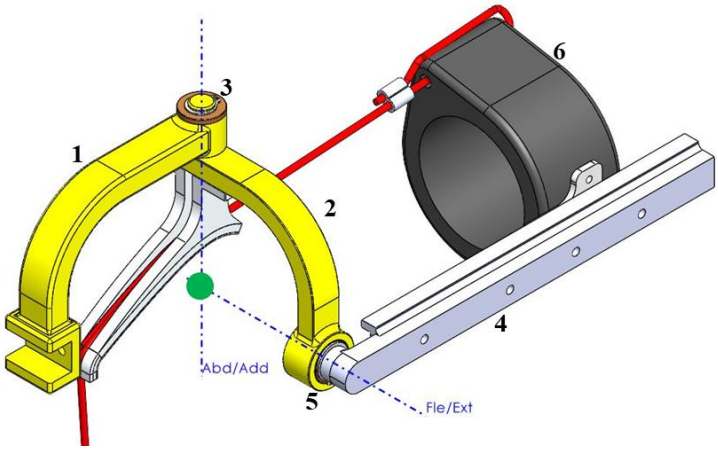

Figure 3.8 First design of the kinematic chain. The green dot is the rotation axes intersection which should be aligned with the SJC.

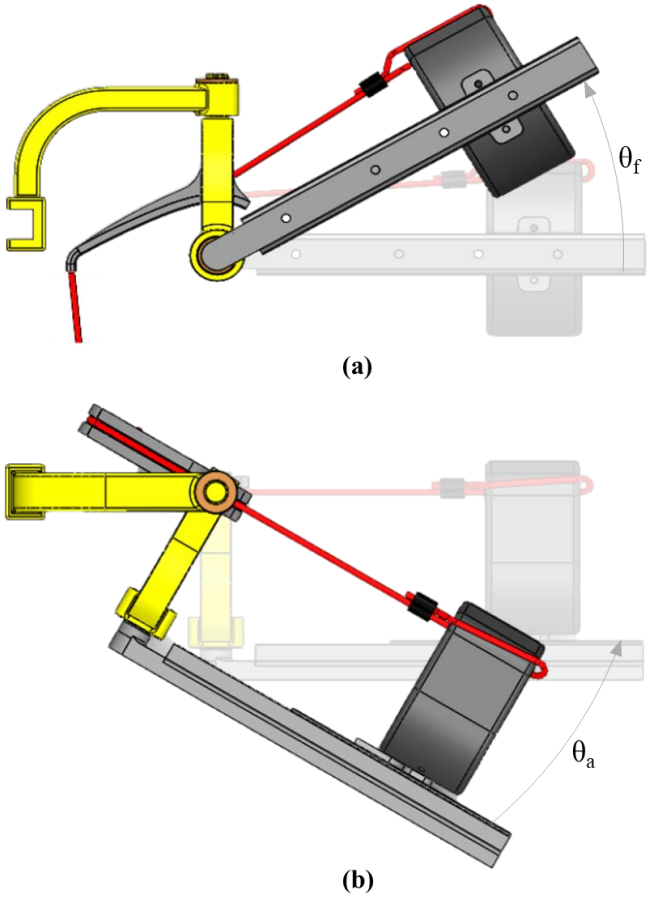

Figure 3.9 Examples of the kinematic chain movement. (a) Flexion; (b) Abduction.

Referring to Figure 3.8, the first arch (1) is rigidly fixed to the back frame, while the second one (2) can rotate with respect to the first one thanks to a bushing (3). This rotation performs the shoulder abduction/adduction DoF (Figure 3.9b). Then, a rigid link (4) running parallel to the arm is mounted into the movable arch through a second bushing (5), and the rotation of this link performs the flexion/extension DoF (Figure 3.9a). The bracelet (6) is bolted to the other end of the arm link. The two arcs must be made and mounted so that their axes of rotation are aligned with the shoulder joint rotation axes. Therefore, the intersection point of the two exoskeleton joint axes is the hypothetical SJC (Figure 3.8, green dot). The shoulder pad is attached to the movable arch to move with the arm during the shoulder abduction.

Although the above-described solution complies with the kinematic chain design features, a second solution, shown in Figure 3.10, is proposed to facilitate the construction and assembly of the exoskeleton shoulder joints.

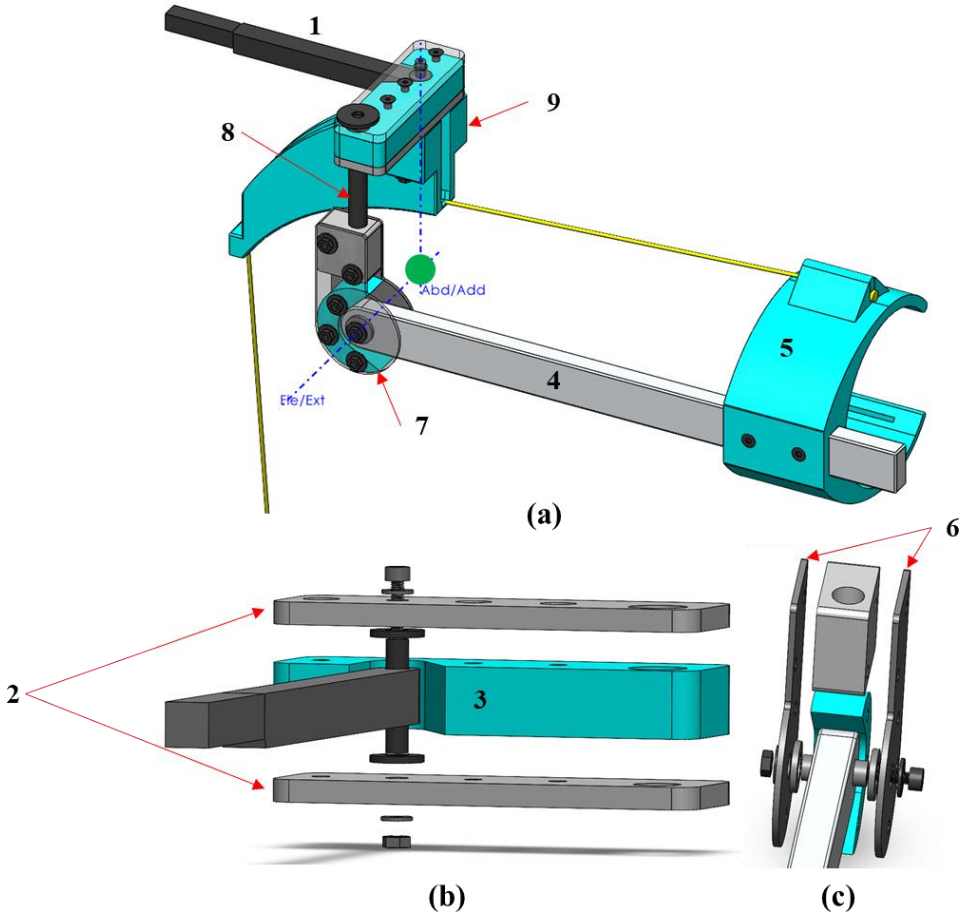

Figure 3.10 Final design of the kinematic chain (a) and details of the abduction (b) and flexion (c) joint. The green dot is the rotation axes intersection which should be aligned with the SJC.

The second solution consists of two hinges: a vertical axis hinge joint J_v (Figure 3.10b) to allow the abduction of the arm and a horizontal axis hinge joint J_h (Figure

3.10c) to permit shoulder flexion. The two rotational axes must intersect in the hypothetical SJC (Figure 3.10a, green dot). Both hinges are made of a fixed link, a pin, and a movable link that rotates around the pin. The latter, in turn, consists of a bushing, two washers, and a bolt that locks the axial displacement of the bushing.

Referring to Figure 3.10, J_v fixed link consists of a rigid bar (1) connected at the rear to the back frame of the exoskeleton. The front of the bar is instead drilled to accommodate the hinge pin. On the other hand, the movable link consists of two parallel plates (2) and the internal block (3) that acts both as a spacer for the plates and as a mechanical limit switch for the hinge, limiting the shoulder abduction to 30° (Figure 3.11b).

J_h has a similar structure to the previous one. Referring to Figure 3.10, the hinge's movable link is a rigid link (4) that runs parallel to the arm of the user. The front end of this link supports the bracelet (5) of the exoskeleton, while the rear end is drilled to accommodate the hinge pin inside. On the other hand, the fixed link is constituted of two parallel plates (6) and an internal block (7) that acts both as a spacer between the two plates and as a mechanical limit switch, allowing flexion of the shoulder between 70° and 135° (Figure 3.11a).

The two hinges are rigidly connected through an M10 bolt (8). Finally, the shoulder pad (9) is bolted to the movable link of the vertical axis hinge.

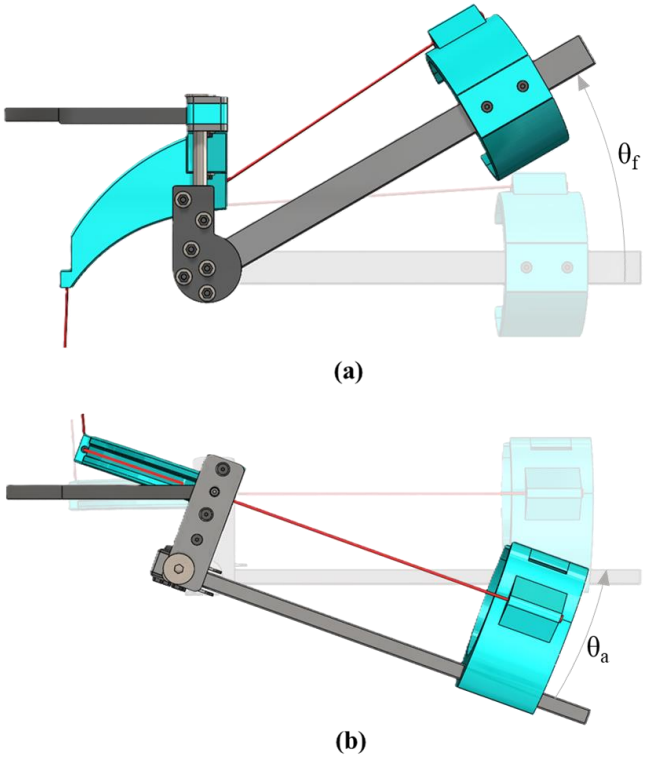

Figure 3.11 Examples of the kinematic chain movement. (a) Flexion. (b) Abduction.

Chapter 4

Assembly of the exoskeleton

This Chapter presents the exoskeleton architecture with particular attention to the contact points between the exoskeleton and the user and the interaction forces exchanged. The design of the exoskeleton in fact must verify the device's structural strength as well as prevent the human-exoskeleton interaction forces from exceeding the pain detection threshold (PDT) to ensure the user's safety.

The exoskeleton, shown in Figure 4.1, is made up of three main parts: the exoskeleton arms (exo-arm) (Figure 4.1b), the back frame (Figure 4.1c), and a commercial harness (FP14 – Portwest) (Figure 4.1d).

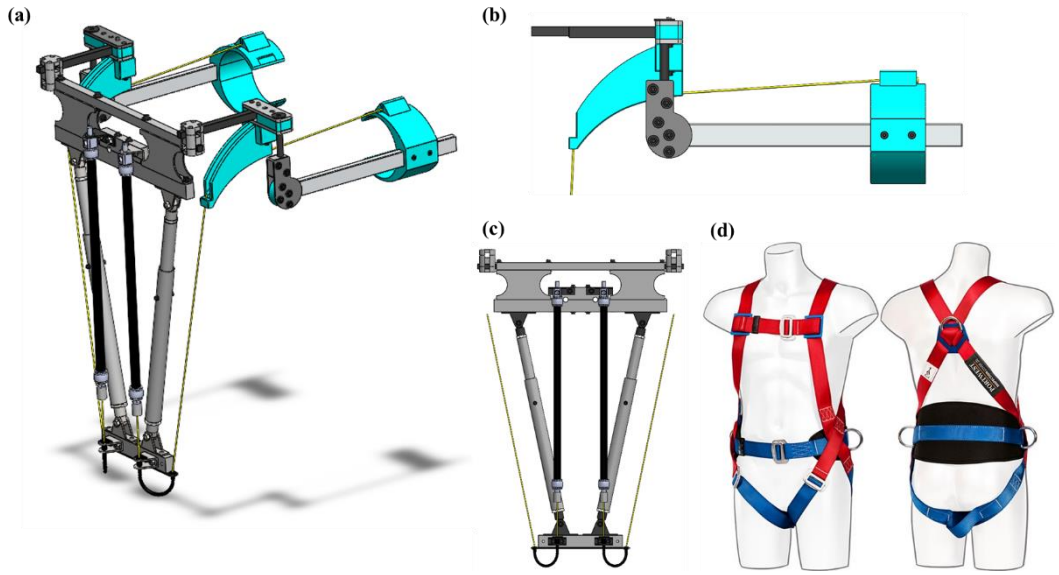

Figure 4.1 Exoskeleton structure (a) consisting of two exoskeleton arms (b), a back frame (c), and a commercial harness (d).

Each exo-arm supports the user's arm and includes the kinematic chain described in Section 3.2. The back frame is a rigid structure placed behind the user's back on which the reaction forces produced by the MKMs are discharged. Finally, the harness allows the user to wear the device easily and quickly.

The exoskeleton architecture will be described in detail in Section 4.1. Section 4.2 presents an analytical model for estimating the human-exoskeleton interaction forces. Finally, in Section 4.3, a stress analysis of the exoskeleton frame will be conducted.

The simulation results guarantee safety and facilitate the choice of the prototype constructive material and the sizing of the components.

4.1 Architecture of the exoskeleton

The final structure of the exoskeleton, shown in Figure 4.2, is assembled using both commercial and custom-made components.

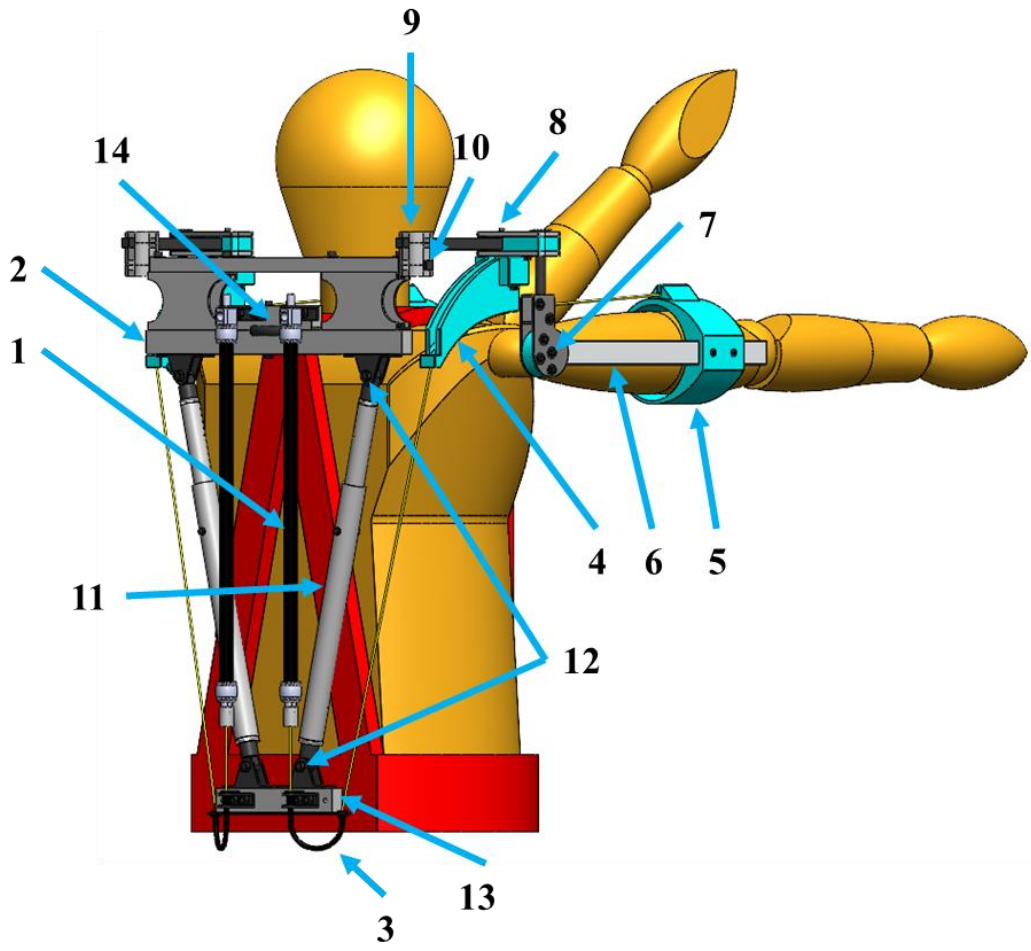

Figure 4.2 Exoskeleton structure.

Referring to Figure 4.2, two MKMs (DMSP-10-350N-RM-CM, FESTO, Germany) (1), one for each arm, are placed behind the back of the user. Their upper ends are fixed to the back-frame upper beam (2) by an L-shaped plate, while the lower ends are connected to a cable (Braided climax - 200daN, OCKERT, Germany). Custom aluminum eye rods fasten the cable to each MKM. The cable reverses its direction thanks to a high-density polyethylene-coated steel sheath (3) and two sheath clips. Then, it wraps around the shoulder pad (4) and finally joins the bracelet (5) that supports the user's upper arm. The bracelet is bolted to a strut (6) to prevent the high MKM traction forces from sliding the bracelet along the arm. Several positions are available along the strut to secure the bracelet to adapt the bracelet position to the upper arm's length of the user. The strut allows shoulder flexion articulating with the horizontal axis hinge J_h (7), which is connected to the vertical axis hinge J_v (8) that allows shoulder abduction. The bracelet, J_h, J_v, and the shoulder pad make up the exo-arm, which is attached to the back frame through a clamp (KPVV 10, RS Rose+Krieger, Germany) (9).

Adjustment elements are integrated into the back frame to adapt the position of the joint axes to the shoulder width and the shoulder-pelvic distance of the user.

Two custom square telescopic bars (10) adjust the position of the exo-arms in the mediolateral direction to align the J_v axis of rotation to the shoulder abduction axis. Due to this adjustable system, the cable must be connected to the lower end of MKM. The payload must be aligned to the axis of the pneumatic muscle to work correctly. Then, MKM should be placed exactly below the shoulder pad if the cable is attached to the muscle's upper end. However, when changing the mediolateral position of the exo-arm, the alignment fails unless the MKM is also moved. Therefore, this solution would increase system encumbrance and make the sizing of the exoskeleton more hard-working. Otherwise, by connecting the cable to the lower end of the MKM and then reversing its direction, the shoulder pad position can be changed without affecting the alignment between the load and the axis of the muscle. It is preferable to use a sheath instead of a pulley to reverse the direction of the cable to prevent the cable from rolling over during periods of non-use (supply pressure = 0 bar) and to reduce the device's overall weight.

Two custom vertical telescopic rods (11) instead allow for adjustment of the position of the shoulder pad and the J_h in the craniocaudal direction to have the alignment between the flexion-extension axis of the exoskeleton and the shoulder joint in the initial work position. Each telescopic rod is connected to the back frame through two round tube endcaps (NDL.T-20x1-1.5-M8 and NDL.T-25x1-1.5-2-M8, ELESA, Italy) and two fork supports articulated with flat eyes end fittings (12). The latter allow the rotation of the telescopic rods on the front plane and provide greater mobility to the user's trunk.

The adjustment elements that allow for adaptation to the physical characteristics of the subject of the longitudinal position of the bracelet and the

joints' axis of rotation are shown in detail in Figure 4.3. In addition, two ratchet tensioners, placed between the shoulder pad and the bracelet, adjust the cable length.

Finally, the back-frame is attached to a commercial harness to allow the wearing of the exoskeleton. The harness pelvic belt is screwed on the back-frame lower beam (13), while the thoracic ring of the harness is connected to the back-frame upper beam through a clamp (14) made ad hoc to follows the shape of the thoracic ring.

The contact points between the user and the exoskeleton are the bracelets, the pelvic belt, and the thoracic belt. The following section will estimate the magnitude of the pressures applied by the exoskeleton on the user at these contact points to verify that they are below the safety values identified in Section 1.2.1 (6 kPa for the trunk [37], 15 kPa for the pelvis [37], and 30 kPa for the upper arm [43]).

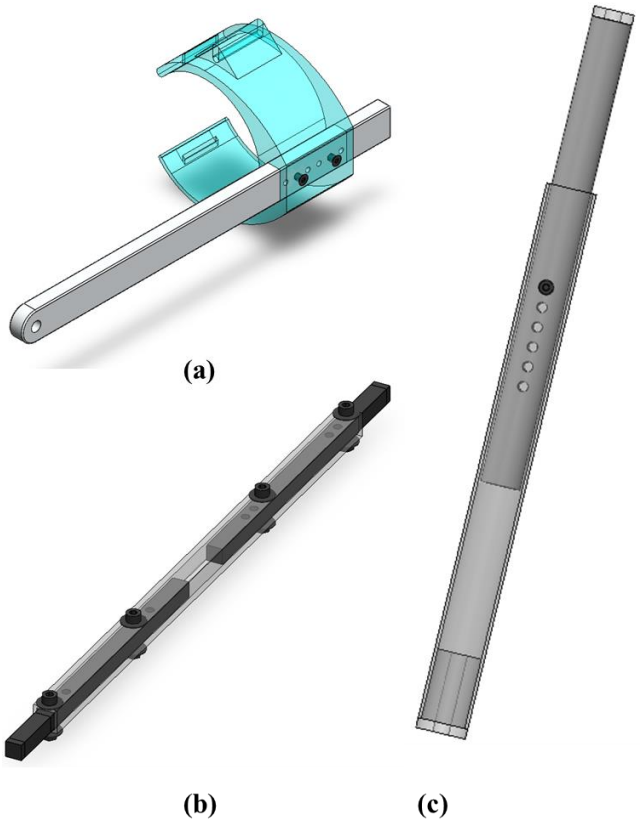

Figure 4.3 Adjustment elements. (a) Adjustment of the longitudinal position of the bracelet. (b) Adjustment of the shoulder width. (c) Adjustment of the shoulder-pelvis distance.

4.2 Human-exoskeleton interaction force

Figure 4.4 shows a graphical representation of the exoskeleton in the XYZ reference system, defined with the X-axis in the anteroposterior direction, the Y-axis in the cranio-caudal direction, and the Z-axis in the mediolateral direction. The

positive directions are forward, upward, and right side for the X-axis, Y-axis, and Z-axis, respectively. The connections between the back-frame and harness can be assimilated to kinematic constraints, so the human-exoskeleton interaction forces can be estimated by solving the static equilibrium of the system.

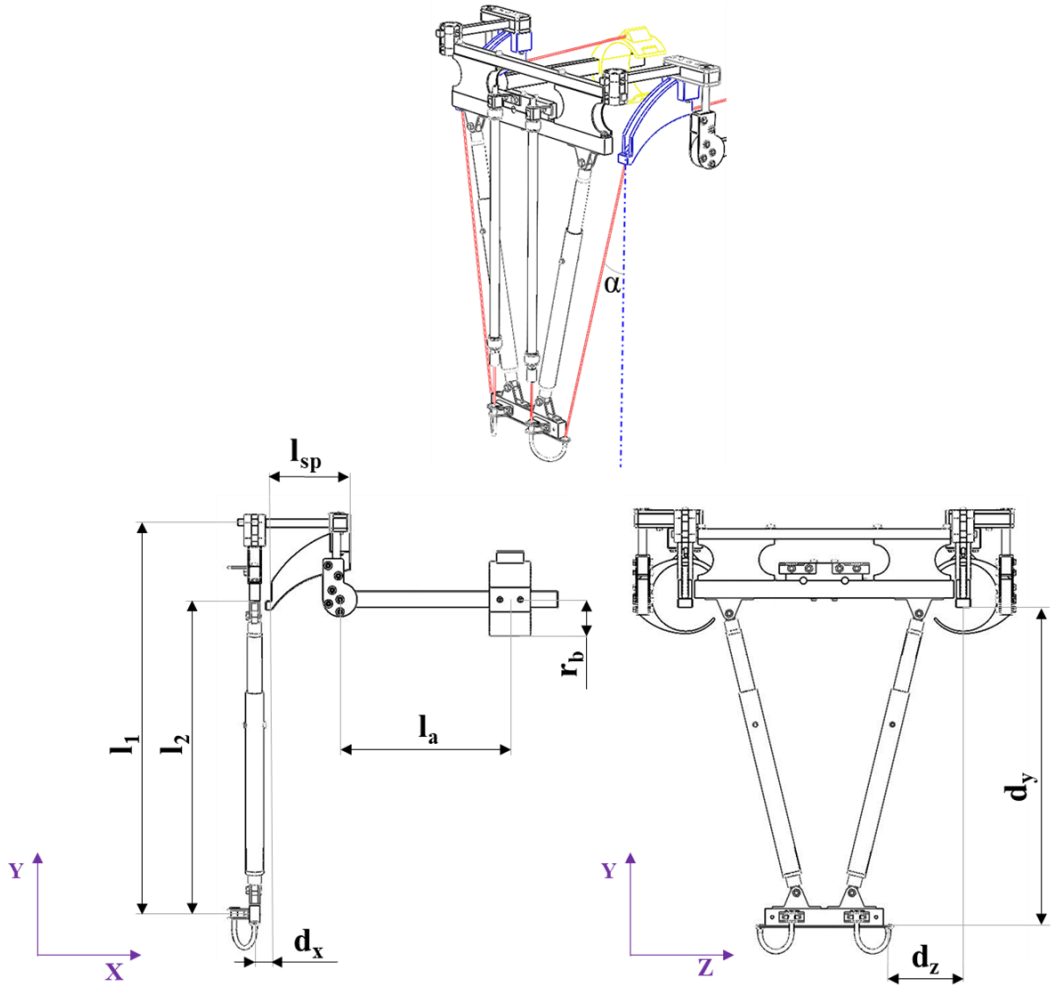

Figure 4.4 Graphical representation of the exoskeleton.

The following sections describe the analytical model employed to estimate the interaction forces and present the obtained results. The analyses considered only the static forces for different angles of flexion (θ_f) and abduction (θ_a) of the shoulder in the maximum load conditions. The exoskeleton weight and the friction are neglected.

4.2.1 Exo-arm

The exo-arm system is analyzed to evaluate the forces applied by the exoskeleton on the user's upper arm. Figure 4.5 shows a representation of the exo-arm. The connection with the back frame is modeled as a fixed support, while the

involved forces are the cable traction force and the bracelet-arm interaction force. The first is equal in modulus to the MKM tensile force (F_{MKM}) and is always directed along the cable direction. F_{MKM} is transmitted to the shoulder pad, in both the first (A) and last (Z) cable-shoulder pad contact point, and to the bracelets, in the bracelet-cable connection point. The F_{MKM} force applied on the bracelet and in point A lies on the arm flexion plane. On the other hand, the F_{MKM} force applied on point Z has components in X, Y, and Z directions that depend on the mutual distance between the shoulder pad and the sheath clip.

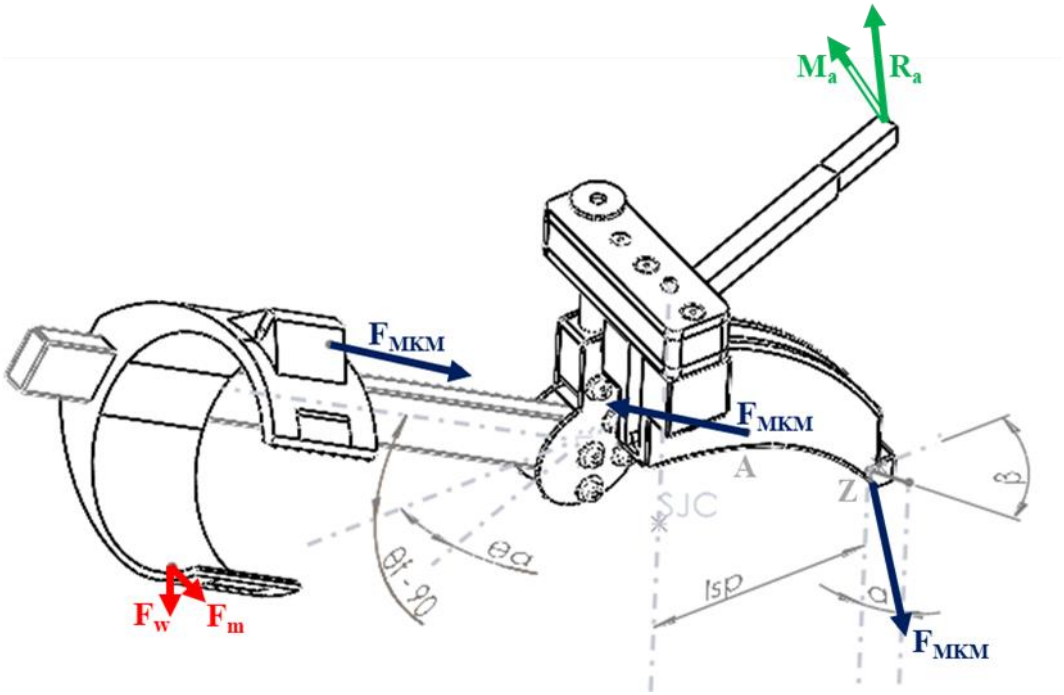

Figure 4.5 Representation of the exoskeleton arm. Ra and Ma are the fixed support constraining reactions; F_w is the user's arm gravitational load; F_m is the user's muscular force; F_{MKM} is the cable traction force. α is the angle between the cable and the Y-axis; β is the angle between the projection of the cable on the transverse plane and the X-axis; l_{sp} is the cam-length; θ_f and θ_a are the shoulder flexion and abduction angle, respectively.

The bracelet-arm interaction force (F_a) is partly due to the weight of the arm and any tool handled by the user (F_w) and partly to the user's muscular action (F_m).

Modeling the user's arm as a rigid link with mass concentrated in its center of mass, hinged in SJC and with roller support at the bracelet, F_w can be calculated as:

$$F_w = \frac{M_g}{l_a * \sin(\theta_f)} \tag{4.1}$$

In Equation 4.1, M_g is the gravitational torque at the shoulder, l_a is the distance between SJC and the bracelet (see Figure 4.4) and θ_f is the shoulder flexion angle.

On the other hand, F_m is the muscle action needed to keep the arm in the desired position. It depends on two factors. The first is the effort needed to compensate for the mismatch between the gravitational and exoskeleton support torque (F'_m) and thus maintain the desired flexion angle. The second is the effort needed to maintain the desired abduction angle (F''_m). Due to the distance in the middle-lateral direction between the shoulder pad Z-point and the sheath clip placed in the back-frame, the direction assumed by the F_{MKM} behind the user's back introduces an unwanted abducent moment around J_v that should be counteracted by activating the shoulder adductor muscles.

F'_m and F''_m can be evaluated as follow:

$$F'_m = \frac{F_{MKM} * r - F_w * l_a * \sin(\theta_f)}{l_a} \tag{4.2}$$

$$F''_m = \frac{F'_m * \cos(\theta_f) * \cos(\theta_a) * b_1 + F_{MKM} * \sin(\alpha) * \sin(\beta) * b_2 - F_{MKM} * \sin(\alpha) * \cos(\beta) * b_3}{(l_a * \sin(\theta_f) + r_b * \cos(\theta_f)) * \cos(\theta_a)} \tag{4.3}$$

$$b_1 = (l_a * \cos(\theta_f) + r_b * \sin(\theta_f)) * \sin(\theta_a) \tag{4.4}$$

$$b_2 = l_{sp} * \sin(\theta_a) \tag{4.5}$$

$$b_3 = l_{sp} * \cos(\theta_a) \tag{4.6}$$

$$\alpha = \operatorname{acos}\left(\frac{d_y}{\sqrt{d_x^2 + d_y^2 + d_z^2}}\right) \tag{4.7}$$

$$\beta = \operatorname{acos}\left(\frac{d_x}{d_z}\right) \tag{4.8}$$

In Equations (4.2 – 4.8), r is the distance between the horizontal hinge axis (J_h) and F_{MKM} applied on the bracelet; l_a is the distance between the bracelet and J_h; b_1 is the lever arm of the X-component of F'_m; b_2 is the lever arm of the X-component of F_{MKM} applied in the shoulder pad Z point; b_3 is the lever arm Y-component of F_{MKM} applied in the shoulder pad Z-point; r_b is the bracelet inner radius; l_{sp} is the shoulder pad length; α is the angle between the cable and Y-axis calculated on the plane that contains both the cable and the Y-axis; β is the angle between the

projection of F_{MKM} on the transverse plane and X-axis; d_x, d_y, and d_z are the distance between the shoulder pad and sheath clip (see Figure 4.4).

At this point, the X (F_{ax}), Y (F_{ay}), and Z (F_{az}) components of the arm-bracelet interaction force can be obtained as:

$$F_{a_x} = F'_m * \cos(\theta_f) * \cos(\theta_a) \quad (4.9)$$

$$F_{a_y} = F'_m * \sin(\theta_f) + F_w \quad (4.10)$$

$$F_{a_z} = F''_m \quad (4.11)$$

Finally, the reaction force (R_{ax}, R_{ay}, R_{az}) between the exo-arm and the back frame can be calculated (Equations 4.12 – 4.14).

$$R_{a_x} = -F_{a_x} + F_{MKM} * \sin(\alpha) * \sin(\beta) \quad (4.12)$$

$$R_{a_y} = F_{a_y} + F_{MKM} * \cos(\alpha) \quad (4.13)$$

$$R_{a_z} = F_{a_z} + F_{MKM} * \sin(\alpha) * \cos(\beta) \quad (4.14)$$

4.2.2 Back Frame

The analysis of the forces applied on the back frame, shown in Figure 4.6, allows the evaluation of the exoskeleton-trunk interaction forces.

The connections of the back frame with the pelvic belt allow rotations around the support point and displacements in the Z-direction, while the connection with the thoracic ring of the harness allows rotations around the support point and displacements in the Y-direction. The involved forces are the MKM traction forces (F_{MKM}), the cable tension, and the reaction forces of the exo-arms (R_a).

F_{MKM} is directed downward and acts on the L-shaped plates supporting the two MKMs.

The cable tension is distributed on the inner surface of the sheaths and tends to flatten it. However, the sheaths maintain their shape thanks to the sheath clips. Therefore, for the sake of simplicity, the cable tension can be considered concentrated, applied on the sheet clips' fixing point, equal to F_{MKM}, and directed along the cable direction.

Finally, the exo-arms' reaction forces are exerted on the exo-arm-back frame connection point.

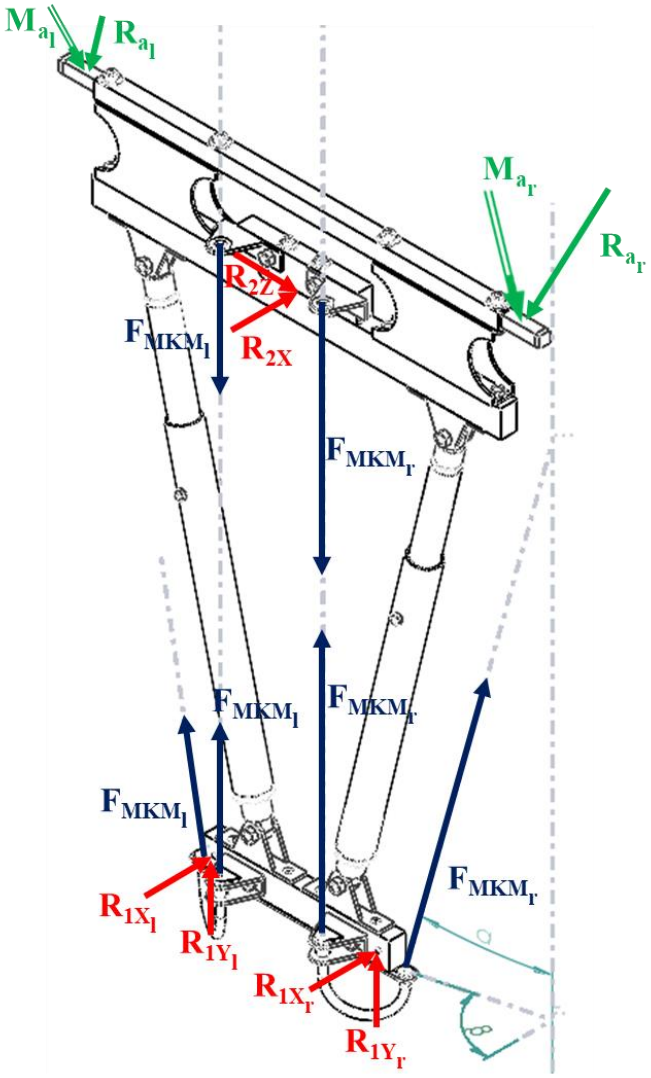

Figure 4.6 Representation of the back frame. Ra and Ma are the fixed support constraining reactions; F_{MKM} is the MKM traction force; R_{1X} and R_{1Y} are the X and Y components of the reaction force exchanged between the back-frame and the pelvic belt; R_{2X} and R_{2Z} are the X and Z components of the reaction force exchanged between the back-frame and the thoracic belt; α is the angle between F_{MKM} and the Y-axis; β is the angle between the projection of F_{MKM} on the transverse plane and the X-axis. The subscripts r and l refer to the right and left sides.

To solve the static equilibrium of the back frame, the Equation (4.15 – 4.18) can be wrote. The reaction force applied to the pelvic belt (R_1) and the thorax belt (R_2) can then be used to estimate the human-exoskeleton interaction forces at the level of the thorax (F_t, Equation 4.19) and pelvis (F_p, Equation 4.20).

$$R_{1x} = R_{1x_r} + R_{1x_l} = R_{ax_r} + R_{ax_l} - R_{2x} - \left(F_{MKM_r} + F_{MKM_l}\right) * \sin(\alpha) * \cos(\beta) \quad (4.15)$$

$$R_{2x} = \frac{\left(R_{ax_r} + R_{ax_l}\right) * L_1 - M_{ax_r} - Max_l}{L_2} \quad (4.16)$$

$$R_{1y} = R_{1y_r} + R_{1y_l} = R_{ay_r} + R_{ay_l} - (F_{MKM_r} + F_{MKM_l}) * \cos(\alpha) \quad (4.17)$$

$$R_{2z} = R_{az_r} - R_{az_l} + \left(F_{MKM_l} - F_{MKM_r}\right) * \sin(\alpha) * \sin(\beta) \quad (4.18)$$

$$F_t = R_{2x} \quad (4.19)$$

$$F_p = \sqrt{R_{1x}^2 + R_{1y}^2 + R_{2z}^2} \quad (4.20)$$

4.2.3 Contact pressure estimation

The analytical model presented in Sections 4.2.1 and 4.2.2 has been implemented in MATLAB. The simulations are performed considering an average height man (70 kg, 1.7 m) in the heaviest working condition (extended elbows and a 2 kg tool in the right hand). The gravitational torque is calculated based on the anthropometric parameters reported in Table 1.3. On the other hand, the assistive torque is obtained assuming the supply pressure and the contraction ratio identified in Sections 2.5 and 2.7 (k_i = 2%; p = 4.3 bar, and p = 7.7 bar for the left and right arm, respectively). Finally, the alignment between ExoJC and SJC is assumed for a shoulder flexion angle equal to 90°.

The calculated human-exoskeleton interaction forces (F_a, F_t, F_p) have been used to investigate the contact pressures applied on the user's arms, chest, and pelvis to ensure that the pain detection thresholds (PDT) reported in Section 1.2.1 are not exceeded. A contact surface of half the inner surface of the bracelet (79 cm^2, Figure 4.7a) has been assumed to estimate the pressure on the user's arms. The arm contact pressure trends are shown in Figure 4.8, as the angle of flexion and abduction varies. It should be noted that even when both the gravitational and the assistive torque are maximum (Figure 4.8b), the PDT of 30 kPa is not exceeded throughout the exoskeleton working range.

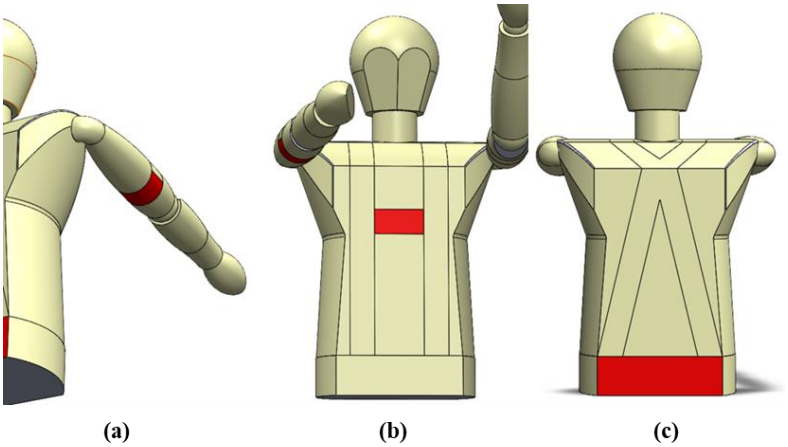

Figure 4.7 A sketch of the user highlighting the contact surfaces between the exoskeleton and the upper arm (a), the thorax (b), and the pelvis (c) of the user.

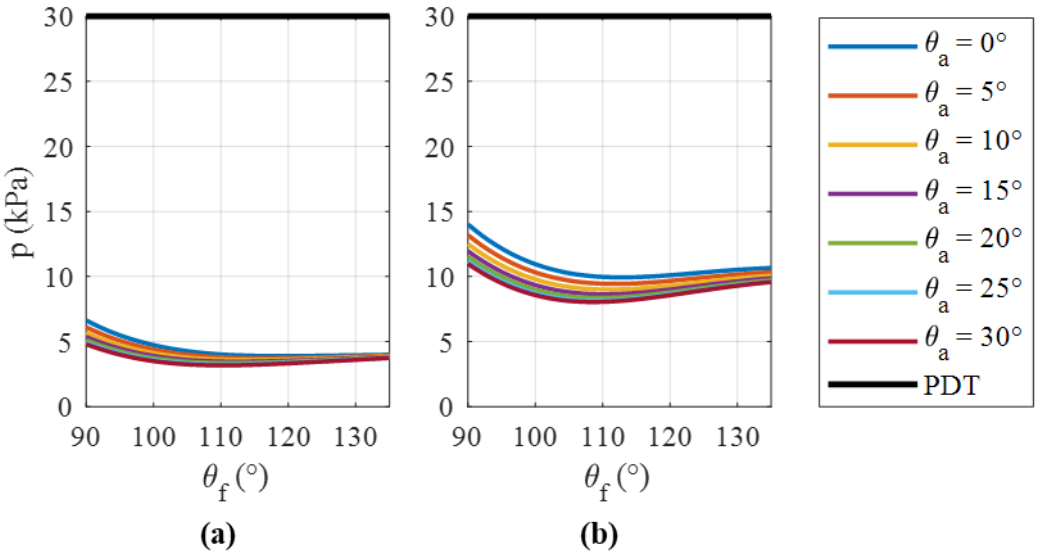

Figure 4 8 The pressure exerted on the left (a) and right (b) upper arm of the user to vary both flexion (θ_f) and abduction (θ_a) of the shoulder. The black line represents the pain detection threshold (PDT).

The pressures on the chest and pelvis have been estimated assuming a contact surface equal to the size of the thoracic belt (102 cm^2, Figure 4.7b) and pelvic belt (540 cm^2, Figure 4.7c). The estimated contact pressures are shown in Figure 4.9 and do not exceed the selected thresholds (6 kPa for the chest and 15 kPa for the pelvis).

The results are promising in terms of safety. The low estimated contact pressures minimize the risk of damage to the user's soft tissues even for long periods of exoskeleton use.

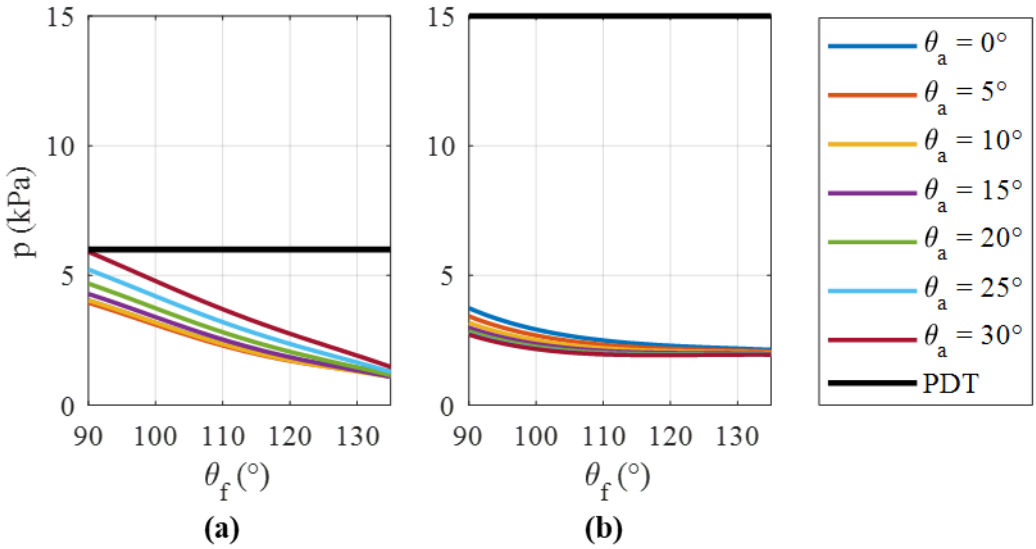

Figure 4.9 The pressure exerted on the chest (a) and pelvis (b) of the user to vary both flexion (θ_f) and abduction (θ_a) of the shoulder. The black line represents the pain detection threshold (PDT).

4.3 FEM structural analysis

Finite Element Analysis (FEM) has been used to run static structural analysis for the study of stresses in the exoskeleton structure.

SolidWorks is used to build the exoskeleton model and then its Simulation tool is used to perform the FEM analysis. The analysis aims to assist in choosing materials and sizing the various exoskeleton parts in order to avoid the structural failure of the exoskeleton components. To this end, the most demanding working conditions are considered. Therefore, the same boundary conditions established in Section 4.2.3 (1.7 m; 70 kg; elbows extended; tool of 2 kg in the right hand; ki = 2%; supply pressure equal to 4.3 bar for the left arm and 7.7 bar for the right arm) are employed in FEM simulations. In addition, θ_f and θ_a are set equal to 90° and 0°, respectively.

Low-cost and easy to find, and work materials are assessed to develop the prototype. As a result, stainless steel (DIN 1.4301 X5CrNi18-10) and aluminum alloy (EN AW - 6060-t6) are selected as constructive materials based on the mechanical stress magnitude to which the component is subjected. In addition, to simplify the manufacturing, peculiar-shaped components (e.g., the shoulder pad) could be made of polylactic acid (PLA) through fusion deposition modeling techniques.

Stainless steel and aluminum alloys can be modeled as isotropic materials, and their mechanical characteristics are listed in Table 4.1. On the other hand, the PLA mechanical properties depend on different printing parameters, first of all, the printing direction. Generally, Young's modulus and yield strength are higher along the printing direction and decreased by about 50% in the other two directions due

to the delamination of weak filament bonds [111]. It should be noted that molten PLA filament flattens during extrusion, facilitating the air gap formation in the printing plane. As a result, the gravity direction and the other transverse direction also have different mechanical properties. Therefore, an orthotropic material model should be implemented [112]. However, the effect of gravity deposition is rarely considered, and many previous studies [113–119] employ the transverse isotropic model, according to which the cross-section along the fiber direction is an isotropic surface. This work also assumed this hypothesis. The PLA mechanical characteristics have been extrapolated from the literature and are listed in Table 4.1.

Finally, FEM simulations are performed separately for the two subassemblies: exo-arm and back-frame. The results are presented and discussed in Sections 4.3.1 and 4.3.2, respectively.

Table 4.1 Young's modulus (E), Poisson's ratio (ν), shear modulus (G), yield strength (S_y) and ultimate tensile strength (S_{ut}) of the identified materials.

Material	E (MPa)	ν	G (MPa)	S_y (MPa)	S_{ut} (MPa)
DIN 1.4301 (X5CrNi18-10)	200000	0.28	79000	400	600
EN AW - 6060-t6	66000	0.33	25000	230	230
PLA (printing direction)	2904.2	0.292	723.34	56	56
PLA (other directions)	2597.5	0.299	1010	35	35

4.3.1 Exo-arm structural analysis

The constraints and loads to which the exo-arm is subjected are shown in Figure 4.10 and detailed in the following.

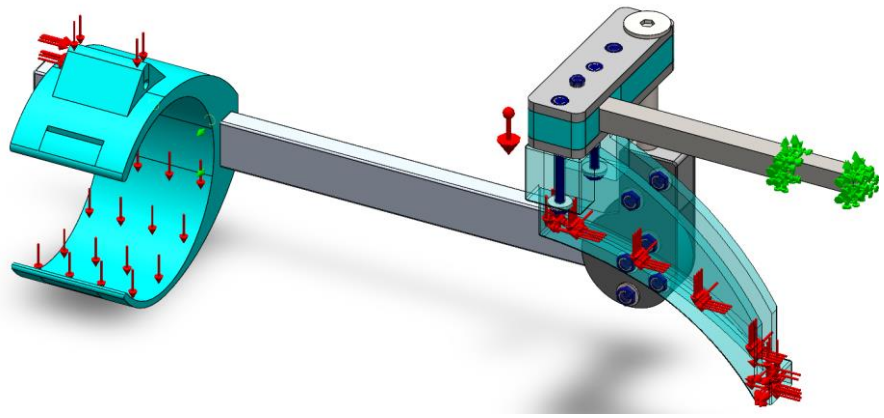

Figure 4.10 CAD model of the exo-arm with constraints and loads highlighted by green and red arrows, respectively.

Since the exo-arm is fixed to the back frame through the clamp, the interface between the exo-arm and the clamp is modeled as a fixed geometry constraint. In addition, the bracelet translation in the Z-direction is constrained to simulate the force applied by the subject on the bracelet to maintain the desired abduction angle.

Regarding the loads:

- The interaction force between the arm of the user and the bracelets is due to both the arm weight and the user's muscular action. The latter compensates for the mismatch between the assistive and gravitational torque and maintains a shoulder flexion angle of 90°. In the simulated condition, the bracelet-arm interaction force is directed along the Y-axis, and its magnitude is obtained by solving equation 4.10. It is equal to -98.55 N for the right arm and -46.67 N for the left arm.
- The cable traction force is exerted both on the bracelet and shoulder pad.
  On the bracelet, it is applied near the cable connection point and directed along the cable. Therefore, it has both X and Y components. The X component is -546.55 N for the right arm and -258.83 N for the left arm, while the respective Y components are 32.62 N and 15.45 N.
  The shoulder pad is also subjected to the cable tension because the cable slides without crawling along the shoulder pad. In the FEM model, the resultant force of the tensions applied by the cable in point A and point Z is distributed over the shoulder pad surface. The force components X, Y, and Z are 522.1 N, -503.46 N, and - 108.69 N for the right arm and 247.25 N, -238.42 N and 51.47 N for the left arm. The friction between the cable and the shoulder pad is neglected.
- The gravitational load due to the weight of the components is applied to the exo-arm center of gravity.
- A preload has been defined for each of the 13 bolted joints of the exo-arm: two M4 bolts between the bracelet and the strut (1.25 Nm); six M4 bolts in the horizontal axis hinge (2.5 Nm); three M4 bolts and one M3 bolt in the vertical axis hinge (1.88 Nm and 1.09 Nm, respectively); one M10 bolt to join each other the vertical and horizontal axis hinges (2.5 Nm). All bolts are class 8.8, and the tightening torque is less than or equal to 80% of the elastic bolt limit for each one.

The magnitude and the direction of the load are obtained from the analytical model described in Section 4.2.

Finally, global contact interaction is applied to prevent interference but allow backlash between components.

The model has been discretized through a tetrahedral curvature-based mesh with a minimum element size of 0.9 mm and a maximum size of 17 mm.

In the following, only the simulation results of the right exo-arm are shown since it works in more demanding conditions. The Von Mises resistance criterion has been adopted for isotropic materials, ensuring that the equivalent stress is lower than the material yield stress. On the other hand, for PLA components, the criterion of the maximum normal stress is adopted, and it is verified that its value along each direction is lower than the corresponding ultimate strength.

The most stressed component is the M10 bolt that connects the two hinges (Figure 4.11). However, the maximum Von Mises stress is equal to 585 MPa hence it is less than the bolt yield stress (640 MPa).

In addition to the bolt, the most stressed parts are the plates that constitute the fixed element of J_h and the fixed element of J_v (Figure 4.12). These components must be made of stainless steel to withstand the loads (355 MPa).

On the other hand, Figure 4.13 shows the exo-arm components moderately stressed (191 MPa). All of them (the two parallel plates that form the J_v moveable link, the J_h moveable link, and the spacer of the J_h rigid link) are constructed in aluminum alloy to lighten the structure as much as possible.

Finally, the remaining parts are made of PLA (Figure 4.14 – 4.15).

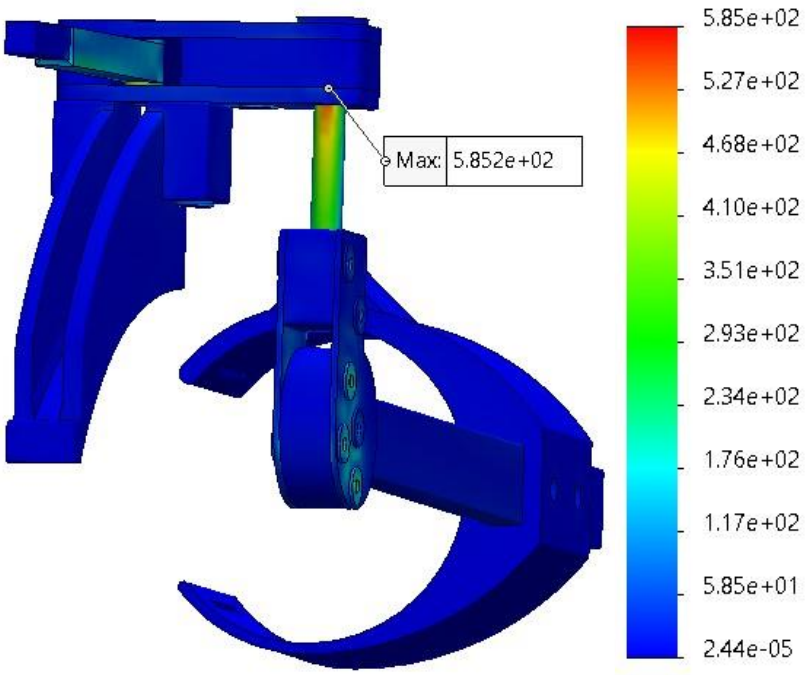

Figure 4.11 Von Mises stresses expressed in MPa in the whole right exo-arm.

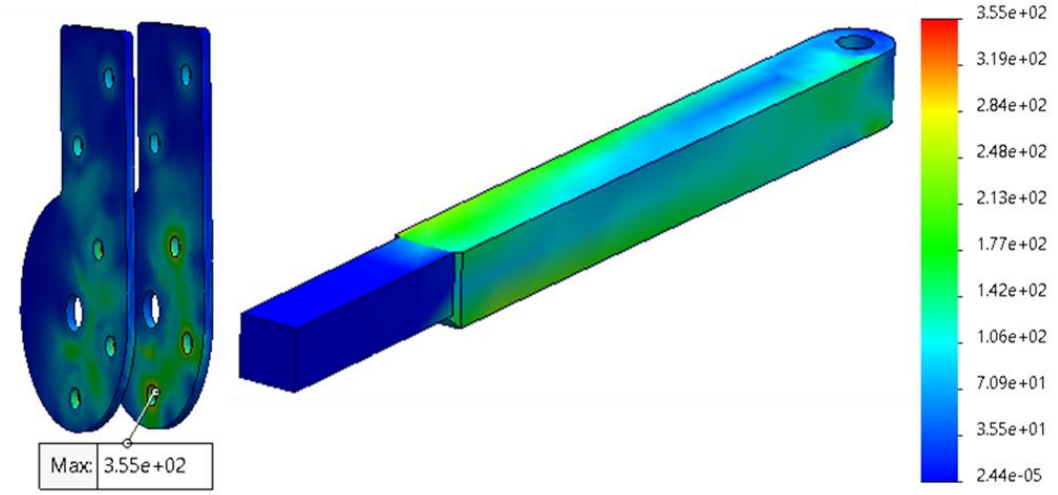

Figure 4.12 Von Mises stress expressed in MPa in the stainless steel component.

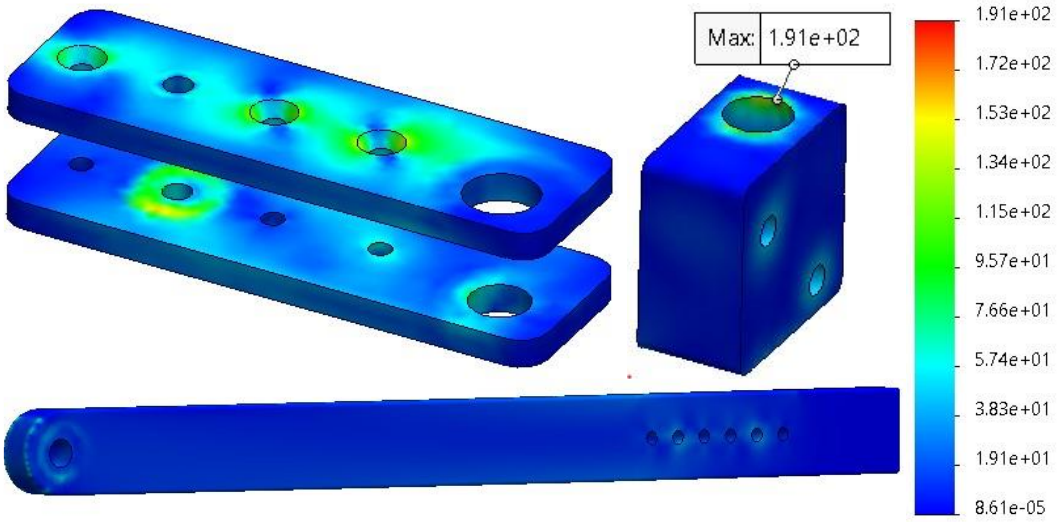

Figure 4.13 Von Mises stress expressed in MPa in the aluminum alloy component.

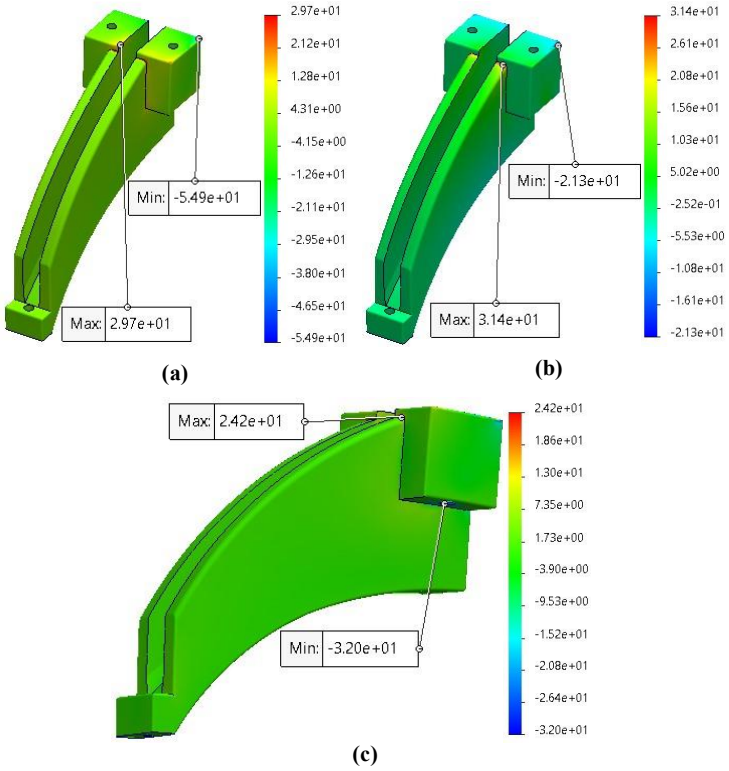

Figure 4.14 Shoulder pad maximum normal stress in the fiber (a) and transversal direction (b - c). Stresses are in MPa.

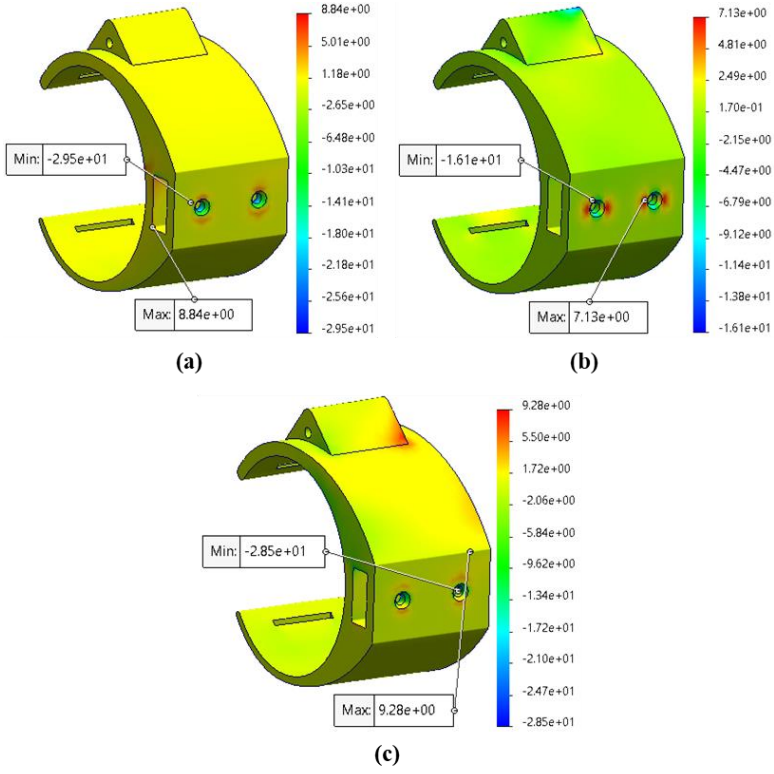

Figure 4.15 Bracelet maximum normal stress in the fiber (a) and transversal direction (b-c). Stresses are in MPa.

Due to the loads, the axis of the horizontal hinge is lowered by about 2 mm and moves back by about 5 mm (Figure 4.16). It should be taken into account wearing the exoskeleton. Therefore, an initial offset must be planned to prevent a misalignment between the J_h and SJC during the working task. The bracelet also lowers, causing the flexion angle to be reduced by about 2°. The user must likely apply a less muscular action than that estimated with Equation 4.2 to maintain the position desired. This discordance may be due to two different factors: the presence of the exo-arm weight in FEM simulations and the application of distributed and non-concentrated loads on the bracelet and shoulder pad.

Finally, Table 4.2 shows the reaction forces between the exo-arm and the clamp returned by FEM analysis. These results will be used for the structural analysis of the back frame (Section 4.3.2).

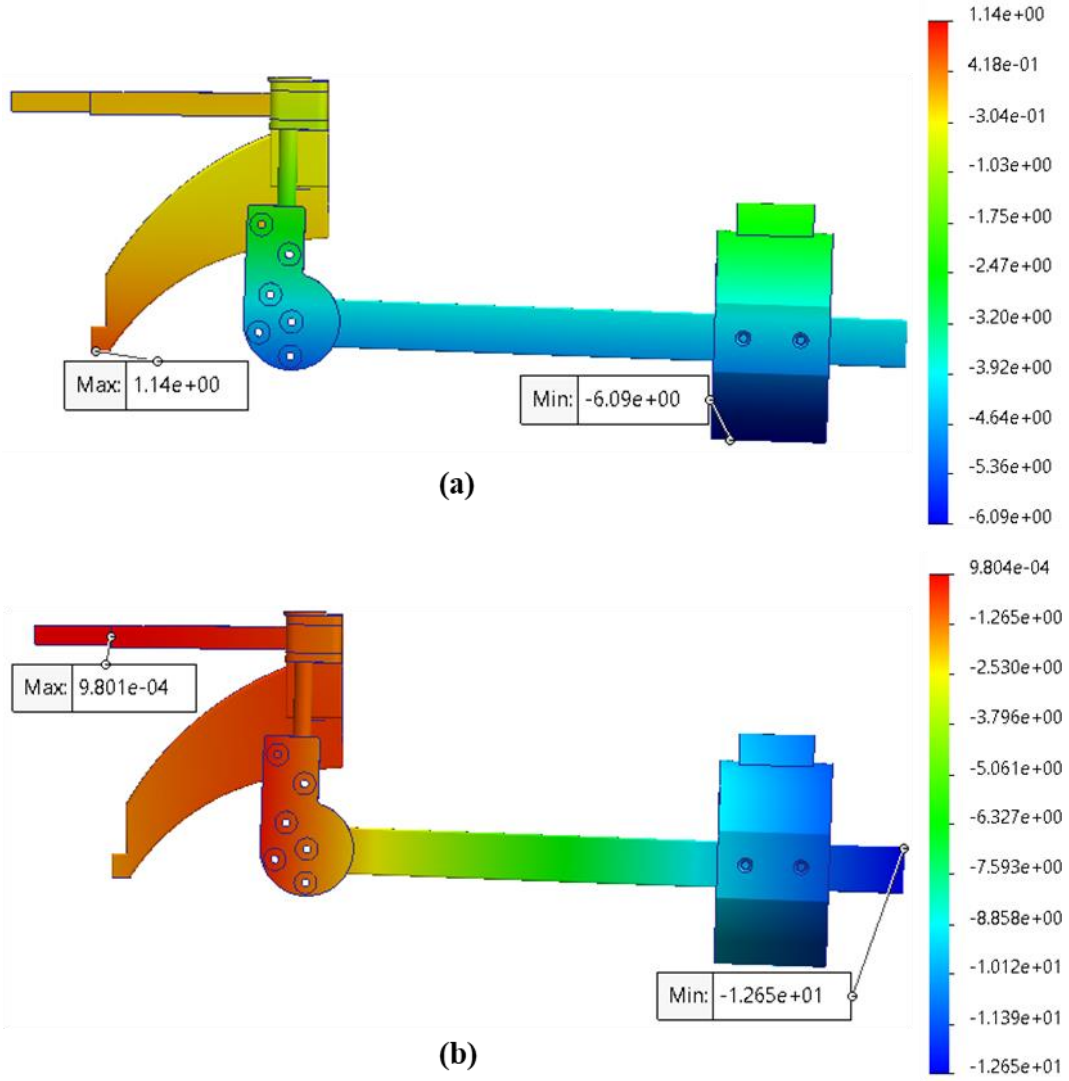

Figure 4.16 Displacement in X (a) and Y (b) direction. Data are expressed in mm.

Table 4.2 Reaction forces between exo-arms and back frame.

	Left Arm	Right Arm
R_x (N)	15.6	24.1
R_y (N)	314.6	644.1
R_z (N)	62.8	137.8
M_x (Nm)	6.1	-13.0
M_y (Nm)	-3.3	6.8
M_z(Nm)	22.3	44.9

4.3.2 Back frame structural analysis

Figure 4.17 shows the constraints and the loads acting on the back frame. The model is simplified by removing MKMs and sheaths and applying forces directly to the structure. The load magnitude and direction, detailed in the following, are obtained from the analytical model described in Section 4.2.

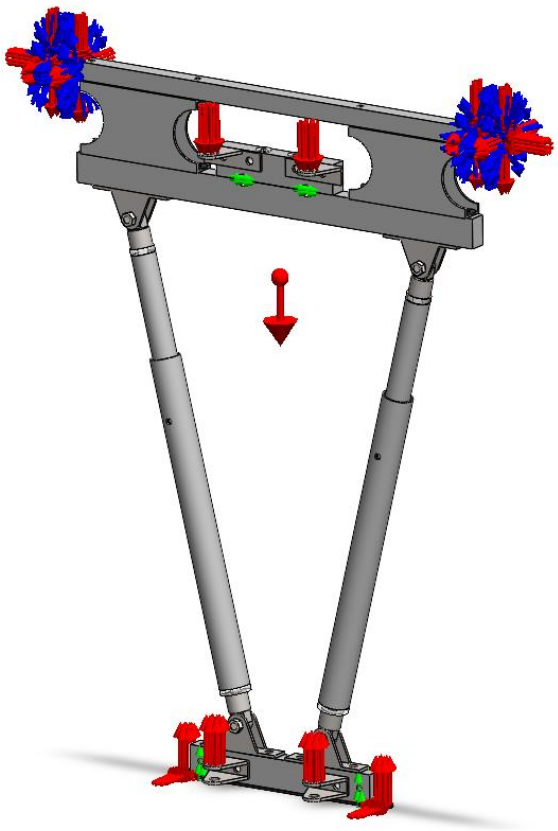

Figure 4.17 CAD model of the back frame. The green arrows represent the model constraints, while red and blue arrows represent forces and torques acting on the structure.

The harness's thoracic ring prevents translation in the X and Z directions, while the pelvic belt hinders translation in the X and Y directions.

Regarding the loads:

- The reaction forces listed in Table 4.2 act on the two square telescopic bars.
- The MKMs exert a traction force on the L-plates. The two forces are directed along Y and equal to -547.5 N for the right side and -259.3 N for the left side.
- The cable traction forces are applied at the sheath clips and are directed along the cable. They are opposite to the MKM traction forces in the medial sheath clips (before the cable reversal). In the two lateral sheath clips (after the cable reversal), instead, their components X, Y, and Z are equal to 24.4 N, 536 N, and 108.7 N for the right side and 11.6 N, 253.9 N, and -51.5 N for the left side.
- The gravitational load due to the weight of the components is applied to the back frame center of gravity.
- A preload has been defined for each of the 26 bolted joints of the back frame. All bolts are class 8.8, and the tightening torque is less than or equal to 80% of the elastic bolt limit for each one.

Finally, global contact interaction is applied to prevent interference but allow backlash between components.

The model has been discretized through a tetrahedral curvature-based mesh with a minimum element size of 0.62 mm and a maximum size of 12.4 mm.

The Von Mises resistance criterion has been adopted to evaluate the strength of the structure.

The most solicited parts are the L-plate, the sheath clips, and the square telescopic bar on the right side. All these components, as well as their left-side counterparts and the four hinges that allow the vertical telescopic bars to rotate in the frontal plane, are made of stainless steel 1.4301, whose yield strength is higher than the estimated maximum Von Mises stress (393 MPa, Figure 4.18).

As in the case of the exo-arm, all other components are made of aluminum to lighten the structure as much as possible. The maximum Von Mises stress is equal to 195 MPa (Figure 4.19), so the Von Mises criterion is respected.

Finally, Figure 4.20 shows the back frame displacements with a deformation scale equal to 20. Due to the loads, the upper part of the back frame bends forward, and the telescopic square bar twists clockwise while the MKM support and the sheath clip approach each other. However, the proper functioning of the exoskeleton should not be altered as the maximum displacement is less than one millimeter (Figure 4.21).

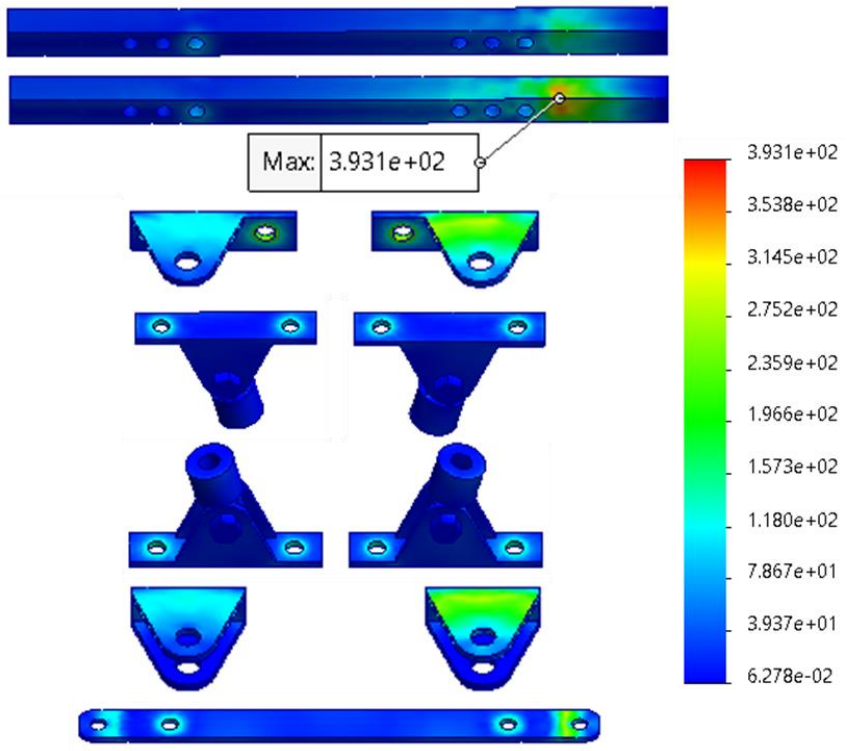

Figure 4.18 Von Mises stress expressed in MPa in the stainless steel component of the back frame.

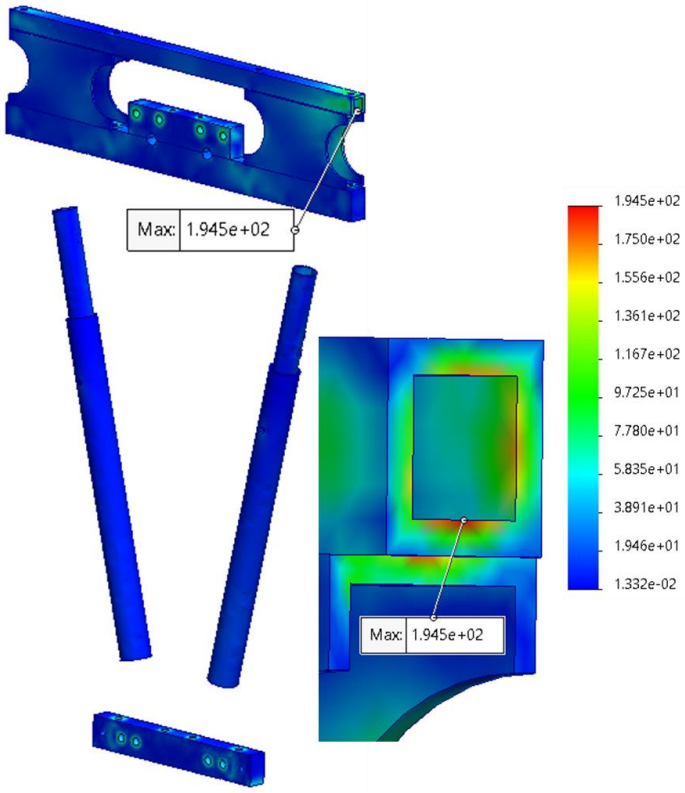

Figure 4.19 Von Mises stress expressed in MPa in the aluminum alloy component of the back frame.

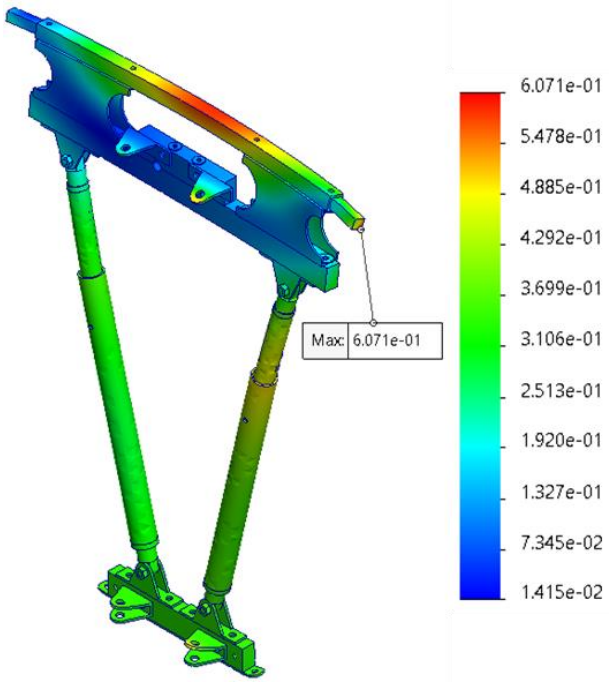

Figure 4.20 Displacement magnitude of the back frame. Data are expressed in mm.

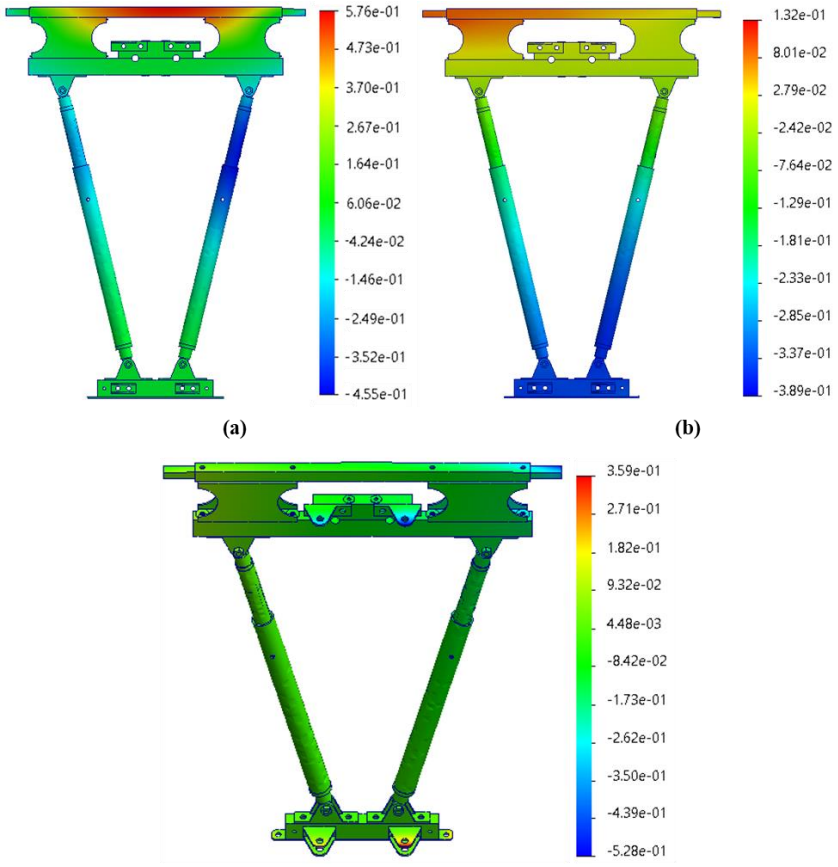

Figure 4.21 Displacement in X (a), Z (b), and Y (c) direction. Data are expressed in mm.

4.4 Exoskeleton size

The results of both exo-arm and back frame FEM analysis imply that the designed exoskeleton provides stable support. Therefore, by assuming the materials suggested by the FEM analysis results and the commercial components identified (i.e., harness, MKMs, clamps, etc…), the prototype shown in Figure 4.22 is developed.

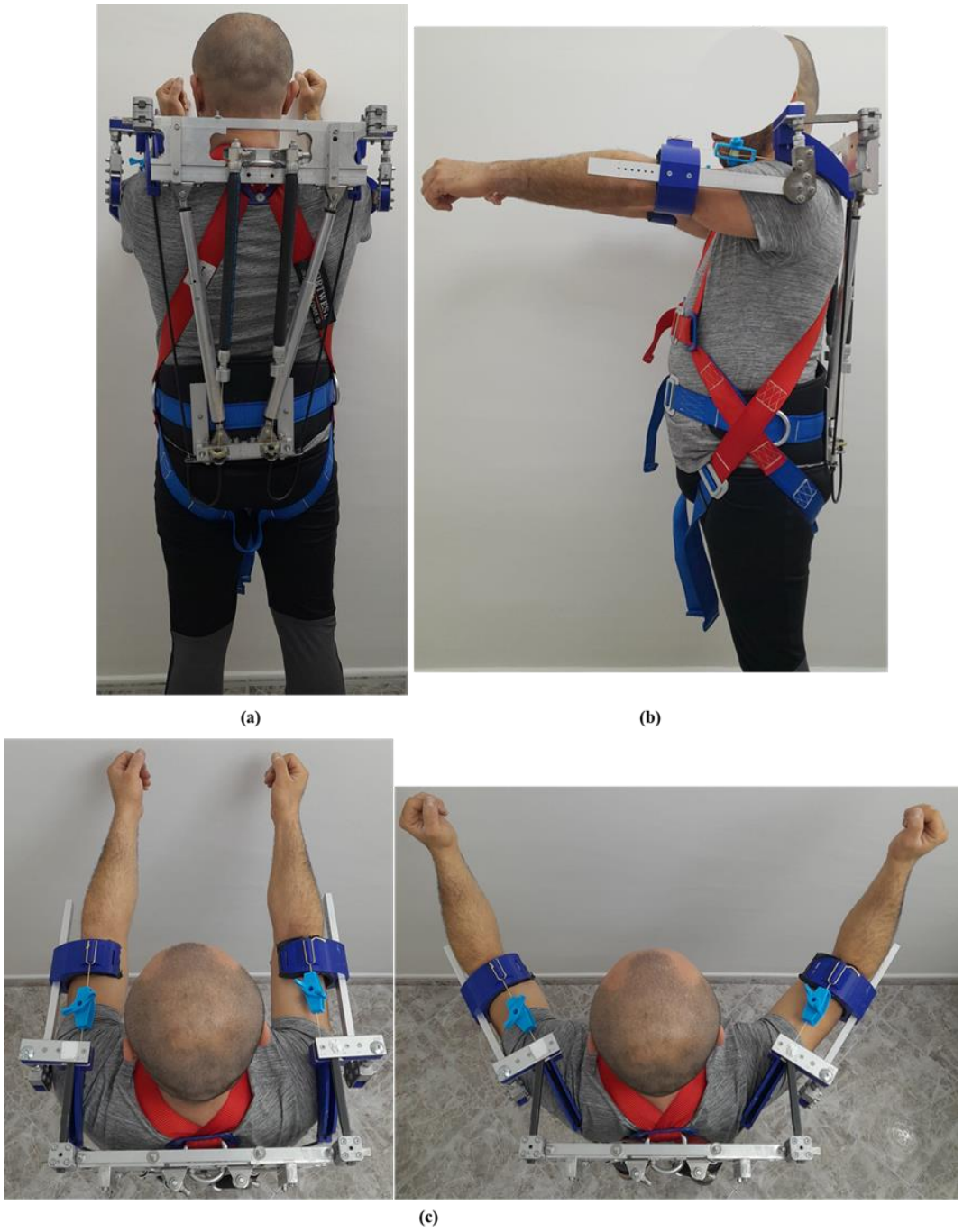

Figure 4.22 Rear (a), left side (b) and upper (c) view of the prototype.

The prototype is suitable for users with a height between 160 cm and 175 cm. The distance between the bracelet and J_h can be varied from 180 mm to 260 mm, the shoulder width from 370 mm to 410 mm, and the shoulder-pelvis distance between 460 mm and 500 mm. The width of the exoskeleton at the pelvis level is fixed and is equal to 200 mm. To improve user comfort, the bracelets' inner surfaces and the shoulder pads' outer surfaces have been covered with a polyamide coating (ComforTex soft, Ottobock, Duderstadt, Germany). The total weight of the exoskeleton is about 5.5 kg.

Although the exoskeleton size is in line with those of exoskeletons currently on the market, its weight is about twice that. However, it must be considered that is a prototype. In the future, the device's weight should be reduced by using lightweight and high-strength materials, such as carbon fiber.

Chapter 5

Test-bench analyses

The torque generator and the kinematic chain functionality are evaluated through preliminary static tests performed on a test bench. The tests aimed to check the MKM behavior during the exo-arm flexion.

The test bench used is outlined in Figure 5.1.

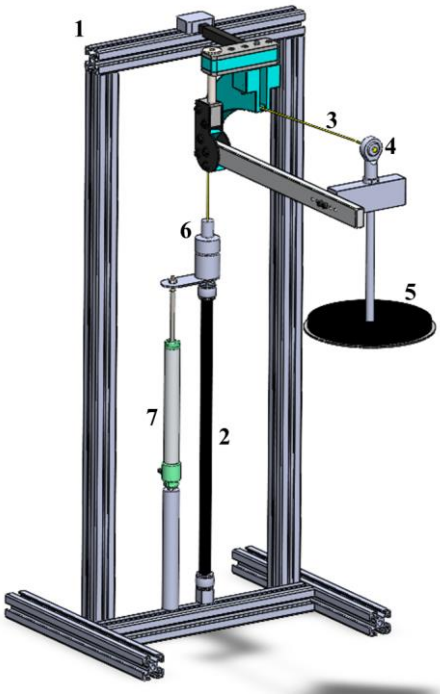

Figure 5.1 Test-bench developed for the torque generator characterization.

The exo-arm and the MKM lower end are attached to a fixed frame (1). The upper end of the MKM (2) instead is connected to a cable (3) that wraps around the

shoulder pad and connects to a stainless-steel hook (4) placed at a distance of 250 mm from J_h. A known load (5) is also attached to the hook. A uniaxial load cell (UMM, 100 kgf, Dacell Co. Ltd., Cheongju, Korea, 6) mounted between the muscle and the cable measured the MKM tensile force. A linear displacement transducer (PZ-34-A-100, Gefran S.p.A., Provaglio D'Iseo, Italy, 7) is linked in parallel to the MKM to measure its length variation. The exo-arm flexion angle is measured with a digital protractor. Finally, the supply pressure is manually adjusted through a reducer and measured through a pressure gauge installed near the muscle. The signals of the transducers are acquired through a digital multimeter.

The torque generator performance is evaluated for three different MKM supply pressures: 3 bar, 4 bar, and 5 bar. For each supply pressure value, the progressive sequence of loads from 0 kg to 5 kg, listed in Table 5.1, is applied to the stainless-steel hook. For each external load considered, the values of the flexion angle, the MKM length, and the MKM traction force are recorded once the static balance between the gravitational torque and the torque exerted by the MKM has been reached. The MKM length variation detected during the tests is shown in Figure 5.2, together with the MKM theoretical length variation estimated in Chapter 2.

Table 5.1 Static characterization data. m is the external load; p is the supply pressure; k is the MKM contraction ratio; F_{MKM} is the MKM traction force; θ is the exoskeleton flexion angle,

p (bar)	m (kg)	k (%)	F_{MKM} (N)	θ (°)
3	0	14.2	14	132
	1.18	10.6	62	110
	2.15	6.7	114	93
	3.15	5.3	132	78
	4.15	4.6	144	72
	5.15	3.9	156	66
4	0	16.2	38	135
	1.18	11.8	102	107
	2.15	9.8	132	92
	3.15	7.7	158	81
	4.15	6.9	176	73
	5.15	6.6	178	69
5	1.18	15.6	92	120
	2.15	12.6	148	97
	3.15	11.4	162	92
	4.15	10.5	176	81
	5.15	10.1	186	74

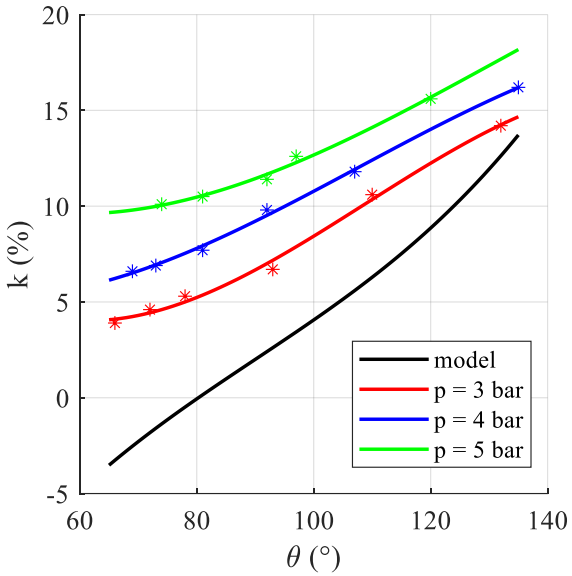

Figure 5.2 Muscle shortening measured during static characterization tests.

It can be noted that the experimental results are quite different from the simulated ones. It is probably due to the exo-arm deformation resulting from the load application. Both gravitational and MKM traction forces application caused the shoulder pad to lower. Therefore, the shoulder pad and MKM were closer to each other, and a shorter cable would be necessary to reach the same flexion angle. Since the cable is inextensible, the muscle undergoes a higher shortening than estimated to compensate for the deformation of the structure. Decreasing the external load increases the flexion angle and requires further muscle shortening. At the same time, the exo-arm returns to its undeformed condition, causing the elongation of MKM. The overall effect of these two opposing behaviors is that for a flexion angle ranging between 60° and 135°, MKM shortens by a smaller amount than estimated. The slope of the experimental curves (Figure 5.2, colored lines) is less than that of the theoretical curve (Figure 5.2, black line). An overall shortening of about 10% is measured in the explored working range instead of the estimated 17%. In addition, the MKM shortening depends on the supply pressure, whereas in the modeled case, the MKM shortening is determined only by the shoulder flexion angle.

The contraction ratio affects the MKM traction force, as detailed in Chapters 1 and 2. In particular, the measured F_{MKM} is less than estimated (Figure 5.3). Therefore, higher supply pressures are needed to obtain the desired support torque. The difference between the measured and the estimated force increases exponentially below 90°. As a result, the support torque provided by the exoskeleton increases less than shown in Figure 2.19, so lowering the arm should be less demanding for the users.

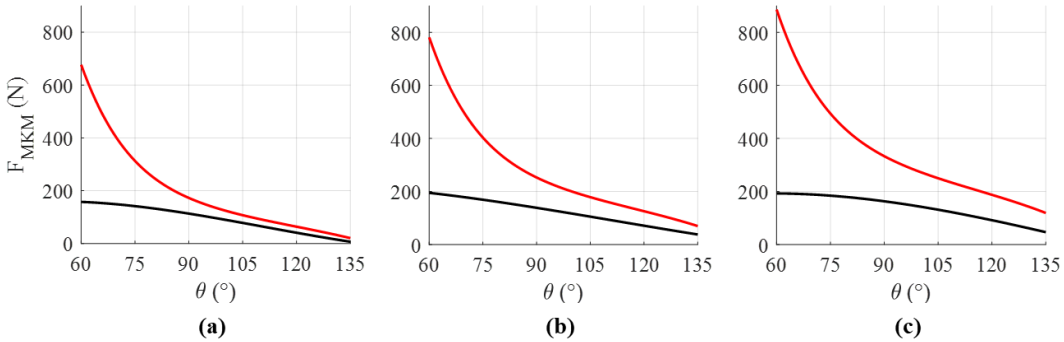

Figure 5.3 Measured (black lines) and estimated (red lines) MKM traction forces at different supply pressures. (a) p = 3 bar; (b) p = 4 bar; (c) p = 5 bar.

Chapter 6

Experimental validation

Experimental tests simulating overhead works to assess the effectiveness of the exoskeleton and any undesired effects are performed in the laboratory. The device is evaluated through an assessment method based on a large set of measures to estimate both desired and undesired effects. The exoskeleton assistive ability is verified by monitoring shoulder muscles' activity. On the other hand, the undesired effects onset is studied by evaluating the effort of low-back muscles and the subject balance performance. Finally, the shoulder and elbow kinematics and the position of the exoskeleton joint center are investigated to quantify any misalignments between the exoskeleton and the user's anatomy during the tasks.

The instrumentation, monitored parameters, and analysis algorithms implemented for conducting experimental tests and analyzing the collected data will be detailed in Section 6.1. The experimental protocol will be described in Section 6.2. Finally, the obtained results will be presented and discussed in Sections 6.3 and 6.4, respectively.

6.1 Data recording

6.1.1 EMG data

Muscular activity is monitored using the Wave Plus multichannel wireless surface electromyographic system (Cometa, Italy). Common mode rejection ratio of 120 dB, input impedance of 20 MΩ, and a gain of 1000. Surface EMG pre-gelled, bipolar electrodes (silver-silver chloride electrodes, 24 mm, GEA soluzioni, Italy) are placed over the shoulder and low back muscles following the SENIAM recommendations.

The position of the electrodes is described below for each of the monitored muscles:

- Anterior deltoid (Figure 6.1). The first electrode is positioned by moving from the acromion of a finger both in the distal and anterior direction. The second electrode is placed 20 mm away from the first in the direction of the line from the acromion to the thumb. If the electrodes are correctly positioned, the EMG signal appears with the shoulder abduction in slight flexion and the humerus in slight rotation.

Figure 6.1 EMG electrodes location in Anterior Deltoid. Black cross indicates acromion position.

- Middle deltoid (Figure 6.2). The electrodes are placed on the line from the acromion to the lateral epicondyle of the elbow, on the bulge of the muscle. The inter-electrode distance was about 20 mm. The correct placement of the electrodes can be checked by abducting the shoulder while the elbow is flexed to avoid a simultaneous rotation of the humerus. After reaching the desired shoulder position, the elbow can be extended to increase the gravitational load and ensure a higher increase in the EMG signal.

Figure 6.2 EMG electrodes location in Middle Deltoid. Black cross indicates acromion position. Blue cross indicates lateral epicondyle of the elbow position.

- Latissimus dorsi (Figure 6.3). The first electrode is about 4 cm below the lower edge of the scapula and half the distance between the spine and the lateral edge of the torso. The second electrode is positioned along the direction that forms an angle of about 25° with the horizontal, moving about 20 mm laterally from the first electrode [120]. The onset of the EMG signal is visible during shoulder adduction with the arm slightly flexed.

Figure 6.3 EMG electrodes location in Latissimus Dorsi. Grey dashed line indicates the lower edge of the scapula.

- Longissimus (Figure 6.4). The first electrode is positioned starting from the spinous process L1 and moving two fingers in the lateral direction. The second electrode is 20 mm above the first. EMG activity is observed as the subject lifts the trunk from a prone position to check the correct placement of the electrodes.

Figure 6.4 EMG electrodes location in Longissimus. Black cross indicates L1 position.

- Iliocostalis (Figure 6.5). Firstly, the posterior iliac spine must be identified. Then, move one finger in the medial direction and draw the line connecting this point to the lowest point of the last rib. The first electrode is placed on this line at the L1 level, while it is necessary to move 20 mm along the line towards the rib to place the second electrode. As for the longissimus, the correct positioning can be verified by lifting the trunk from a prone position.

Figure 6.5 EMG electrodes location in Iliocostalis. Black cross indicates the lowest point of the last rib. Light blue cross indicates the posterior iliac spine. Yellow cross indicate L1 position.

Electrodes are placed bilaterally on both the right and left muscles. The skin is shaved and cleaned with alcohol before applying the electrodes to ensure better adhesion. Finally, the electrodes' placement correctness is checked thanks to the real-time graphical user interface.

EMG data are sampled at 1000 Hz and post-processed with a customized script in MATLAB 2022 (MathWorks Inc., MA, USA). Raw EMG signals are high pass filtered (4th Butterworth filter with 10 Hz cut-off frequency) and low pass filtered (4th Butterworth filter with 450 Hz cut-off frequency) to remove high-frequency noise and movement artifact. Then, EMG signals are rectified.

6.1.2 Kinematics data

Shoulder and elbow kinematics are monitored using a twelve-camera optical motion capture system (Vicon Nexus). Since the exoskeleton movements must be tracked, the Vicon standard template designed to calculate the human upper body kinematics, namely Plug-in-Gait upper body (PiG-ub), cannot be used. Therefore, a custom labeling skeleton template to model the trunk, the upper limbs, and a part of the exoskeleton has been defined. The designed marker set consists of 17 markers on the subject and 6 markers on the exoskeleton.

The markers placed on the subject, shown in Figure 6.6, are:

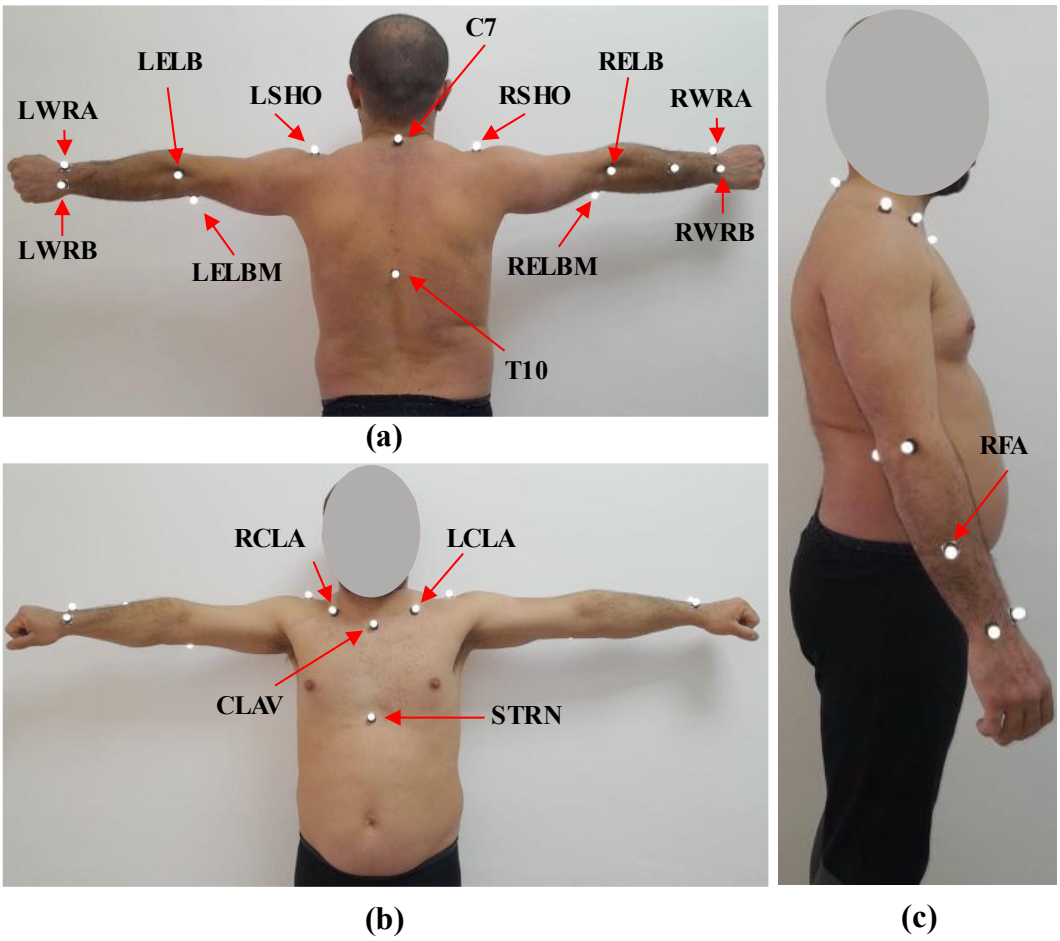

Figure 6.6 Back (a), front (b), and right-side view (c) of the marker set placed on the subject.

- Torso markers:
  - C7, placed on the spinous process of the 7th cervical vertebra.
  - T10, placed on the spinous process of the 10th vertebra.
  - STRN, placed on the xiphoid process of the sternum.
  - CLAV, placed on the suprasternal notch.
- Right upper limb markers:
  - RSHO, placed on the right acromion clavicular joint.
  - RCLA, placed on the right clavicle, halfway between RSHO and CLAV.
  - RELB, placed on the lateral epicondyle of the right humerus.
  - RELBM, placed on the medial epicondyle of the right humerus.
  - RFA, anywhere over the right forearm. It just facilitates automatic marker labeling. It is not used to derive kinematic variables.
  - RWRA, placed on the medial side of the right wrist.
  - RWRB, placed on the lateral side of the right wrist.
- Left upper limb markers:

- LSHO, placed on the left acromion clavicular joint.
- LCLA, placed on the left clavicle, halfway between LSHO and CLAV.
- LELB, placed on the lateral epicondyle of the left humerus.
- LELBM, placed on the medial epicondyle of the left humerus.
- LWRA, placed on the medial side of the left wrist.
- LWRB, placed on the lateral side of the left wrist.

The markers placed on the exoskeleton, shown in Figure 6.7, are:

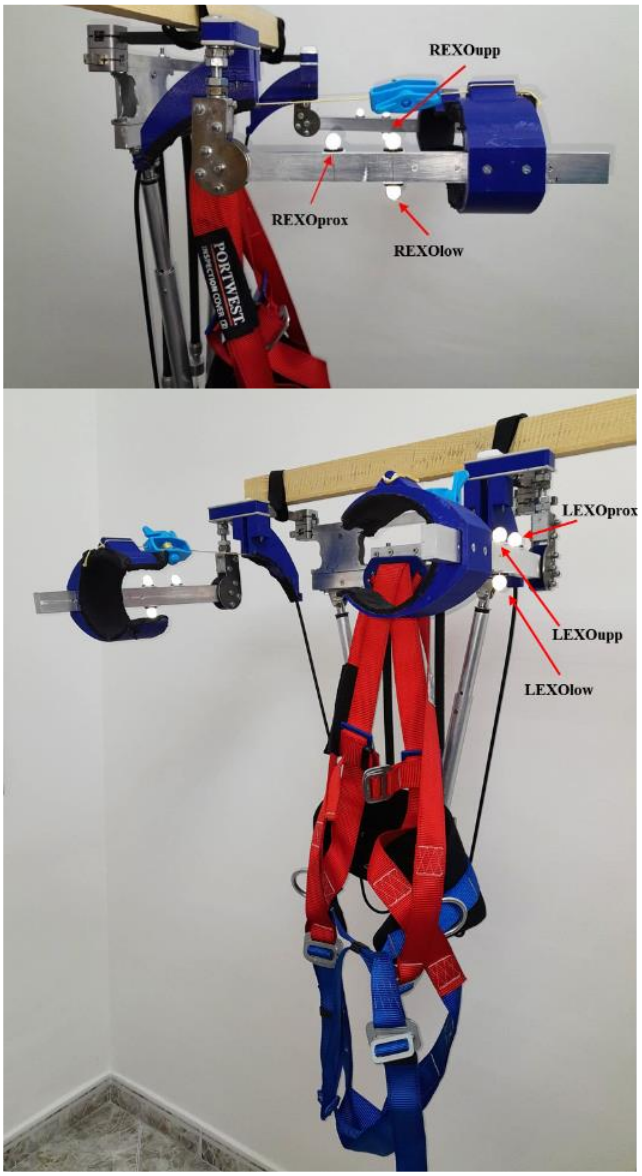

Figure 6.7 Marker set placed on the exoskeleton.

- REXOprox, placed on the upper face of the exoskeleton strut that runs parallel to the right upper arm of the user at a distance of 10 cm from the horizontal hinge.
- REXOupp, placed on the upper face of the exoskeleton strut that runs parallel to the right upper arm of the user at a distance of 15 cm from the horizontal hinge.
- REXOlow, placed on the lower face of the exoskeleton strut that runs parallel to the right upper arm of the user at a distance of 15 cm from the horizontal hinge.
- LEXOprox, placed on the upper face of the exoskeleton strut that runs parallel to the left upper arm of the user at a distance of 10 cm from the horizontal hinge.
- LEXOupp, placed on the upper face of the exoskeleton strut that runs parallel to the left upper arm of the user at a distance of 15 cm from the horizontal hinge.
- LEXOlow, placed on the lower face of the exoskeleton strut that runs parallel to the left upper arm of the user at a distance of 15 cm from the horizontal hinge.

It should be noted that the adopted marker set is similar to the PiG-ub, with the addition of markers on the exoskeleton, the humerus medial epicondyle (RELBM and LELBM), and the clavicle (RCLA and LCLA). RELBM, LELBM, RCLA, and LCLA are redundant markers. They are not directly necessary to obtain the joint centers and angles but can help reconstruct the trajectory of other markers not visible to the cameras during movement. In particular, the redundant markers allowed the reconstruction of C7, RSHO, LSHO, RELB, and LELB trajectories through a methodology detailed in the following.

Marker trajectories are sampled at 100 Hz. Raw trajectory data are low pass filtered (4th Butterworth filter with 6 Hz cut-off frequency) to remove movement artifacts. The shoulder joint center, the flexion-extension angle of both shoulder and elbow, the abduction-adduction angle of the shoulder, and the position of the flexion-extension axis of the exoskeleton are obtained from the trajectories of the markers thanks to a custom MATLAB script, provided in Appendix A. The post-processing algorithm consists of four phases:

1. data check;
2. calculation of the joints center;
3. calculation of the joints angles;
4. calculation of the exoskeleton joints center position.

Data check

The initial stage checks that the required subject parameter values and marker trajectories are present. The biomechanical model requests the following fixed parameters to run correctly:

- the diameter of the markers;
- the vertical distance between the center of the glenohumeral joint and the acromion (shoulder offset);
- the distance between the medial and lateral epicondyle of the humerus (elbow offset);
- the thickness of the wrist in the direction from the palm to the back of the hand (wrist offset).

All anthropometric measurements should be repeated for both the right and left side.

Missing data in the marker trajectory is estimated using a cubic-spline interpolation method if gaps are less than 100 frames. In the case of wider gaps, the trajectory is reconstructed from the position of the other markers. For this purpose, a preliminary static acquisition is made to calculate the distance of two markers, A and B, belonging to the same body segment in a marker-based reference system $\vec{u}\,\vec{v}\,\vec{w}$. Knowing the trajectory of B during the experimental task and the distance AB, it is possible to derive the position of A.

C7 trajectory can be found by creating the $\vec{u}\,\vec{v}\,\vec{w}$ reference system in which: $\vec{u}$ is parallel to the line between STRN and CLAV, $\vec{w}$ is perpendicular to the plane containing STRN, CLAV, and T10, while $\vec{v}$ is at right angles to both $\vec{u}$ and $\vec{w}$.

Similarly, SHO trajectory can be obtained by defining the $\vec{u}\,\vec{v}\,\vec{w}$ reference system, with $\vec{u}$ parallel to the line between CLAV and the thorax origin (described below), $\vec{w}$ perpendicular to the plane containing CLA, CLAV and the thorax origin, and $\vec{v}$ at right angles to both $\vec{u}$ and $\vec{w}$.

Finally, ELB trajectory can be obtained by defining the $\vec{u}\,\vec{v}\,\vec{w}$ reference system where $\vec{u}$ is parallel to the line between WRB and ELBM, $\vec{w}$ is perpendicular to the plane containing WRB, ELBM, and SHO, while $\vec{v}$ is at right angles to both $\vec{u}$ and $\vec{w}$.

As an example, the mathematical steps to derive the position of C7 are illustrated in Equations 6.1-6.4:

$$\vec{u} = \frac{\overrightarrow{\mathrm{CLAV_s}} - \overrightarrow{\mathrm{STRN_s}}}{|\overrightarrow{\mathrm{CLAV_s}} - \overrightarrow{\mathrm{STRN_s}}|} \tag{6.1}$$

$$\vec{w} = \frac{\left(\overrightarrow{CLAV_s} - \overrightarrow{STRN_s}\right) \wedge \left(\overrightarrow{T10_s} - \overrightarrow{STRN_s}\right)}{\left|\left(\overrightarrow{CLAV_s} - \overrightarrow{STRN_s}\right) \wedge \left(\overrightarrow{T10_s} - \overrightarrow{STRN_s}\right)\right|} \tag{6.2}$$

$$\vec{v} = \vec{w} \wedge \vec{u} \tag{6.3}$$

$$\Delta = \begin{bmatrix} \vec{u} \\ \vec{v} \\ \vec{w} \end{bmatrix} \cdot \overrightarrow{C7_s} - \begin{bmatrix} \vec{u} \\ \vec{v} \\ \vec{w} \end{bmatrix} \cdot \overrightarrow{CLAV_s} \tag{6.4}$$

In Equations 6.1 - 6.4, the subscript s indicate that the trajectories are acquired during the static preliminary test. Known Δ, the coordinates of C7 during any other task performed by the same subject can be calculated by making the difference between the coordinates of CLAV in the reference system $\vec{u}\,\vec{v}\,\vec{w}$ and Δ.

A ROM trial (i.e., a trial in which the shoulder range of movement is explored) is acquired to validate the reconstruction algorithm by comparing the reconstructed trajectories with those measured by VICON. Figure 6.8 shows the coordinates expressed in the laboratory global reference system of the markers C7 (Figure 6.8a), RSHO (Figure 6.8b) and RELBM (Figure 6.8c) acquired by VICON (continuous lines) and reconstructed (thick dashed lines). The reconstruction of RSHO is the least accurate, maybe because the distance between RSHO and RCLA may not always be exactly constant due to the movement of the clavicle during the arm flexion. However, the root mean square error between the acquired and the estimated trajectory is always less than 10 mm (Table 6.1) and is considered adequate for the application.

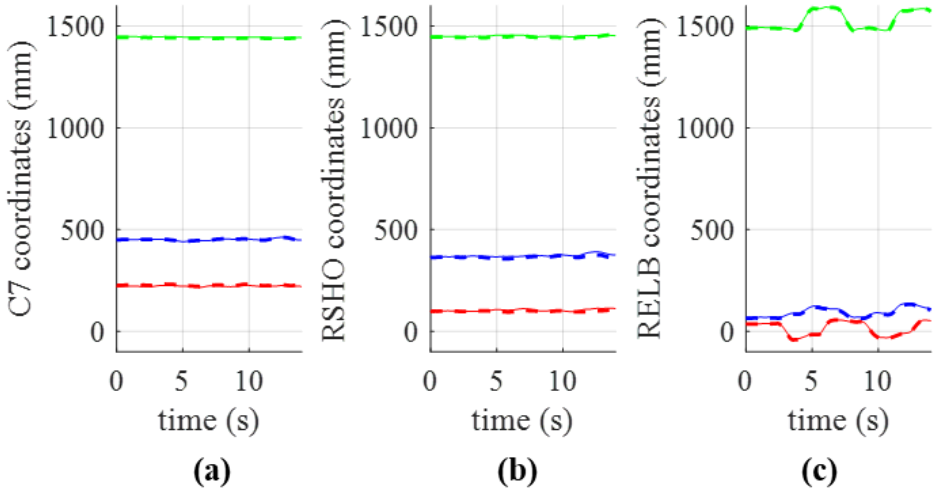

Figure 6.8 Coordinates in the global reference system of the laboratory of the markers C7 (a), RSHO (b), and RELB (c). The continuous lines represent the acquired trajectories, while the thick dashed lines represent the reconstructed trajectories. The X, Y, and Z coordinates are shown in red, blue and green, respectively.

Table 6.1 Mean square error between the reconstructed and acquired trajectories of the marker C7, RSHO, and RELB

Marker	X	Y	Z
C7	4.88 mm	0.47 mm	4.40 mm
RSHO	6.45 mm	8.70 mm	5.28 mm
RELB	2.10 mm	4.68 mm	2.17 mm

Calculation of the joints' centers

The second step consists of obtaining the coordinates of the shoulder joint center (SJC), the elbow joint center (EJC), and the wrist joint center (WJC). Although only SJC affects the performance of the exoskeleton, EJC and WJC are used to calculate the joint angles.

The chord function, used in the PiG models, is exploited to define SJC and EJC. The coordinates of 3 points (I, J, and K) are required to identify the joint center (JC) position (Figure 6.9).

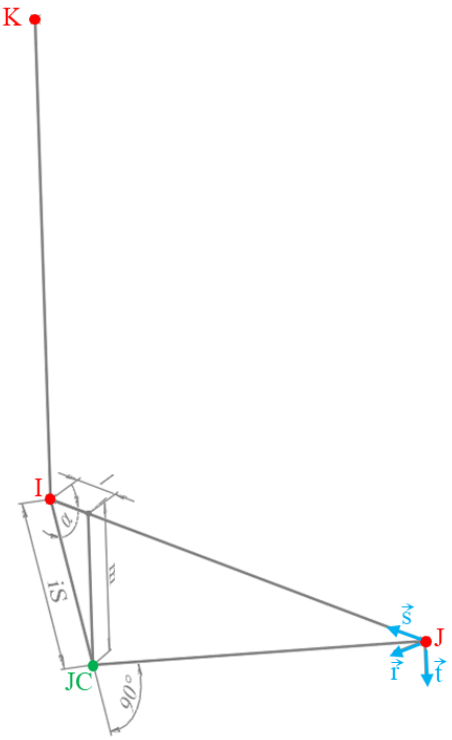

Figure 6.9 Descriptive scheme of the chord function. I, J, and K (red dots) are the coordinates of the points the function requires. s, r, and t (blue arrows) define the right-hand reference system based on the coordinates of points I, J, and K. Finally, JC is the position of the required joint center (green dot).

J could be a previously calculated JC or the origin of the proximal body segment of the joint. I is a marker placed at a distance iS from the required JC. iS coincides with one of the anthropometric measurements requested by the algorithm (shoulder

offset or elbow offset). K is the virtual marker that defines the plane where the angle I-JC-J equals 90°.

The coordinates of these three points are used to define three axes $\vec{s}$, $\vec{r}$, and $\vec{t}$.

- $\vec{s}$ is parallel to the line between J and I.
- $\vec{r}$ is perpendicular to the plane formed by the three points. Its direction is shown in Figure 6.9.
- $\vec{t}$ is at right angles to both $\vec{s}$ and $\vec{r}$ so that the three axes form a right-handed system.

JC coordinates can then be derived by moving from I along $\vec{s}$ and $\vec{t}$ by an amount equal to -l and m, respectively. l and m depend on iS as shown by Equations 6.5 - 6.7.

$$l = iS * \cos(\alpha) \tag{6.5}$$

$$m = \sqrt{iS^2 - l^2} \tag{6.6}$$

$$\cos(\alpha) = \frac{iS}{\overline{IJ}} \tag{6.7}$$

To estimate SJC, the points I, J, and K are respectively the marker SHO, the thorax origin, and the virtual marker located in the direction perpendicular to the line from the thorax origin to the SHO, and the thorax u-axis. iS is the shoulder offset (Figure 6.10a). Firstly, the thorax local reference system $\overrightarrow{x_t}\,\overrightarrow{y_t}\,\overrightarrow{z_t}$ must be defined as follows:

$$\overrightarrow{z_t} = \frac{\frac{\overrightarrow{C7} + \overrightarrow{CLAV}}{2} - \frac{\overrightarrow{T10} + \overrightarrow{STRN}}{2}}{\left|\frac{\overrightarrow{C7} + \overrightarrow{CLAV}}{2} - \frac{\overrightarrow{T10} + \overrightarrow{STRN}}{2}\right|} \tag{6.8}$$

$$\overrightarrow{y_t} = \frac{\overrightarrow{z_t} \wedge \left(\frac{\overrightarrow{C7} + \overrightarrow{T10}}{2} - \frac{\overrightarrow{CLAV} + \overrightarrow{STRN}}{2}\right)}{\left|\overrightarrow{z_t} \wedge \left(\frac{\overrightarrow{C7} + \overrightarrow{T10}}{2} - \frac{\overrightarrow{CLAV} + \overrightarrow{STRN}}{2}\right)\right|} \tag{6.9}$$

$$\overrightarrow{x_t} = \overrightarrow{y_t} \wedge \overrightarrow{z_t} \tag{6.10}$$

Then, the thorax origin (O_t) can be estimated by Equation 6.11:

$$\overrightarrow{O_t} = \overrightarrow{CLAV} - \frac{\text{Marker Diameter}}{2} * \overrightarrow{x_t} \quad (6.11)$$

On the other hand, to estimate EJC, the points I, J, and K are respectively the marker ELB, SJC, and the virtual marker located in the direction perpendicular to the plane containing SJC, ELB, and the midpoint between WRA and WRB. iS is the elbow offset (Figure 6.10b).

Finally, WJC is calculated by moving from the midpoint of WRB and WRA by an amount equal to wrist offset along the perpendicular to the line joining WRB and WRA and the line joining the midpoint of WRA and WRB to EJC (Figure 6.10c).

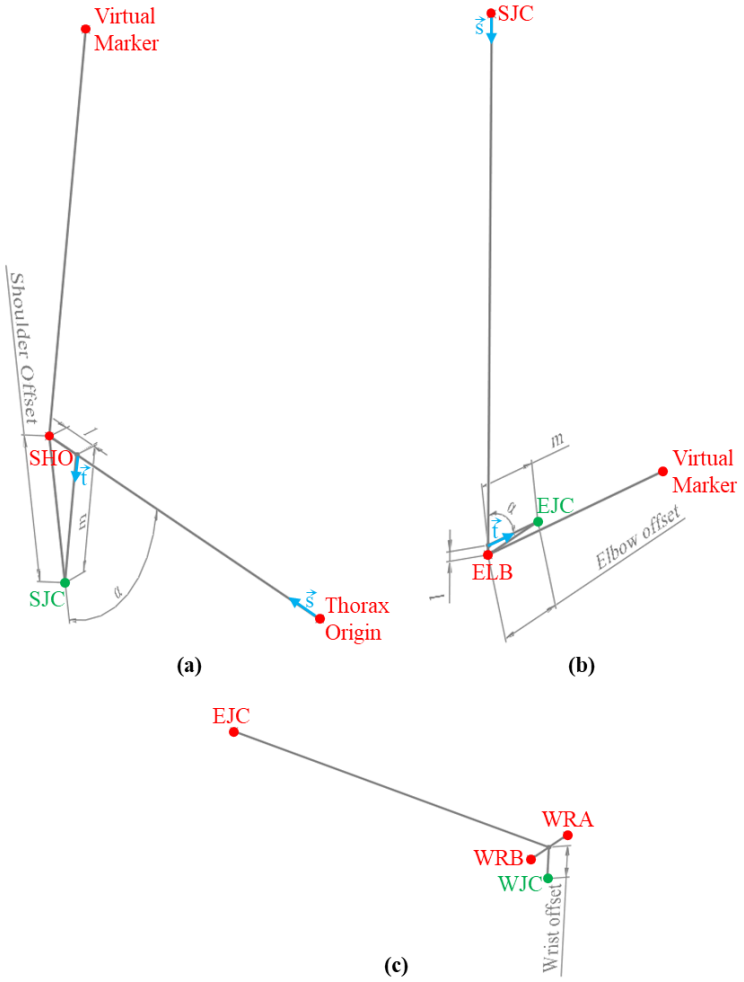

Figure 6.10 Descriptive scheme of the algorithm used for the calculation of SJC (a), EJC (b) and WJC (c).

Calculation of the joint's angles

The third step calculates the angle of flexion/extension of the shoulder, the angle of abduction/adduction of the shoulder, and the angle of flexion/extension of the elbow. Each joint angle is calculated from the Cardan angles derived by comparing the relative orientations of the distal and proximal segments of the joint.

To describe an angle using the three-angle representation, the proximal segment is fixed while the distal segment performs the following ordered rotations:

- The first rotation is measured about the medium-lateral axis of the proximal body segment and represents the flexion/extension of the joint. A positive value corresponds to a flexion.
- The second rotation is measured about the anterior-posterior axis of the distal segment and defines the abduction/adduction of the articulation. A positive value corresponds to abduction.
- The third rotation is measured about the longitudinal axis of the distal segment and defines intra/extra rotation. A positive value corresponds to external rotation.

The fixed and mobile segments of the shoulder are the thorax and the humerus, respectively. The anatomical reference system of the thorax has been defined previously (Equations 6.8 - 6.10). The anatomical reference system of the humerus, instead, has the z-axis ($\overrightarrow{z_h}$) parallel to the line from EJC to SJC (Equation 6.12), the y-axis ($\overrightarrow{y_h}$) perpendicular to $\overrightarrow{z_h}$ and the line from EJC to WJC (Equation 6.13), and the x-axis ($\overrightarrow{x_h}$) perpendicular to the first two (Equation 6.14).

$$\overrightarrow{z_h} = \frac{\overrightarrow{SJC} - \overrightarrow{EJC}}{\left|\overrightarrow{SJC} - \overrightarrow{EJC}\right|} \tag{6.12}$$

$$\overrightarrow{y_h} = \frac{\overrightarrow{z_h} \wedge \left(\overrightarrow{WJC} - \overrightarrow{EJC}\right)}{\left|\overrightarrow{z_h} \wedge \left(\overrightarrow{WJC} - \overrightarrow{EJC}\right)\right|} \tag{6.13}$$

$$\overrightarrow{x_h} = \overrightarrow{y_h} \wedge \overrightarrow{z_h} \tag{6.14}$$

Once the anatomical reference systems have been defined, the shoulder flexion/extension and abduction/adduction can be derived. The first corresponds to the angle between $\overrightarrow{z_h}$ and $\overrightarrow{z_t}$ calculated around $\overrightarrow{y_t}$. The second coincides with the angle between $\overrightarrow{y_h}$ and $\overrightarrow{y_t}$ calculated around $\overrightarrow{z'_h}$, which is the orientation of $\overrightarrow{z_h}$ after the first rotation.

On the other hand, the fixed and mobile segments of the elbow are the humerus and the radius, respectively. The anatomical reference system of the radius has the z-axis ($\overrightarrow{z_r}$) parallel to the line from WJC to EJC (Equation 6.15), the y-axis ($\overrightarrow{y_r}$) parallel to $\overrightarrow{y_h}$, and the x-axis ($\overrightarrow{x_r}$) perpendicular to the first two.

$$\overrightarrow{z_r} = \frac{\overrightarrow{EJC} - \overrightarrow{WJC}}{\left|\overrightarrow{EJC} - \overrightarrow{WJC}\right|} \tag{6.15}$$

The elbow flexion angle corresponds to the angle between $\overrightarrow{z_h}$ and $\overrightarrow{z_r}$ calculated around $\overrightarrow{y_h}$.

Calculation of the exoskeleton joint center

In the last step, the algorithm calculates the position of the horizontal axis hinge of the exoskeleton J_h. First, a technical reference system of the exoskeleton $(\overrightarrow{x_{exo}}, \overrightarrow{y_{exo}}, \overrightarrow{z_{exo}})$ is defined using the coordinates of the three markers on the exo-arm. $\overrightarrow{x_{exo}}$ is directed from EXO_{prox} to the EXO_{upp}, $\overrightarrow{z_{exo}}$ is perpendicular to the plane that contains the three markers, and $\overrightarrow{y_{exo}}$ is perpendicular to the first two. The position of J_h can then be identified starting from the position of EXO_{prox} and moving of -10 cm long $\overrightarrow{x_{exo}}$ and of an amount equal to half the distance between EXO_{upp} and EXO_{low} long $\overrightarrow{z_{exo}}$.

6.1.3 Balance performance

The coordinates on the transverse plane of the center of the pressures exchanged between foot and ground (CoP) are provided by the force platform (BMS series, AMTI, USA). The latter measures the CoP displacement in the anteroposterior (AP_o) and mediolateral (ML_o) direction with respect to the origin of the force platform coordinate system. AP_o and ML_o are sampled at 1000 Hz and passed through a fourth-order zero-phase Butterworth low-pass digital filter with a 20 Hz cut-off frequency. The CoP coordinates are then referred to their average position by subtracting the arithmetic mean from AP_o and ML_o. The time series thus obtained (AP and ML) have been used to calculate the RMS amplitude.

The RMS amplitude (CoP_{rms}) is the RMS value of the distance, calculated in the transverse plane, between the CoP instantaneous position and the CoP average position:

$$CoP_{rms} = \sqrt{\frac{1}{N}\sum_{n=1}^{N}\left(\sqrt{AP(n)^2 + ML(n)^2}\right)^2} \tag{6.16}$$

In Equation 6.16, N is the CoP number of samples.
An increased CoP_{rms} value suggests a decreased ability to maintain postural control.

6.2 Experimental protocol

The experiments took place at the interdepartmental center Polito^{BIO}MedLab of Politecnico di Torino. Two healthy subjects (one male, and one female), whose anthropometric characteristics are reported in Table 6.2, are recruited for the experiments. Both participants were right-handed and had no prior experience with the exoskeleton.

Markers and EMG electrodes are placed on subjects following the protocol described in Section 6.1. After that, subjects are asked to stand on the force platform and perform static and dynamic tasks.

Table 6.2 Subjects anthropometric characteristics. r and l apices refer to the right and left arm, respectively.

Subject	Gender	Height (m)	Weight (kg)	Age (years)	Shoulder offset (cm)	Elbow offset (cm)	Wrist offset (cm)
1	F	1.72	80	31	30 (r) 32 (l)	61 (r) 61 (l)	40 (r) 38 (l)
2	M	1.60	67	34	25 (r) 25 (l)	65 (r) 63 (l)	37 (r) 38 (l)

During the static tasks, each subject is asked to stand still and keep both arms flexed, with a hand-held tool (power drill, weight = 1.2 kg) in the right hand and the elbows are in the most extended position which is comfortable for the user. Two different shoulder flexion angles are tested: 90° (Figure 6.11a) and 110° (Figure 6.11b). A reference point placed in a panel in front of the subject helps to maintain the arms in the position prescribed by the task.

During the dynamic tasks, each subject is asked to stand and follow with the right hand the outline of a rectangle (b = 20 cm; h = 30 cm) drawn on a panel in front of him/her. The panel height is set to guarantee that the shoulder flexion angle ranges between 90° and 110°. The elbows are in the most extended position which is comfortable for the user. Dynamic tasks are executed two times: with and without the presence of a tool in the right hand. In each condition, subjects are asked to repeat the movements 10 times at a self-selected pace. Before each repetition, the subject is asked to flex the elbow to facilitate the segmentation of signals in post-processing.

All participants performed all tasks wearing the exoskeleton (EXO session) and without wearing it (FREE session). The order of FREE and EXO sessions is randomized across participants. A rest period of at least 5 minutes has been allowed between tasks.

Before starting the EXO session, the exoskeleton structure is adapted to fit the physical characteristics of each participant. The arm bracelets are positioned 10 cm

from the elbow. The assistive level is set to fully compensate for the gravitational torque when the shoulder is flexed to 90° while the elbow is extended. The supply pressures are set equal to 6.5 bar or 4.5 bar, depending on whether the tool is held in the hand.

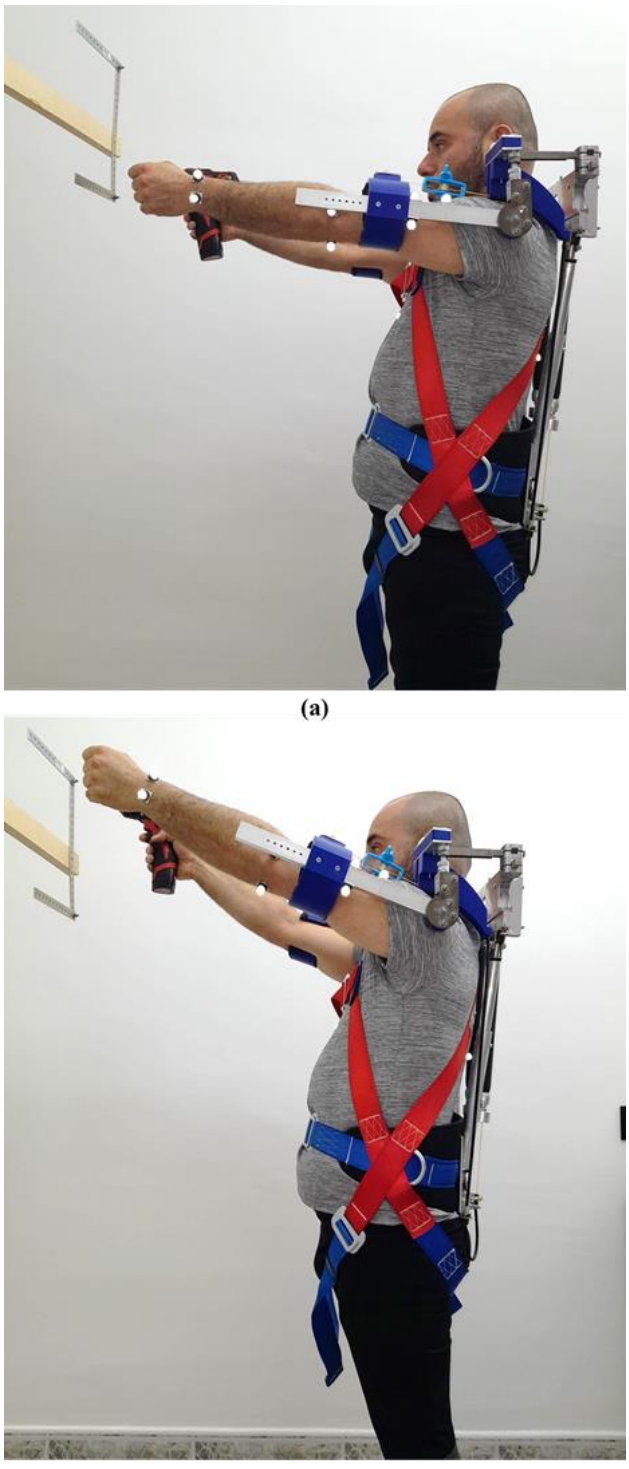

Figure 6.11 Static task. The shoulder flexion angle is equal to 90° (a) or 110° (b)

Two different procedures are considered to calculate the performance parameters (ARV, CoP_{rms}, shoulder flexion and abduction angles, SJC-ExoJC misalignments) according to the experimental task type. In static tasks, performance parameters are calculated in the last 50 s of the acquisition (Figure 6.12).

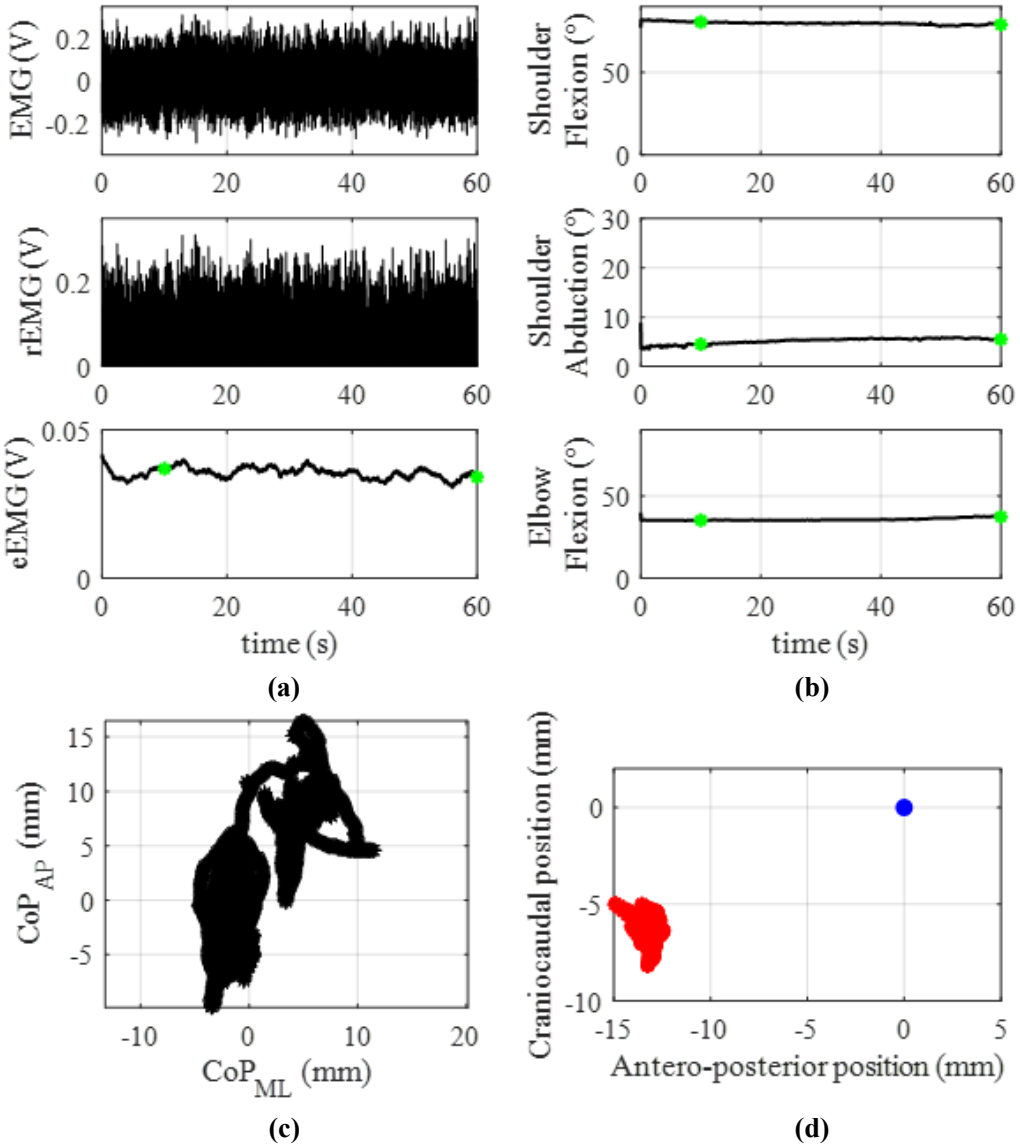

Figure 6.12 A representative recording of the EMG signal (a), shoulder and elbow angles (b), CoP displacement (c), and SJC (red dots) and ExoJC (blue dot) position in the upper-arm elevation plane (d) observed during static tasks. In (a) and (b), the green dots define the range within the mean values of the rectified EMG and joint angles are calculated.

In dynamic tasks, performance parameters have been calculated for each repetition and the 10 values have been averaged to obtain a single index for each dynamic task. The measurement of the elbow angle is used to identify individual repeats and to segment the EMG, kinematics, and CoP signals appropriately. Each

repeat corresponds to the time interval in which the elbow flexion angle remains below a threshold defined as the sum of the elbow flexion angle at the beginning of the test and half of the standard deviation of the elbow flexion angle. (Figure 6.13).

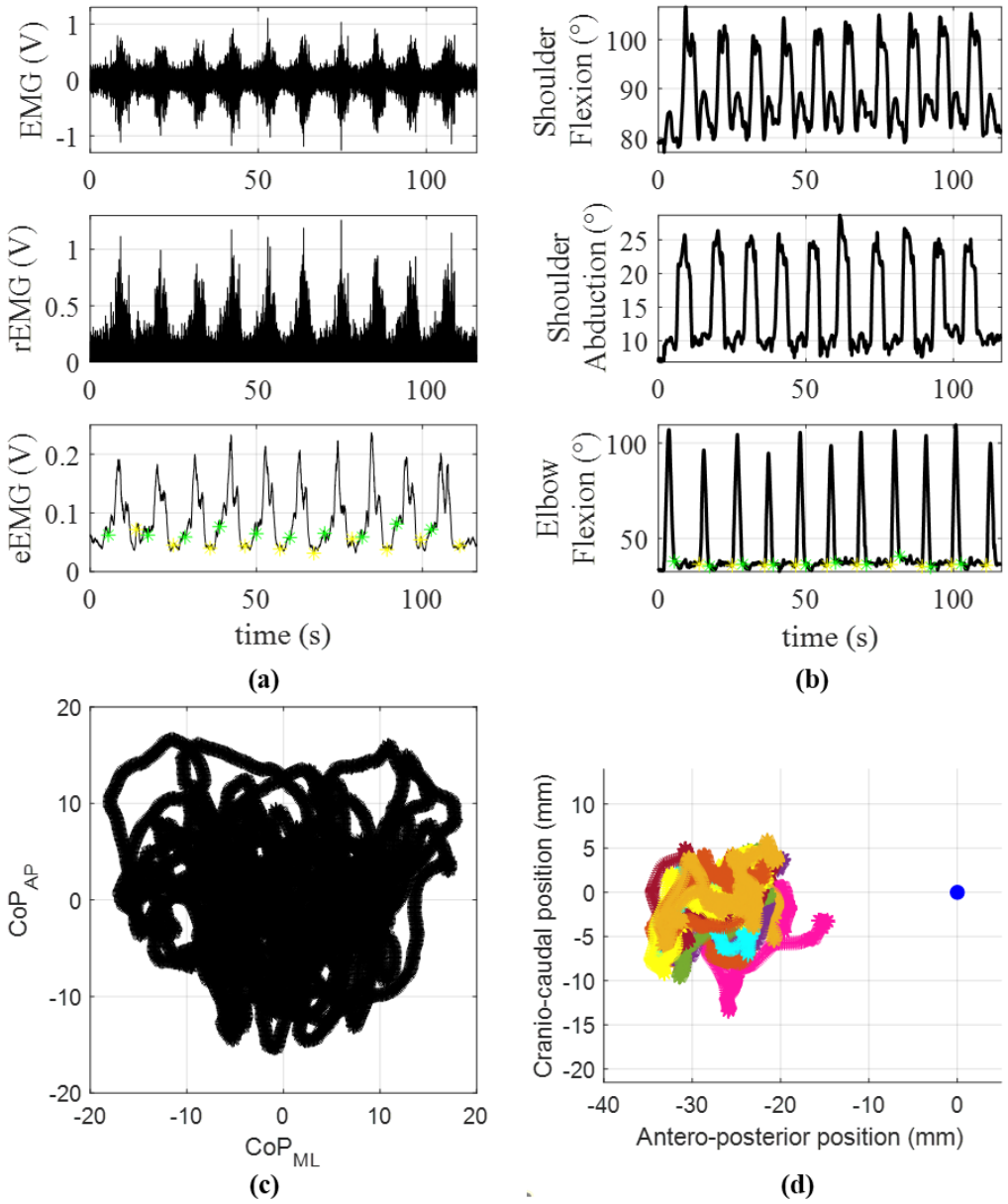

Figure 6.13 A representative recording of the EMG signal (a), shoulder and elbow angles (b), CoP displacement (c), and SJC (colored dots) and ExoJC (blue dot) position in the upper-arm elevation plane (d) observed during dynamic tasks. In (a) and (b), the green dots define the cycles start instants while the yellow dots are the end cycles instants.

6.3 Results

6.3.1 Exoskeleton assistive ability

In the static task, the shoulder flexion angles do not show substantial differences between the FREE and EXO sessions, while slight changes in the shoulder abduction angles are observed (Table 6.3).

Table 6.3 Shoulder flexion and abduction angles measured during static task. Positive values indicate flexed and abducted position, while negative values indicate extended and adducted position.

			Shoulder Flexion (°)		Shoulder Abduction (°)	
			FREE	EXO	FREE	EXO
SBJ 1	90°	Right arm	78.8 ± 1.5	79.8 ± 0.4	9.9 ± 1.1	5.3 ± 0.4
		Left arm	83.3 ± 0.9	81.6 ± 0.6	2.3 ± 0.7	5.5 ± 0.3
	110°	Right arm	98.4 ± 1.0	95.2 ± 0.3	7.0 ± 0.8	8.2 ± 0.4
		Left arm	98.5 ± 0.9	98.7 ± 0.3	4.6 ± 0.3	8.8 ± 0.2
SBJ 2	90°	Right arm	85.2 ± 0.7	87.7 ± 0.4	5.5 ± 0.4	7.4 ± 0.3
		Left arm	90.4 ± 0.5	88.9 ± 0.2	2.5 ± 0.3	6.0 ± 0.1
	110°	Right arm	108.6 ± 1.9	88.7 ± 1.5	7.0 ± 0.7	21.0 ± 1.3
		Left arm	113.7 ± 1.3	105.3 ± 0.6	2.1 ± 0.5	9.2 ± 0.4

Figure 6.14 shows the shoulder muscle ARV percentage variations between the FREE and EXO static sessions. Positive values indicate increased muscular activity in the EXO sessions, while negative values indicate decreased activations.

90° static task (Figure 6.15 a-b) highlighted a relevant reduction in the activity of the anterior deltoid (-70.0 ± 5.7 % for the right arm and -70.0 ± 9.9 % for the left arm) and middle deltoid (-57.0 ± 15.6 % for the right arm and -53.5 ± 17.7 % for the left arm). Slight reductions are also observed in the latissimus dorsi activity (-2.5 ± 2.8 % for the right arm and -6.3 ± 5.3 % for the left arm).

On the other hand, 110° static task (Figure 6.15 c-d) showed a relevant reduction in the activity of the anterior deltoid (-64.5 ± 21.9 % for the right arm and -58.5 ± 21.9 % for the left arm), the middle deltoid (-54.0 ± 15.6 % for the right arm and -36.5 ± 31.8 % for the left arm), and the right latissimus dorsi (-16.5 ± 7.8 %). On the contrary, the left latissimus dorsi ARV increased. The latissimus dorsi is responsible for horizontal abduction and extension of the shoulder joint. Although shoulder abduction increases in EXO sessions, it cannot justify the extra muscular effort. In addition, latissimus dorsi activity does not increase in any other trial, so it could be due to a measurement error or a particular psychophysical condition of the subject. Other tests will be necessary to identify the real causes.

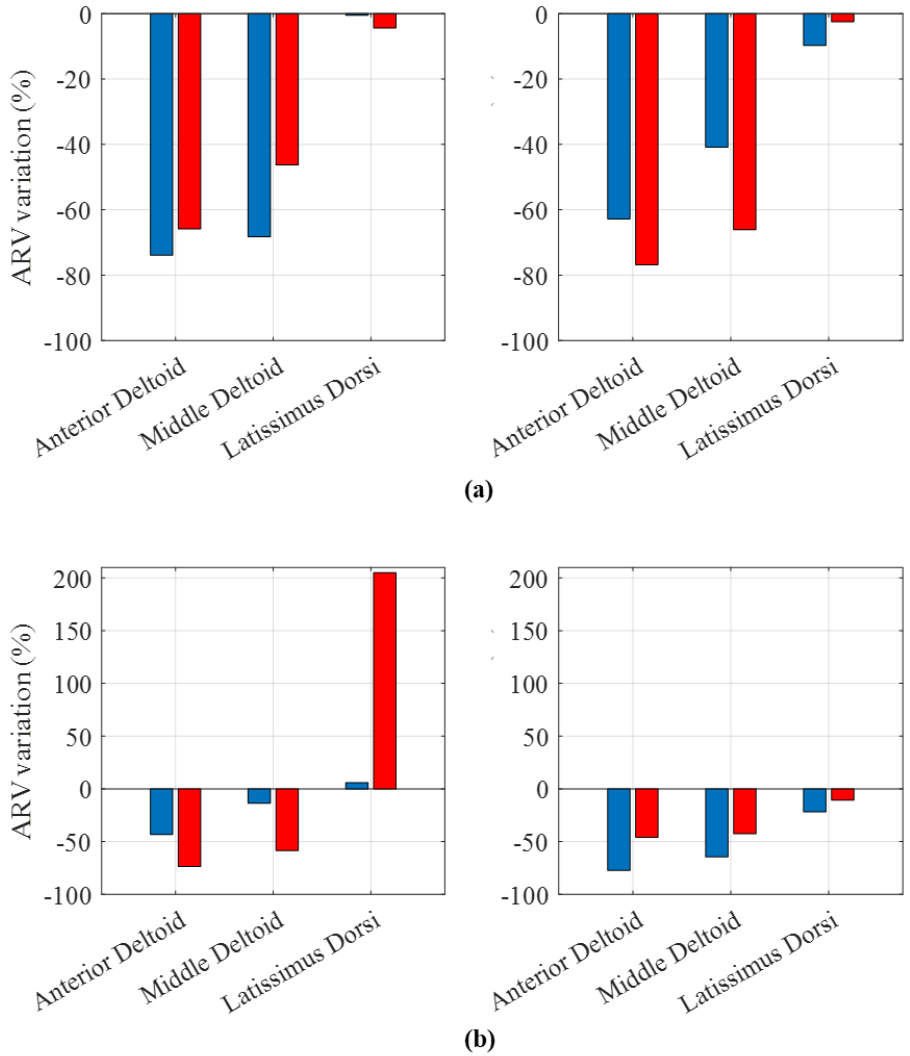

Figure 6.14 Shoulder muscles ARV percentage variation between the FREE and EXO static trial of subject 1 (blue bars) and subject 2 (red bars). (a) 90° of shoulder flexion; (b) 110° of shoulder flexion. Graphs on the left refers to left users arm while graphs on the right refers to right arm.

Dynamic tests consist of an abduction, a flexion, an adduction, and an extension performed in sequence. The motion range explored during the trials is listed in Table 6.4.

The use of the exoskeleton causes a reduction in the muscle activity of all three shoulder muscles also in dynamic tests. In tool-less tests (Figure 6.15a), the activity of the anterior deltoid, middle deltoid, and latissimus dorsi is reduced by 21.5 ± 2.1 %, 22 ± 53.7 %, and 5 ± 7.1 %, respectively. In the tool test (Figure 6.15b), the activity of the anterior deltoid, middle deltoid, and latissimus dorsi is reduced by 26 ± 15.6 %, 47.5 ± 19.8 %; 26 ± 19.8%. The slight increase of middle deltoid activity in the tool-less test executed by subject 2 can be explained by the wider abduction/adduction movements performed during the EXO session (see Table 6.4).

Table 6.4 Dynamic test workspace.

		SBJ 1		SBJ 2	
		FREE	EXO	FREE	EXO
without tool	Abduction (°)	13.5 ± 1.3	16.7 ± 1.4	16.0 ± 3.7	26.6 ± 2.7
	Flexion (°)	18.3 ± 0.7	22.0 ±2.9	36.8 ± 7.6	39.3 ± 1.1
	Adduction (°)	12.1 ± 1.0	17.4 ± 1.0	16.9 ± 3.0	29.8 ± 2.9
	Extension (°)	18.2 ± 2.1	21.6 ± 2.4	40.4 ± 4.5	42.4 ± 3.7
with tool	Abduction (°)	12.7 ± 1.1	16.1 ± 1.4	8.5 ± 5.5	16.2 ± 3.5
	Flexion (°)	15.4 ± 1.7	20.7 ± 3.0	25.6 ± 4.7	32.2 ± 2.5
	Adduction (°)	11.8 ± 0.8	17.5 ± 1.8	13.5 ±2.7	19.5 ± 2.4
	Extension (°)	17.8 ±1.4	19.2 ± 1.7	29.1 ± 3.6	34.3 ± 2.8

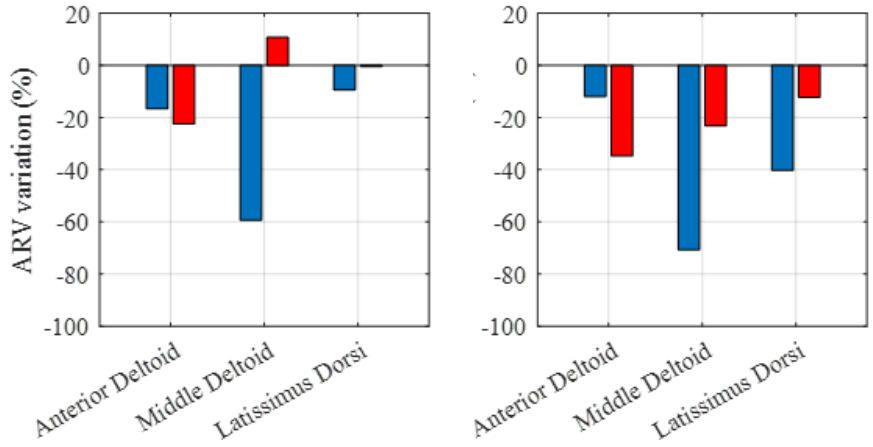

Figure 6.15 Shoulder muscles ARV percentage variation between the FREE and EXO dynamic trial of subject 1 (blue bars) and subject 2 (red bars). (a) without hand-tool; (b) with hand-tool.

6.3.2 Side effects

Figures 6.16 and 6.17 show the muscular activity measured during static and dynamic tasks of the iliocostalis and longissimus. No significant difference and/or inter-tasks repeatable trend occurred.

Finally, the rms CoP displacement increased during EXO sessions (Figure 6.18)

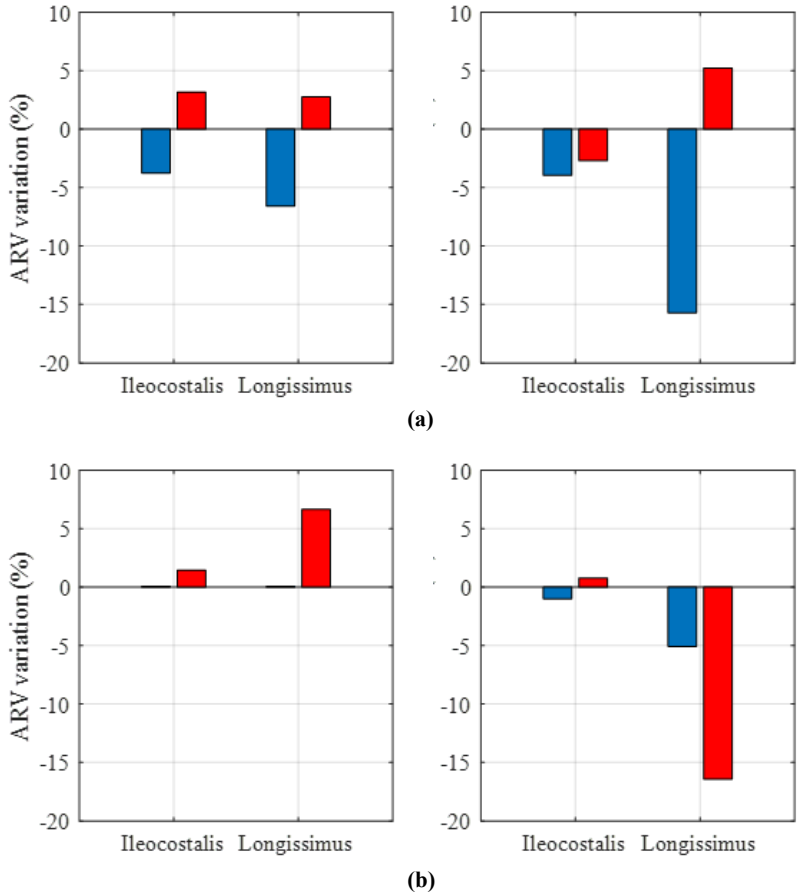

Figure 6.16 Lumbar muscles ARV percentage variation between the FREE and EXO static trial of subject 1 (blue bars) and subject 2 (red bars). (a) 90° of shoulder flexion; (b) 110° of shoulder flexion. Graphs on the left refers to muscle on the left side of the body while graphs on the right refers to muscles on the right side of the body.

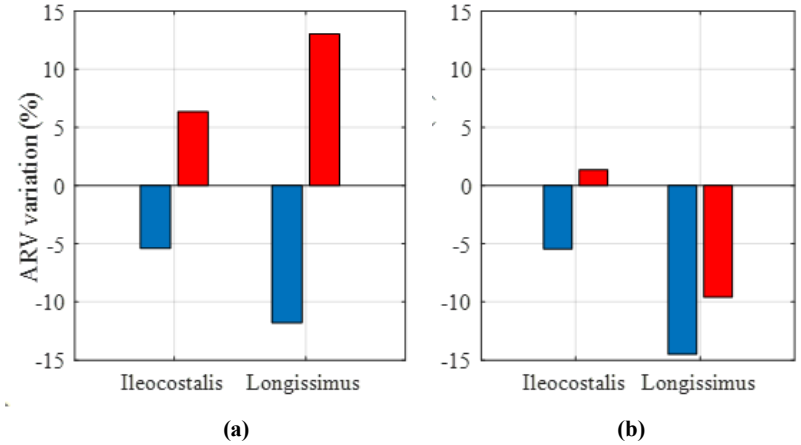

Figure 6.17 Right side lumbar muscles ARV percentage variation between the FREE and EXO dynamic trial of subject 1 (blue bars) and subject 2 (red bars). (a) without hand-tool; (b) with hand-tool.

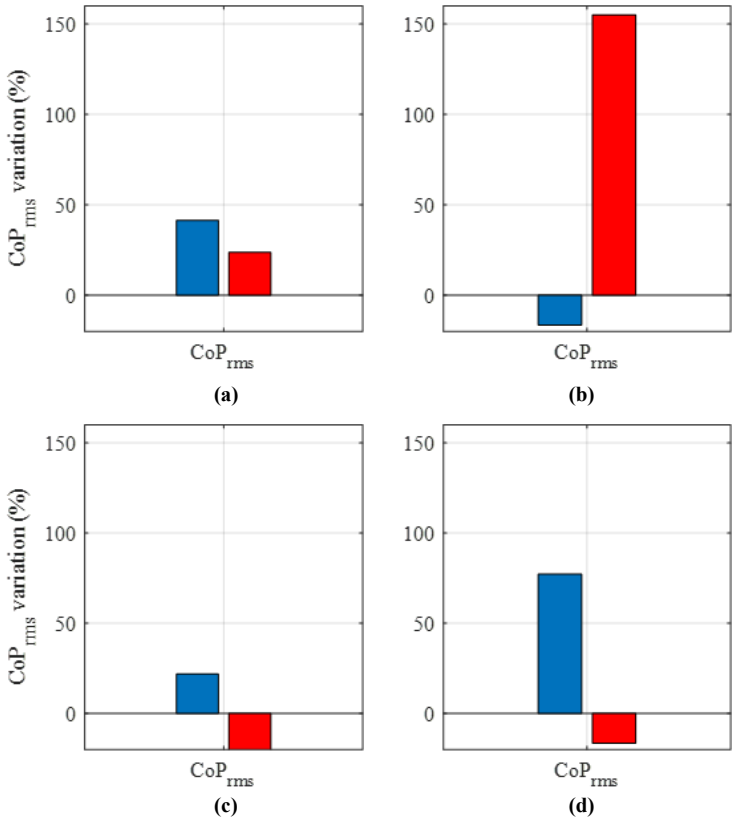

Figure 6.18 CoP_{rms} percentage variation between the FREE and EXO trial of subject 1 (blue bars) and subject 2 (red bars). (a) 90° of shoulder flexion; (b) 110° of shoulder flexion; (c) dynamic task; (d) dynamic test with hand-tool.

6.3.3 Kinematic matching

A misalignment is observed between SJC and the exoskeleton flexion-extension joint in static tasks. The magnitude of the misalignment is shown in Table 6.5 and depends on the shoulder flexion angle.

Table 6.5 SJC – ExoJC misalignment in the arm elevation plane. Positive values indicate forward and upper displacement of SJC with respect ExoJC.

			Antero-posterior mismatch (mm)	Cranio-caudal mismatch (mm)
SBJ 1	Static task: 90°	Right arm	6.7 ± 0.3	-5.8 ± 1.2
		Left arm	3.9 ± 0.6	0.2 ± 1.1
	Static task: 110°	Right arm	-8.6 ± 0.8	-5.5 ± 0.8
		Left arm	-8.4 ± 1.2	-3.1 ± 0.5
SBJ 2	Static task: 90°	Right arm	9.8 ± 0.9	-5.3±0.9
		Left arm	6.1 ± 0.6	-1.4 ± 0.5
	Static task: 110°	Right arm	-5.3 ± 1.2	1.4 ± 1.0
		Left arm	16.1 ± 1.3	-1.9 ± 0.9

6.4 Discussion

In this study, muscle activity, balance performance, and kinematic coupling are quantified to assess the effectiveness of an upper limb passive exoskeleton based on MKM muscles. The results demonstrated the effectiveness of the device during simulated overhead tasks.

During the static tasks, the ARV of the middle deltoid and anterior deltoid has been reduced by about 66% and 55% in the loaded condition (right arm) and by about 64% and 45% in the unloaded condition (left arm). The anterior deltoid percentage reductions are higher than that reported for similar exoskeletons (55% with PAEXO [53]; 20% with MATE [74], and 57% with H-VEX [73]). The middle deltoid also reduces its muscle effort, though by a lesser amount. The lower efficacy could be due to the effect of the exoskeleton on the joint kinematics. The inclination on the frontal plane of the cable between the exoskeleton lower bar and the shoulder pad introduces a parasitic abductor torque on the user's shoulder. As a result, the users change their arm posture to comply with exoskeleton action. Other previous studies also reported an exoskeleton-induced abduction of the arm [23, 53]. However, the middle deltoid is responsible for shoulder horizontal abduction so changing arm posture may require increased medial deltoid muscle activity, reducing the beneficial effect of the exoskeleton for this muscle.

Similarly, during the dynamic tasks, the ARV of the middle deltoid, anterior deltoid, and latissimus dorsi have been reduced respectively by about 20%, 24%, and 5% in the unloaded condition and by about 23%, 47%, and 26% in the loaded condition. Compared to static tests, the anterior deltoid muscle activity reduction is lower. The anterior deltoid is responsible for shoulder flexion and horizontal adduction. Therefore, its muscular effort decreased during the flexion movement thanks to the exoskeleton support torque but increased during the adduction because it must counteract the action of the exoskeleton.

Overall, the exoskeleton seemed to unload the physical demand of the main shoulder elevator muscles in a range that varied from -15% to -77%, depending on the task. Moreover, the muscle activity reduction does not depend on the presence of the tool in the hand. Therefore, the support torque can be adapted to the specific working task by correctly adjusting the initial pressure. Reducing muscle activity has important benefits for the user. Shoulder muscles' contraction generates intra-articular compression forces in the glenohumeral joint which is proportional to the amount of muscle strength developed. Therefore, reducing muscle activity means reducing the loads acting on the joint and consequently the risk of developing degenerative arthritis and tendinitis. Muscle activity reduction also delays the onset of muscle fatigue. The latter affects the movement of bone segments during arm elevation and could lead to the reduction of subacromial space and compression of the supraspinatus tendon.

In view of the above, the presented exoskeleton has the potential to reduce the risk of upper limb work-related musculoskeletal diseases. Despite the experimental test being the first subjects' experience with the exoskeleton, the results are promising. A training session could potentially increase the exoskeleton's effectiveness. In future studies, a training phase should be implemented before the experimental test to allow users to be more comfortable with the exoskeleton. However, further research is needed to confirm the potential long-term benefits.

Upper limb industrial exoskeletons must necessarily be wearable devices. They cannot be connected to fixed platforms because they must allow full freedom of movement to the user. As a result, the support action of the upper limbs occurs at the expense of an increase in load in more stable and stronger body parts such as the spinal joint and pelvis. Despite this force transfer, the effort of the muscles of the lumbar area does not increase significantly, which represents a positive finding considering the added weight of the device on the user. On the other hand, it causes a degradation of the balance performance. In most tasks, there is an increase in CoP_{rms}. However, this side effect could disappear by reducing the overall device weight [53]. A training session to allow the user to adapt to the extra weight could also have a beneficial effect on postural performance.

Finally, SJC – ExoJC misalignment is measured in the arm elevation plane. The misalignment measured in the anteroposterior direction depends on the shoulder flexion angle. As the flexion angle increases, the load on the exoskeleton decreases because both the gravitational force lever arm and the MKM traction force decrease. As a result, the structure, which had deformed as shown in Chapter 4, returns to its undeformed configuration, and the ExoJC moves forward by changing the distance between SJC and ExoJC in the anteroposterior direction. On the other hand, the distance between the two joint centers measured in the craniocaudal direction is not affected by the shoulder flexion angle. SJC and ExoJC move upwards due to the scapular rhythm and the return of the exoskeleton structure in the undeformed condition, respectively.

Despite the misalignment, subjects did not experience discomfort during the experimental tasks. The measured values are acceptable, considering that 11 mm is the maximum relative displacement of a wearable device that will avoid discomfort [121].

6.4.1 Limitations of the experimental trials

The results of this experimental study should be interpreted by considering the following main limitations.

The first concerns the population. The number of subjects involved in the study is limited, and the population is not representative of the end user. A larger sample

size, including experienced manual handling workers, is necessary to ascertain the device's usability for the working population.

The second concerns the task. The experimental tasks were simple and short-lasting. In the future, it is necessary to test the exoskeleton for long-lasting work periods and tasks more representative of the work activities. In addition, dynamic tasks should be repeated at different speeds to ensure that the response time of the MKM is adequate to guarantee an assistive level independent of the speed of movements. Finally, the exoskeleton effect must also be evaluated during peripheral movements, such as lowering the arms, trunk rotation, and walking.

It should be said that the preparation phase of the subject was long and laborious due to the large number of sensors applied to the subject. In the future, the stereophotogrammetric system could be replaced with other equivalent solutions (such as IMU units or motion capture markerless systems) to reduce the duration of experimental testing.

Chapter 7

Conclusion

This work focused on the development of a passive upper-limb exoskeleton for industrial application based on MKM.

Upper limb exoskeletons aim to support the user's arms during the overhead task to reduce the intra-joint compressive load and consequently the incidences of musculoskeletal diseases. Passive exoskeletons currently used in industrial environments employ spring-based mechanisms to balance gravitational forces.

There are various advantages of using MKM as a nonlinear pneumatic spring within the framework of an exoskeleton. The softness and similarity with human skeleton muscles ensure safe contact. In addition, MKMs offer a good power-to-weight ratio and are simple to install, thus they have no negative impact on the weight and overall size of the final design. Furthermore, the availability of MKM in various sizes, as well as the ability to modify the action level by adjusting the supply pressure, allow for broad customization of the actuator's response to suit a wide range of applications and operating situations. Finally, MKMs are inexpensive, resistant to high temperatures and thermal gradients, and can withstand dusty and unclean conditions, making them suited for use in industrial environments.

Analytical and numerical analyses have demonstrated the feasibility of the exoskeleton based on MKMs.

The performance of the exoskeleton strongly depends on the actuator's force transmission to the user's arm. Three different transmissions are compared. In terms of working range, the design option that involves a cam rotating around the shoulder flexion axis turns out to be more convenient. However, it does not allow for effective adaptation of the support action to the working task, since using a hand tool led to a reduction of the support action. Moreover, the cam must be located laterally relative to the shoulder, which calls for the construction of a bulkier, more

complex mechanism. Similar issues arose with the pulley-based configuration. For these reasons, the transmission based on the sliding of a cable on a fixed shoulder pad has been preferred. The results of the simulations presented in Chapter 2, in fact, have shown that a proper design of the shoulder pad profile guarantees an assistive torque equal to at least 75% of the gravitational torque in a working range wide enough for most work activities. In addition, the system performance is not influenced by the loaded conditions. developed to ensure an adequate working range for most work activities.

Defined the transmission and verified the static resistance of the exoskeleton structure through FEM analysis, a prototype that allows a shoulder flexion between 90° and 135° and a shoulder abduction between 0° and 30° is developed. The prototype, made with cheap and easy-to-work materials, has a total weight of about 5 kg.

Experimental validation tests have shown that the exoskeleton can adequately support the user during overhead tasks. A shoulder muscle activity reduction of up to 75% has been detected, while there is no evident increase in lumbar muscle activity due to the transfer of loads by the exoskeleton. Moreover, subjects did not declare discomfort due to excessive pressure applied by the exoskeleton on the user's body.

On the other hand, a worsening of postural performance is observed, witnessed by the CoP_{rms} increase in EXO sessions. This could be due to the prototype weight which is about twice respect to the devices currently on the market. However, the final device will be made with more performing materials, high strength, and low weight (such as carbon fiber) to reduce the overall weight. As a result, the negative effect on CoP displacement could disappear or at least be reduced.

Finally, some critical issues regarding usability are highlighted by experimental tests. The first concerns the power supply of the MKM. The small MKM volume allows to use of a manual pump to quickly pressurize the actuator. However, the user must adjust the supply pressure before wearing the exoskeleton or must be helped by a second operator. In the future, a pneumatic circuit must be designed to allow the user to change the supply pressure and consequently the assistance level of the exoskeleton independently even after wearing the device. Another issue is the limited working range. As shown in Figure 2.14, the support torque provided by the exoskeleton below 80° of shoulder flexion is more than twice the shoulder gravitational torque. The high mismatch between the two torques must be compensated by the muscular action of the user increasing the shoulder extensor muscles' efforts. The transmission should be optimized to facilitate the lowering of the arms.

References

1. European Agency for Safety and Health at Work., IKEI., Panteia. (2019) Work-related musculoskeletal disorders: prevalence, costs and demographics in the EU. Publications Office, LU
2. Grieve JR, Dickerson CR (2008) Overhead work: Identification of evidence-based exposure guidelines. OER 8:53–66. https://doi.org/10.3233/OER-2008-8105
3. Ribeiro J, Lima R, Eckhardt T, Paiva S (2021) Robotic Process Automation and Artificial Intelligence in Industry 4.0 – A Literature review. Procedia Computer Science 181:51–58. https://doi.org/10.1016/j.procs.2021.01.104
4. Ronzoni M, Accorsi R, Botti L, Manzini R (2021) A support-design framework for Cooperative Robots systems in labor-intensive manufacturing processes. Journal of Manufacturing Systems 61:646–657. https://doi.org/10.1016/j.jmsy.2021.10.008
5. Deshpande N, Ortiz J, Sarakoglou I, Semini C, Tsagarakis N, Brygo A, Fernandez J, Frigerio M, Saccares L, Toxiri S, Caldwell DG (2017) NEXT-GENERATION COLLABORATIVE ROBOTIC SYSTEMS FOR INDUSTRIAL SAFETY AND HEALTH. Rome, Italy, pp 187–200
6. Bogue R (2018) Exoskeletons – a review of industrial applications. IR 45:585–590. https://doi.org/10.1108/IR-05-2018-0109
7. Radulovic R, Piera JB, Cassagne B, Grossiord A, Boruchowitsch G (1980) The mobile arm support. Prosthetics & Orthotics International 4:101–105. https://doi.org/10.3109/03093648009164573
8. Makinson BJ (1969) Hardiman I Project. GENERAL ELECTRIC CO SCHENECTADY NY SPECIALTY MATERIALS HANDLING PRODUCTS OPERATION, New York
9. Gopura RARC, Kiguchi K (2009) Mechanical designs of active upper-limb exoskeleton robots: State-of-the-art and design difficulties. In: 2009 IEEE International Conference on Rehabilitation Robotics. IEEE, Kyoto, Japan, pp 178–187
10. Gull MA, Bai S, Bak T (2020) A Review on Design of Upper Limb Exoskeletons. Robotics 9:16. https://doi.org/10.3390/robotics9010016
11. de Vries A, de Looze M (2019) The effect of arm support exoskeletons in realistic work activities: A review study. J Ergonomics 9:255. https://doi.org/doi: 10.35248/2165-7556.19.9.255
12. Huysamen K, Bosch T, De Looze M, Stadler KS, Graf E, O'Sullivan LW (2018) Evaluation of a passive exoskeleton for static upper limb activities. Applied Ergonomics 70:148–155. https://doi.org/10.1016/j.apergo.2018.02.009
13. Kim S, Nussbaum MA, Mokhlespour Esfahani MI, Alemi MM, Alabdulkarim S, Rashedi E (2018) Assessing the influence of a passive, upper extremity exoskeletal vest for tasks requiring arm elevation: Part I –

"Expected" effects on discomfort, shoulder muscle activity, and work task performance. Applied Ergonomics 70:315–322. https://doi.org/10.1016/j.apergo.2018.02.025
14. Theurel J, Desbrosses K, Roux T, Savescu A (2018) Physiological consequences of using an upper limb exoskeleton during manual handling tasks. Applied Ergonomics 67:211–217. https://doi.org/10.1016/j.apergo.2017.10.008
15. Iranzo S, Piedrabuena A, Iordanov D, Martinez-Iranzo U, Belda-Lois J-M (2020) Ergonomics assessment of passive upper-limb exoskeletons in an automotive assembly plant. Applied Ergonomics 87:103120. https://doi.org/10.1016/j.apergo.2020.103120
16. Bai S, Christensen S, Islam MRU (2017) An upper-body exoskeleton with a novel shoulder mechanism for assistive applications. In: 2017 IEEE International Conference on Advanced Intelligent Mechatronics (AIM). IEEE, Munich, Germany, pp 1041–1046
17. Ebrahimi A (2017) Stuttgart Exo-Jacket: An exoskeleton for industrial upper body applications. In: 2017 10th International Conference on Human System Interactions (HSI). IEEE, Ulsan, Korea (South), pp 258–263
18. Mauri A, Lettori J, Fusi G, Fausti D, Mor M, Braghin F, Legnani G, Roveda L (2019) Mechanical and Control Design of an Industrial Exoskeleton for Advanced Human Empowering in Heavy Parts Manipulation Tasks. Robotics 8:65. https://doi.org/10.3390/robotics8030065
19. Otten BM, Weidner R, Argubi-Wollesen A (2018) Evaluation of a Novel Active Exoskeleton for Tasks at or Above Head Level. IEEE Robot Autom Lett 3:2408–2415. https://doi.org/10.1109/LRA.2018.2812905
20. Tokhi MO, Virk GS (2016) Advances in Cooperative Robotics: Proceedings of the 19th International Conference on CLAWAR 2016. WORLD SCIENTIFIC
21. Altenburger R, Scherly D, Stadler KS (2016) Design of a passive, iso-elastic upper limb exoskeleton for gravity compensation. Robomech J 3:12. https://doi.org/10.1186/s40648-016-0051-5
22. Maurice P, Camernik J, Gorjan D, Schirrmeister B, Bornmann J, Tagliapietra L, Latella C, Pucci D, Fritzsche L, Ivaldi S, Babic J (2020) Objective and Subjective Effects of a Passive Exoskeleton on Overhead Work. IEEE Trans Neural Syst Rehabil Eng 28:152–164. https://doi.org/10.1109/TNSRE.2019.2945368
23. Spada S, Ghibaudo L, Gilotta S, Gastaldi L, Cavatorta MP (2017) Investigation into the Applicability of a Passive Upper-limb Exoskeleton in Automotive Industry. Procedia Manufacturing 11:1255–1262. https://doi.org/10.1016/j.promfg.2017.07.252
24. Wang H-M, Le DKL, Lin W-C (2021) Evaluation of a Passive Upper-Limb Exoskeleton Applied to Assist Farming Activities in Fruit Orchards. Applied Sciences 11:757. https://doi.org/10.3390/app11020757
25. De Vries A, Murphy M, Könemann R, Kingma I, De Looze M (2019) The Amount of Support Provided by a Passive Arm Support Exoskeleton in a Range of Elevated Arm Postures. IISE Transactions on Occupational

Ergonomics and Human Factors 7:311–321. https://doi.org/10.1080/24725838.2019.1669736
26. Li J, Zhang C, Dong M, Cao Q (2020) A Kinematic Model of the Shoulder Complex Obtained from a Wearable Detection System. Applied Sciences 10:3696. https://doi.org/10.3390/app10113696
27. Hall SJ (2012) Basic biomechanics, 6th ed. McGraw-Hill, New York, NY
28. Delgado P, Alekhya S, Majidirad A, Hakansson NA, Desai J, Yihun Y (2020) Shoulder Kinematics Assessment towards Exoskeleton Development. Applied Sciences 10:6336. https://doi.org/10.3390/app10186336
29. Zhang C, Dong M, Li J, Cao Q (2020) A Modified Kinematic Model of Shoulder Complex Based on Vicon Motion Capturing System: Generalized GH Joint with Floating Centre. Sensors 20:3713. https://doi.org/10.3390/s20133713
30. Klopčar N, Lenarčič J (2006) Bilateral and unilateral shoulder girdle kinematics during humeral elevation. Clinical Biomechanics 21:S20–S26. https://doi.org/10.1016/j.clinbiomech.2005.09.009
31. Amabile C, Bull AMJ, Kedgley AE (2016) The centre of rotation of the shoulder complex and the effect of normalisation. Journal of Biomechanics 49:1938–1943. https://doi.org/10.1016/j.jbiomech.2016.03.035
32. Nef T, Riener R (2008) Shoulder actuation mechanisms for arm rehabilitation exoskeletons. In: 2008 2nd IEEE RAS & EMBS International Conference on Biomedical Robotics and Biomechatronics. IEEE, Scottsdale, AZ, USA, pp 862–868
33. Sylla N, Bonnet V, Colledani F, Fraisse P (2014) Ergonomic contribution of ABLE exoskeleton in automotive industry. International Journal of Industrial Ergonomics 44:475–481. https://doi.org/10.1016/j.ergon.2014.03.008
34. Winter DA (2009) Biomechanics and motor control of human movement, 4th ed. Wiley, Hoboken, N.J
35. Stekelenburg A, Strijkers GJ, Parusel H, Bader DL, Nicolay K, Oomens CW (2007) Role of ischemia and deformation in the onset of compression-induced deep tissue injury: MRI-based studies in a rat model. Journal of Applied Physiology 102:2002–2011. https://doi.org/10.1152/japplphysiol.01115.2006
36. Gefen A, Brienza DM, Cuddigan J, Haesler E, Kottner J (2022) Our contemporary understanding of the aetiology of pressure ulcers/pressure injuries. International Wound Journal 19:692–704. https://doi.org/10.1111/iwj.13667
37. Kozinc Ž, Babič J, Šarabon N (2021) Human pressure tolerance and effects of different padding materials with implications for development of exoskeletons and similar devices. Applied Ergonomics 93:103379. https://doi.org/10.1016/j.apergo.2021.103379
38. Hven L, Frost P, Bonde JPE (2017) Evaluation of Pressure Pain Threshold as a Measure of Perceived Stress and High Job Strain. PLoS ONE 12:e0167257. https://doi.org/10.1371/journal.pone.0167257
39. Pons JL (2008) Wearable robots: biomechatronic exoskeletons. Wiley, Hoboken, N.J

40. Kermavnar T, Power V, De Eyto A, O'Sullivan LW (2018) Computerized Cuff Pressure Algometry as Guidance for Circumferential Tissue Compression for Wearable Soft Robotic Applications: A Systematic Review. Soft Robotics 5:1–16. https://doi.org/10.1089/soro.2017.0046
41. Yandell MB, Ziemnicki DM, McDonald KA, Zelik KE (2020) Characterizing the comfort limits of forces applied to the shoulders, thigh and shank to inform exosuit design. PLoS ONE 15:e0228536. https://doi.org/10.1371/journal.pone.0228536
42. He Y, Eguren D, Luu TP, Contreras-Vidal JL (2017) Risk management and regulations for lower limb medical exoskeletons: a review. MDER Volume 10:89–107. https://doi.org/10.2147/MDER.S107134
43. Graven-Nielsen T, Vaegter HB, Finocchietti S, Handberg G, Arendt-Nielsen L (2015) Assessment of musculoskeletal pain sensitivity and temporal summation by cuff pressure algometry: a reliability study. Pain 156:2193–2202. https://doi.org/10.1097/j.pain.0000000000000294
44. Cui X, Chen W, Jin X, Agrawal SK (2017) Design of a 7-DOF Cable-Driven Arm Exoskeleton (CAREX-7) and a Controller for Dexterous Motion Training or Assistance. IEEE/ASME Trans Mechatron 22:161–172. https://doi.org/10.1109/TMECH.2016.2618888
45. Dehez B, Sapin J (2011) ShouldeRO, an alignment-free two-DOF rehabilitation robot for the shoulder complex. In: 2011 IEEE International Conference on Rehabilitation Robotics. IEEE, Zurich, pp 1–8
46. Lo HS, Xie SQ (2012) Exoskeleton robots for upper-limb rehabilitation: State of the art and future prospects. Medical Engineering & Physics 34:261–268. https://doi.org/10.1016/j.medengphy.2011.10.004
47. Park H-S, Yupeng Ren, Li-Qun Zhang (2008) IntelliArm: An exoskeleton for diagnosis and treatment of patients with neurological impairments. In: 2008 2nd IEEE RAS & EMBS International Conference on Biomedical Robotics and Biomechatronics. IEEE, Scottsdale, AZ, USA, pp 109–114
48. Schiele A, Van Der Helm FCT (2006) Kinematic Design to Improve Ergonomics in Human Machine Interaction. IEEE Trans Neural Syst Rehabil Eng 14:456–469. https://doi.org/10.1109/TNSRE.2006.881565
49. Flor-Unda O, Casa B, Fuentes M, Solorzano S, Narvaez-Espinoza F, Acosta-Vargas P (2023) Exoskeletons: Contribution to Occupational Health and Safety. Bioengineering 10:1039. https://doi.org/10.3390/bioengineering10091039
50. Rashedi E, Kim S, Nussbaum MA, Agnew MJ (2014) Ergonomic evaluation of a wearable assistive device for overhead work. Ergonomics 57:1864–1874. https://doi.org/10.1080/00140139.2014.952682
51. Kim S, Nussbaum MA, Mokhlespour Esfahani MI, Alemi MM, Jia B, Rashedi E (2018) Assessing the influence of a passive, upper extremity exoskeletal vest for tasks requiring arm elevation: Part II – "Unexpected" effects on shoulder motion, balance, and spine loading. Applied Ergonomics 70:323–330. https://doi.org/10.1016/j.apergo.2018.02.024
52. Weston EB, Alizadeh M, Knapik GG, Wang X, Marras WS (2018) Biomechanical evaluation of exoskeleton use on loading of the lumbar spine.

Applied Ergonomics 68:101–108. https://doi.org/10.1016/j.apergo.2017.11.006
53. Maurice P, Čamernik J, Gorjan D, Schirrmeister B, Bornmann J, Tagliapietra L, Latella C, Pucci D, Fritzsche L, Ivaldi S, Babič J (2019) Evaluation of PAEXO, a novel passive exoskeleton for overhead work. Computer Methods in Biomechanics and Biomedical Engineering 22:S448–S450. https://doi.org/10.1080/10255842.2020.1714977
54. Ebrahimi A, Groninger D, Singer R, Schneider U (2017) Control parameter optimization of the actively powered upper body exoskeleton using subjective feedbacks. In: 2017 3rd International Conference on Control, Automation and Robotics (ICCAR). IEEE, Nagoya, Japan, pp 432–437
55. Jarrett C, McDaid AJ (2017) Robust Control of a Cable-Driven Soft Exoskeleton Joint for Intrinsic Human-Robot Interaction. IEEE Trans Neural Syst Rehabil Eng 25:976–986. https://doi.org/10.1109/TNSRE.2017.2676765
56. Du Z, Yan Z, Huang T, Bai O, Huang Q, Zhang T, Han B (2022) Development and Experimental Validation of a Passive Exoskeletal Vest. IEEE Trans Neural Syst Rehabil Eng 30:1941–1950. https://doi.org/10.1109/TNSRE.2022.3189666
57. De La Tejera JA, Bustamante-Bello R, Ramirez-Mendoza RA, Izquierdo-Reyes J (2020) Systematic Review of Exoskeletons towards a General Categorization Model Proposal. Applied Sciences 11:76. https://doi.org/10.3390/app11010076
58. Voilque A, Masood J, Fauroux Jc, Sabourin L, Guezet O (2019) Industrial Exoskeleton Technology: Classification, Structural Analysis, and Structural Complexity Indicator. In: 2019 Wearable Robotics Association Conference (WearRAcon). IEEE, Scottsdale, AZ, USA, pp 13–20
59. Bilancia P, Berselli G (2021) Conceptual design and virtual prototyping of a wearable upper limb exoskeleton for assisted operations. Int J Interact Des Manuf 15:525–539. https://doi.org/10.1007/s12008-021-00779-9
60. Kosaki T, Li S, Department of Systems Engineering, Graduate School of Information Sciences, Hiroshima City University 3-4-1 Ozuka-higashi, Asaminami-ku, Hiroshima 731-3194, Japan (2020) A Water-Hydraulic Upper-Limb Assistive Exoskeleton System with Displacement Estimation. JRM 32:149–156. https://doi.org/10.20965/jrm.2020.p0149
61. Holl E (2022) New Optimized Mechanism for Linking a Hydraulic Actuator to the Elbow Joint of an Upper Arm Exoskeleton. J Test Eval 50:20210677. https://doi.org/10.1520/JTE20210677
62. Gunasekara JMP, Gopura RARC, Jayawardane TSS, Lalitharathne SWHMTD (2012) Control methodologies for upper limb exoskeleton robots. In: 2012 IEEE/SICE International Symposium on System Integration (SII). IEEE, Fukuoka, Japan, pp 19–24
63. Sun J, Shen Y, Rosen J (2021) Sensor Reduction, Estimation, and Control of an Upper-Limb Exoskeleton. IEEE Robot Autom Lett 6:1012–1019. https://doi.org/10.1109/LRA.2021.3056366

64. Anam K, Al-Jumaily AA (2012) Active Exoskeleton Control Systems: State of the Art. Procedia Engineering 41:988–994. https://doi.org/10.1016/j.proeng.2012.07.273
65. Liu C, Liang H, Ueda N, Li P, Fujimoto Y, Zhu C (2020) Functional Evaluation of a Force Sensor-Controlled Upper-Limb Power-Assisted Exoskeleton with High Backdrivability. Sensors 20:6379. https://doi.org/10.3390/s20216379
66. Hessinger M, Pingsmann M, Perry JC, Werthschutzky R, Kupnik M (2017) Hybrid position/force control of an upper-limb exoskeleton for assisted drilling. In: 2017 IEEE/RSJ International Conference on Intelligent Robots and Systems (IROS). IEEE, Vancouver, BC, pp 1824–1829
67. Fu J, Choudhury R, Hosseini SM, Simpson R, Park J-H (2022) Myoelectric Control Systems for Upper Limb Wearable Robotic Exoskeletons and Exosuits—A Systematic Review. Sensors 22:8134. https://doi.org/10.3390/s22218134
68. Trigili E, Grazi L, Crea S, Accogli A, Carpaneto J, Micera S, Vitiello N, Panarese A (2019) Detection of movement onset using EMG signals for upper-limb exoskeletons in reaching tasks. J NeuroEngineering Rehabil 16:45. https://doi.org/10.1186/s12984-019-0512-1
69. Treussart B, Geffard F, Vignais N, Marin F (2020) Controlling an upper-limb exoskeleton by EMG signal while carrying unknown load. In: 2020 IEEE International Conference on Robotics and Automation (ICRA). IEEE, Paris, France, pp 9107–9113
70. Yang C-J, Zhang J-F, Chen Y, Dong Y-M, Zhang Y (2008) A Review of exoskeleton-type systems and their key technologies. Proceedings of the Institution of Mechanical Engineers, Part C: Journal of Mechanical Engineering Science 222:1599–1612. https://doi.org/10.1243/09544062JMES936
71. Herr H (2009) Exoskeletons and orthoses: classification, design challenges and future directions. J NeuroEngineering Rehabil 6:21. https://doi.org/10.1186/1743-0003-6-21
72. De Looze MP, Bosch T, Krause F, Stadler KS, O'Sullivan LW (2016) Exoskeletons for industrial application and their potential effects on physical work load. Ergonomics 59:671–681. https://doi.org/10.1080/00140139.2015.1081988
73. Hyun DJ, Bae K, Kim K, Nam S, Lee D (2019) A light-weight passive upper arm assistive exoskeleton based on multi-linkage spring-energy dissipation mechanism for overhead tasks. Robotics and Autonomous Systems 122:103309. https://doi.org/10.1016/j.robot.2019.103309
74. Pacifico I, Scano A, Guanziroli E, Moise M, Morelli L, Chiavenna A, Romo D, Spada S, Colombina G, Molteni F, Giovacchini F, Vitiello N, Crea S (2020) An Experimental Evaluation of the Proto-MATE: A Novel Ergonomic Upper-Limb Exoskeleton to Reduce Workers' Physical Strain. IEEE Robot Automat Mag 27:54–65. https://doi.org/10.1109/MRA.2019.2954105
75. Magnetti Gisolo S, Muscolo GG, Paterna M, De Benedictis C, Ferraresi C (2021) Feasibility Study of a Passive Pneumatic Exoskeleton for Upper

Limbs Based on a McKibben Artificial Muscle. In: Zeghloul S, Laribi MA, Sandoval J (eds) Advances in Service and Industrial Robotics. Springer International Publishing, Cham, pp 208–217
76. Paterna M, Magnetti Gisolo S, De Benedictis C, Muscolo GG, Ferraresi C (2022) A passive upper-limb exoskeleton for industrial application based on pneumatic artificial muscles. Mech Sci 13:387–398. https://doi.org/10.5194/ms-13-387-2022
77. Cacucciolo V, Renda F, Poccia E, Laschi C, Cianchetti M (2016) Modelling the nonlinear response of fibre-reinforced bending fluidic actuators. Smart Mater Struct 25:105020. https://doi.org/10.1088/0964-1726/25/10/105020
78. Ferraresi C, Franco W, Bertetto AM, Department of Mechanics, Politecnico di Torino, Corso Duca degli Abruzzi, 24 -10129 Torino - Italy, Department of Mechanical Engineering, University of Cagliari Piazza d'Armi, 09123 Cagliari-Italy (2001) Flexible Pneumatic Actuators: A Comparison between The McKibben and the Straight Fibres Muscles. J Robot Mechatron 13:56–63. https://doi.org/10.20965/jrm.2001.p0056
79. Belforte G, Eula G, Ivanov A, Sirolli S (2014) Soft Pneumatic Actuators for Rehabilitation. Actuators 3:84–106. https://doi.org/10.3390/act3020084
80. Ferraresi C, Manuello Bertetto A, Costamagna A, Gollè D (2003) Integrated fin-actuator systems for a marine robot. In: Proceedings of RAAD'03. Cassino
81. Manuello Bertetto A, Cadeddu A, Besalduch LA, Ricciu R, Ferraresi C (2016) Energy balance and mechanical behaviour of a flexible pneumatic actuator for fish-like propulsion. International Journal of Mechanics and Control 17:23–30
82. Kojima A, Okui M, Nakamura T (2020) Development of Soft Pneumatic Actuators Using High-Strain Elastic Materials with Stress Anisotropy of Short Fibers. In: The 1st International Electronic Conference on Actuator Technology: Materials, Devices and Applications. MDPI, p 41
83. Hu W, Mutlu R, Li W, Alici G (2018) A Structural Optimisation Method for a Soft Pneumatic Actuator. Robotics 7:24. https://doi.org/10.3390/robotics7020024
84. Guo L, Li K, Cheng G, Zhang Z, Xu C, Ding J (2021) Design and Experiments of Pneumatic Soft Actuators. Robotica 39:1806–1815. https://doi.org/10.1017/S0263574720001514
85. Ermini L, Chiarello NE, De Benedictis C, Ferraresi C, Roatta S (2021) Venous Pulse Wave Velocity variation in response to a simulated fluid challenge in healthy subjects. Biomedical Signal Processing and Control 63:102177. https://doi.org/10.1016/j.bspc.2020.102177
86. Bertetto AM, Meili S, Ferraresi C, Maffiodo D, Crisafulli A, Concu A, Laboratory of Applied Mechanics and Robotics, Department of Mechanical, Chemical and Materials Engineering, University of Cagliari, Group of Automation and Robotics, Department of Mechanical and Aerospace Engineering, Politecnico di Torino, Torino, Italy, Laboratory of Sports Physiology, Department of Medical Sciences, University of Cagliari, Cagliari, Italy, 2C Technologies Inc., Spinoff of University of Cagliari, Cagliari, Italy (2017) A Mechatronic Pneumatic Device to Improve Diastolic

Function by Intermittent Action on Lower Limbs. Int J Automation Technol 11:501–508. https://doi.org/10.20965/ijat.2017.p0501
87. De Falco I, Cianchetti M, Menciassi A (2017) A soft multi-module manipulator with variable stiffness for minimally invasive surgery. Bioinspir Biomim 12:056008. https://doi.org/10.1088/1748-3190/aa7ccd
88. Franco W, Maffiodo D, De Benedictis C, Ferraresi C (2019) Dynamic Modeling and Experimental Validation of a Haptic Finger Based on a McKibben Muscle. In: Gasparetto A, Ceccarelli M (eds) Mechanism Design for Robotics. Springer International Publishing, Cham, pp 251–259
89. Ranzani T, Cianchetti M, Gerboni G, Falco ID, Menciassi A (2016) A Soft Modular Manipulator for Minimally Invasive Surgery: Design and Characterization of a Single Module. IEEE Trans Robot 32:187–200. https://doi.org/10.1109/TRO.2015.2507160
90. Antonelli MG, Beomonte Zobel P, Durante F, Gaj F (2017) Development and testing of a grasper for NOTES powered by variable stiffness pneumatic actuation. Int J Med Robotics Comput Assist Surg 13:e1796. https://doi.org/10.1002/rcs.1796
91. Antonelli MG, Beomonte Zobel P, Raimondi P, Raparelli T, Costanzo G (2010) An Innovative Brace with Pneumatic Thrusts for Scoliosis Treatment. Int J DNE 5:354–367. https://doi.org/10.2495/DNE-V5-N4-354-367
92. Belforte G, Eula G, Ivanov A, Raparelli T, Sirolli S (2018) Presentation of textile pneumatic muscle prototypes applied in an upper limb active suit experimental model. The Journal of The Textile Institute 109:757–766. https://doi.org/10.1080/00405000.2017.1368111
93. Carello M, Ferraresi C, Visconte C (2003) A new flexible pneumatic finger for a fruit-harvesting hand. Sorrento
94. Antonelli MG, Beomonte Zobel P, D'Ambrogio W, Durante F (2020) Design Methodology for a Novel Bending Pneumatic Soft Actuator for Kinematically Mirroring the Shape of Objects. Actuators 9:113. https://doi.org/10.3390/act9040113
95. Paterna M, De Benedictis C, Ferraresi C (2022) The Research on Soft Pneumatic Actuators in Italy: Design Solutions and Applications. Actuators 11:328. https://doi.org/10.3390/act11110328
96. Belforte G, Raparelli T, Sirolli SA, Department of Mechanical and Aerospace Engineering, Politecnico di Torino (2017) A Novel Geometric Formula for Predicting Contractile Force in McKibben Pneumatic Muscles. Int J Automation Technol 11:368–377. https://doi.org/10.20965/ijat.2017.p0368
97. Antonelli MG, Zobel PB, D'Ambrogio W, Durante F (2018) An analytical formula for designing McKibben pneumatic muscles. International Journal of Mechanical Engineering and Technology 9:320–337
98. Piteľ J, Tóthová M (2016) Modelling of pneumatic muscle actuator using Hill's model with different approximations of static characteristics of artificial muscle. MATEC Web Conf 76:02015. https://doi.org/10.1051/matecconf/20167602015

99. Tsagarakis NG, Caldwell DG (2003) Development and Control of a 'Soft-Actuated' Exoskeleton for Use in Physiotherapy and Training. Autonomous Robots 15:21–33. https://doi.org/10.1023/A:1024484615192
100. Klein J, Spencer SJ, Allington J, Minakata K, Wolbrecht ET, Smith R, Bobrow JE, Reinkensmeyer DJ (2008) Biomimetic orthosis for the neurorehabilitation of the elbow and shoulder (BONES). In: 2008 2nd IEEE RAS & EMBS International Conference on Biomedical Robotics and Biomechatronics. IEEE, Scottsdale, AZ, USA, pp 535–541
101. Balasubramanian S, Ruihua Wei, Perez M, Shepard B, Koeneman E, Koeneman J, Jiping He (2008) RUPERT: An exoskeleton robot for assisting rehabilitation of arm functions. In: 2008 Virtual Rehabilitation. IEEE, Vancouver, BC, pp 163–167
102. Pardoel S, Doumit M (2019) Development and testing of a passive ankle exoskeleton. Biocybernetics and Biomedical Engineering 39:902–913. https://doi.org/10.1016/j.bbe.2019.08.007
103. Krogh-Lund C, Jorgensen K (1991) Changes in conduction velocity, median frequency, and root mean square-amplitude of the electromyogram during 25% maximal voluntary contraction of the triceps brachii muscle, to limit of endurance. Europ J Appl Physiol 63:60–69. https://doi.org/10.1007/BF00760803
104. Paterna M, Dvir Z, De Benedictis C, Maffiodo D, Franco W, Ferraresi C, Roatta S (2022) Center of pressure displacement due to graded controlled perturbations to the trunk in standing subjects: the force–impulse paradigm. Eur J Appl Physiol 122:425–435. https://doi.org/10.1007/s00421-021-04844-9
105. Dvir Z, Paterna M, Quargnenti M, De Benedictis C, Maffiodo D, Franco W, Ferraresi C, Manca A, Deriu F, Roatta S (2020) Linearity and repeatability of postural responses in relation to peak force and impulse of manually delivered perturbations: a preliminary study. Eur J Appl Physiol 120:1319–1330. https://doi.org/10.1007/s00421-020-04364-y
106. Doyle RJ, Hsiao-Wecksler ET, Ragan BG, Rosengren KS (2007) Generalizability of center of pressure measures of quiet standing. Gait & Posture 25:166–171. https://doi.org/10.1016/j.gaitpost.2006.03.004
107. Palmieri RM, Ingersoll CD, Stone MB, Krause BA (2002) Center-of-Pressure Parameters Used in the Assessment of Postural Control. Journal of Sport Rehabilitation 11:51–66. https://doi.org/10.1123/jsr.11.1.51
108. Prieto TE, Myklebust JB, Hoffmann RG, Lovett EG, Myklebust BM (1996) Measures of postural steadiness: differences between healthy young and elderly adults. IEEE Trans Biomed Eng 43:956–966. https://doi.org/10.1109/10.532130
109. Bosch T, Van Eck J, Knitel K, De Looze M (2016) The effects of a passive exoskeleton on muscle activity, discomfort and endurance time in forward bending work. Applied Ergonomics 54:212–217. https://doi.org/10.1016/j.apergo.2015.12.003
110. De Leva P (1996) Adjustments to Zatsiorsky-Seluyanov's segment inertia parameters. Journal of Biomechanics 29:1223–1230. https://doi.org/10.1016/0021-9290(95)00178-6

111. Sosa-Vivas L, Gonzalez-Delgado J, Torrente-Prato G (2023) Experimental and numerical study of orthotropic behavior of 3D printed polylactic acid by material extrusion. Prog Addit Manuf 8:947–959. https://doi.org/10.1007/s40964-022-00369-5
112. Dai S, Deng ZC, Yu YJ, Zhang K, Wang SH, Ye J (2020) Orthotropic elastic behaviors and yield strength of fused deposition modeling materials: Theory and experiments. Polymer Testing 87:106520. https://doi.org/10.1016/j.polymertesting.2020.106520
113. Ahn S, Montero M, Odell D, Roundy S, Wright PK (2002) Anisotropic material properties of fused deposition modeling ABS. Rapid Prototyping Journal 8:248–257. https://doi.org/10.1108/13552540210441166
114. Yao T, Deng Z, Zhang K, Li S (2019) A method to predict the ultimate tensile strength of 3D printing polylactic acid (PLA) materials with different printing orientations. Composites Part B: Engineering 163:393–402. https://doi.org/10.1016/j.compositesb.2019.01.025
115. Azzi VD, Tsai SW (1965) Anisotropic strength of composites: Investigation aimed at developing a theory applicable to laminated as well as unidirectional composites, employing simple material properties derived from unidirectional specimens alone. Experimental Mechanics 5:283–288. https://doi.org/10.1007/BF02326292
116. Alaimo G, Marconi S, Costato L, Auricchio F (2017) Influence of meso-structure and chemical composition on FDM 3D-printed parts. Composites Part B: Engineering 113:371–380. https://doi.org/10.1016/j.compositesb.2017.01.019
117. Zou R, Xia Y, Liu S, Hu P, Hou W, Hu Q, Shan C (2016) Isotropic and anisotropic elasticity and yielding of 3D printed material. Composites Part B: Engineering 99:506–513. https://doi.org/10.1016/j.compositesb.2016.06.009
118. Xia Y, Xu K, Zheng G, Zou R, Li B, Hu P (2019) Investigation on the elasto-plastic constitutive equation of parts fabricated by fused deposition modeling. RPJ 25:592–601. https://doi.org/10.1108/RPJ-06-2018-0147
119. Liebig WV, Jackstadt A, Sessner V, Weidenmann KA, Kärger L (2019) Frequency domain modelling of transversely isotropic viscoelastic fibre-reinforced plastics. Composites Science and Technology 180:101–110. https://doi.org/10.1016/j.compscitech.2019.04.019
120. Novák D, Tulu B, Brendryen H (2016) Handbook of Research on Holistic Perspectives in Gamification for Clinical Practice: IGI Global
121. Mahmud J, Holt CA, Evans SL (2010) An innovative application of a small-scale motion analysis technique to quantify human skin deformation in vivo. Journal of Biomechanics 43:1002–1006. https://doi.org/10.1016/j.jbiomech.2009.11.009

Appendix A: markers trajectories post-processing algorithm

```
clear variables
close all
clc

%% Constant Parameters

[file,path] = uigetfile('*.xlsx');
file = [path file];
Parameters = readmatrix(file,'Sheet','Parameters','Range','B2:C4');

MarkerDiameter = 14;

RShoulderOffset = Parameters(1,1) + (MarkerDiameter/2);
RElbowOffset = (Parameters(2,1) + MarkerDiameter)/2;
RWristOffset = (Parameters(3,1) + MarkerDiameter)/2;

LShoulderOffset = Parameters(1,2) + (MarkerDiameter/2);
LElbowOffset = (Parameters(2,2) + MarkerDiameter)/2;
LWristOffset = (Parameters(3,2) + MarkerDiameter)/2;

%% Marker Trajectories
Trajectories = readmatrix(file,'Sheet','Trajectories');
Trajectories(1:3,:)= [];

T10 = Trajectories(:,3:5);
C7 = Trajectories(:,6:8);
STRN = Trajectories(:,9:11);
CLAV = Trajectories(:,12:14);
RSHO = Trajectories(:,15:17);
RELB = Trajectories(:,18:20);
RWRB = Trajectories(:,27:29);
RWRA = Trajectories(:,30:32);
LSHO = Trajectories(:,36:38);
LELB = Trajectories(:,39:41);
LWRB = Trajectories(:,48:50);
LWRA = Trajectories(:,51:53);

fs = 100;
t = 0:(1/fs):(length(T10)-1)/fs;

%% Identify and reconstruct any missing coordinates of C7

n=4;
fc = 6;
[b,a]=butter(n,fc/(fs/2));
```

```
T10 = filtfilt(b,a,T10);
STRN = filtfilt(b,a,STRN);
CLAV = filtfilt(b,a,CLAV);
load([path 'C7_delta.mat']);

for i = 1:length(C7)
    if anynan(C7(i,:)) == 1
       C7(i,:) = markerrec(STRN(i,:),CLAV(i,:),T10(i,:),C7_delta);
    end
end

C7 = filtfilt(b,a,C7);

%% Thorax Origin
%Thorax
ZAxis = ((C7 + CLAV)./2) - ((T10 + STRN)./2);
XAxis = ((T10 + C7)./2)-((STRN + CLAV)./2);
YAxis = cross(ZAxis,XAxis);
XAxis = cross(YAxis,ZAxis);
XAxis = XAxis./((sum((XAxis.^2),2)).^0.5);
ThoraxOrigin = NaN(length(XAxis),3);
for i = 1:length(XAxis)
    tmp = XAxis(i,:)'*(MarkerDiameter/2);
    ThoraxOrigin(i,:) = CLAV(i,:) + tmp';
end
ThoraxFront = - XAxis;
ThoraxBack = XAxis;
ThoraxLeft = -YAxis;
ThoraxRight = YAxis;

%% Identify and reconstruct any missing coordinates of RSHO and LSHO

%RSHO
if anynan(RSHO) == 1
    RCLA = Trajectories(:,21:23);
    load([path 'RSHO_delta.mat']);
end

for i = 1:length(RSHO)
    if anynan(RSHO(i,:)) == 1
       RSHO(i,:) =
markerrec(ThoraxOrigin(i,:),CLAV(i,:),RCLA(i,:),RSHO_delta);
    end
end
RSHO = filtfilt(b,a,RSHO);

%LSHO
if anynan(LSHO) == 1
    LCLA = Trajectories(:,42:44);
    load([path 'LSHO_delta.mat']);
end
for i = 1:length(LSHO)
    if anynan(LSHO(i,:)) == 1
       LSHO(i,:) =
markerrec(ThoraxOrigin(i,:),CLAV(i,:),LCLA(i,:),LSHO_delta);
    end
```

```
end
LSHO = filtfilt(b,a,LSHO);

%% SJC

% Right arm
ClavicleY = cross(XAxis,ThoraxOrigin - RSHO);
RSJC = Chord(RSHO,ThoraxOrigin,RSHO-ClavicleY,RShoulderOffset);

% Left arm
ClavicleY = cross(XAxis,ThoraxOrigin - LSHO);
LSJC = Chord(LSHO,ThoraxOrigin,LSHO+ClavicleY,LShoulderOffset);

%% Identify and reconstruct any missing coordinates of RELB and LELB

RWRB = filtfilt(b,a,RWRB);
RWRA = filtfilt(b,a,RWRA);

%RELB
if anynan(RELB) == 1
    RELBM = Trajectories(:,24:26);
    load([path 'RELB_delta.mat']);
end
for i = 1:length(RELB)
    if anynan(RELB(i,:)) == 1
       RELB(i,:) = markerrec(RWRB(i,:),RELBM(i,:),RSHO(i,:),RELB_delta);
    end
end
RELB = filtfilt(b,a,RELB);

LWRB = filtfilt(b,a,LWRB);
LWRA = filtfilt(b,a,LWRA);

%LELB
if anynan(LELB) == 1
    LELBM = Trajectories(:,45:47);
    load([path 'LELB_delta.mat']);
end
for i = 1:length(LELB)
    if anynan(LELB(i,:)) == 1
       LELB(i,:) = markerrec(LWRB(i,:),LELBM(i,:),LSHO(i,:),LELB_delta);
    end
end
LELB = filtfilt(b,a,LELB);

%% EJC

%Right arm
RWristMarker = (RWRB+RWRA)./2;
ConstructZ = RSJC - RELB;
ConstructX = RELB - RWristMarker;

Z = cross(ConstructZ,ConstructX);
Y = cross(Z,ConstructZ);
Col0 = ConstructZ./((sum((ConstructZ.^2),2)).^0.5);
Col1 = Y./((sum((Y.^2),2)).^0.5);
```

```
Col2 = Z./((sum((Z.^2),2)).^0.5);
VirtualArmWand = NaN(length(Y),3);
for i = 1:length(Y)
    Rot = [Col1(i,:)' Col2(i,:)' Col0(i,:)'];
    tmp = Rot*[0; 500; 0];
    VirtualArmWand(i,:) = tmp' + RELB(i,:);
end
REJC = Chord(RELB,RSJC,VirtualArmWand,RElbowOffset);

%Left arm
LWristMarker = (LWRB+LWRA)./2;
ConstructZ = LSJC - LELB;
ConstructX = LELB - LWristMarker;

Z = cross(ConstructZ,ConstructX);
Y = cross(Z,ConstructZ);
Col0 = ConstructZ./((sum((ConstructZ.^2),2)).^0.5);
Col1 = Y./((sum((Y.^2),2)).^0.5);
Col2 = Z./((sum((Z.^2),2)).^0.5);
VirtualArmWand = NaN(length(Y),3);
for i = 1:length(Y)
    Rot = [Col1(i,:)' Col2(i,:)' Col0(i,:)'];
    tmp = Rot*[0; -500; 0];
    VirtualArmWand(i,:) = tmp' + LELB(i,:);
end
LEJC = Chord(LELB,LSJC,VirtualArmWand,LElbowOffset);

%% WJC

% Right arm
ThicknessDir = cross( RWRA-RWRB, RWristMarker-REJC );
ThicknessDir = ThicknessDir./((sum((ThicknessDir.^2),2)).^0.5);
RWJC = NaN(length(ThicknessDir),3);
for i = 1:length(ThicknessDir)
    tmp = ThicknessDir(i,:)'*RWristOffset;
    RWJC(i,:) = RWristMarker(i,:) + tmp';
end

% Left arm
ThicknessDir = cross( LWRA-LWRB, LEJC-LWristMarker );
ThicknessDir = ThicknessDir./((sum((ThicknessDir.^2),2)).^0.5);
LWJC = NaN(length(ThicknessDir),3);
for i = 1:length(ThicknessDir)
    tmp = ThicknessDir(i,:)'*LWristOffset;
    LWJC(i,:) = LWristMarker(i,:) + tmp';
end

%% arm and forearm local reference systems

% Right arm
RHumerusAxis = RSJC - REJC;
RRadiusAxis = REJC - RWJC;

Z = cross(RHumerusAxis,RRadiusAxis);
Y = cross(Z,RHumerusAxis);
Col0 = RHumerusAxis./((sum((RHumerusAxis.^2),2)).^0.5);
```

```
Col1 = Y./((sum((Y.^2),2)).^0.5);
Col2 = Z./((sum((Z.^2),2)).^0.5);
RElbowAxis = NaN(length(Y),3);
for i = 1:length(Y)
    Rot = [Col1(i,:)' Col2(i,:)' Col0(i,:)'];
    tmp = Rot*[0; 1; 0];
    RElbowAxis(i,:) = tmp' + REJC(i,:);
end

% Left arm
LHumerusAxis = LSJC - LEJC;
LRadiusAxis = LEJC - LWJC;

Z = cross(LHumerusAxis,LRadiusAxis);
Y = cross(Z,LHumerusAxis);
Col0 = LHumerusAxis./((sum((LHumerusAxis.^2),2)).^0.5);
Col1 = Y./((sum((Y.^2),2)).^0.5);
Col2 = Z./((sum((Z.^2),2)).^0.5);
LElbowAxis = NaN(length(Y),3);
for i = 1:length(Y)
    Rot = [Col1(i,:)' Col2(i,:)' Col0(i,:)'];
    tmp = Rot*[0; 1; 0];
    LElbowAxis(i,:) = tmp' + LEJC(i,:);
end

%% Shoulder angles

%Right arm
X = ThoraxBack;
Y = ThoraxRight;
Z = cross(X,Y);
Y = cross(Z,X);
ThoraxCol0 = X./((sum((X.^2),2)).^0.5);
ThoraxCol1 = Y./((sum((Y.^2),2)).^0.5);
ThoraxCol2 = Z./((sum((Z.^2),2)).^0.5);

X = RHumerusAxis;
Y = RRadiusAxis;
Z = cross(X,Y);
Y = cross(Z,X);
RUArmCol0 = X./((sum((X.^2),2)).^0.5);
RUArmCol1 = Y./((sum((Y.^2),2)).^0.5);
RUArmCol2 = Z./((sum((Z.^2),2)).^0.5);
LastValue = [0; 0; 0];
RShoulderAngle = NaN(length(Y),3);
for i = 1:length(Y)
    PosMat = [ThoraxCol0(i,:)' ThoraxCol1(i,:)' ThoraxCol2(i,:)'];
    Rot = [RUArmCol1(i,:)' RUArmCol2(i,:)' RUArmCol0(i,:)'];
    R = PosMat\Rot;
    Euler = NaN(3,1);
    Euler(3) = SafeArcsin(R(2,1));
    if (abs(cos(Euler(3))) > eps('single')*10)
        Euler(1) = atan2(-R(2,3), R(2,2));
        Euler(2) = atan2(-R(3,1), R(1,1));
    else
        if (Euler(3)>0)
```

```
            Euler(2) = atan2(R(3,2), R(3,3));
        else
            Euler(2) = -atan2(R(3,2), R(3,3));
        end
        Euler(1) = 0;
    end
    if (sum(abs(Euler)) > eps('single'))
        AnAngle = [Euler(2); Euler(1); Euler(3)];
        AnAngle = WrapEulerTo(AnAngle,LastValue);
    else
        AnAngle = Euler;
    end
    LastValue = AnAngle;
    RShoulderAngle(i,:) = AnAngle';
end

%Left arm
X = LHumerusAxis;
Y = LRadiusAxis;
Z = cross(X,Y);
Y = cross(Z,X);
LUArmCol0 = X./((sum((X.^2),2)).^0.5);
LUArmCol1 = Y./((sum((Y.^2),2)).^0.5);
LUArmCol2 = Z./((sum((Z.^2),2)).^0.5);
LastValue = [0; 0; 0];
LShoulderAngle = NaN(length(Y),3);
for i = 1:length(Y)
    PosMat = [ThoraxCol0(i,:)' ThoraxCol1(i,:)' ThoraxCol2(i,:)'];
    Rot = [LUArmCol1(i,:)' LUArmCol2(i,:)' LUArmCol0(i,:)'];
    R = PosMat\Rot;
    Euler = NaN(3,1);
    Euler(3) = SafeArcsin(R(2,1));
    if (abs(cos(Euler(3))) > eps('single')*10)
        Euler(1) = atan2(-R(2,3), R(2,2));
        Euler(2) = atan2(-R(3,1), R(1,1));
    else
        if (Euler(3)>0)
            Euler(2) = atan2(R(3,2), R(3,3));
        else
            Euler(2) = -atan2(R(3,2), R(3,3));
        end
        Euler(1) = 0;
    end
    if (sum(abs(Euler)) > eps('single'))
        AnAngle = [Euler(2); Euler(1); Euler(3)];
        AnAngle = WrapEulerTo(AnAngle,LastValue);
    else
        AnAngle = Euler;
    end
    LastValue = AnAngle;
    LShoulderAngle(i,:) = AnAngle';
end

%% Elbow angles

%Right arm
```

```
X = RRadiusAxis;
Y = RElbowAxis;
Z = cross(X,Y);
Y = cross(Z,X);
RFArmCol0 = X./((sum((X.^2),2)).^0.5);
RFArmCol1 = Y./((sum((Y.^2),2)).^0.5);
RFArmCol2 = Z./((sum((Z.^2),2)).^0.5);
LastValue = [0; 0; 0];
RElbowAngle = NaN(length(Y),3);
for i = 1:length(Y)
    PosMat = [RUArmCol1(i,:)' RUArmCol2(i,:)' RUArmCol0(i,:)'];
    Rot = [-RFArmCol2(i,:)' RFArmCol1(i,:)' RFArmCol0(i,:)'];
    R = PosMat\Rot;
    Euler = NaN(3,1);
    Euler(1) = SafeArcsin(-R(2,3));
    if (abs(cos(Euler(1))) > eps('single')*10)
        Euler(2) = atan2(R(1,3), R(3,3));
        Euler(3) = atan2(R(2,1), R(2,2));
    else
        if (Euler(1)>0)
            Euler(2) = atan2(-R(1,2), R(1,1));
        else
            Euler(2) = -atan2(-R(1,2), R(1,1));
        end
        Euler(3) = 0;
    end
    if (sum(abs(Euler)) > eps('single'))
        AnAngle = [Euler(2); Euler(1); Euler(3)];
        AnAngle = WrapEulerTo(AnAngle,LastValue);
    else
        AnAngle = Euler;
    end
    LastValue = AnAngle;
    RElbowAngle(i,:) = AnAngle';
end

%Left arm
X = LRadiusAxis;
Y = LElbowAxis;
Z = cross(X,Y);
Y = cross(Z,X);
LFArmCol0 = X./((sum((X.^2),2)).^0.5);
LFArmCol1 = Y./((sum((Y.^2),2)).^0.5);
LFArmCol2 = Z./((sum((Z.^2),2)).^0.5);
LastValue = [0; 0; 0];
LElbowAngle = NaN(length(Y),3);
for i = 1:length(Y)
    PosMat = [LUArmCol1(i,:)' LUArmCol2(i,:)' LUArmCol0(i,:)'];
    Rot = [-LFArmCol2(i,:)' LFArmCol1(i,:)' LFArmCol0(i,:)'];
    R = PosMat\Rot;
    Euler = NaN(3,1);
    Euler(1) = SafeArcsin(-R(2,3));
    if (abs(cos(Euler(1))) > eps('single')*10)
        Euler(2) = atan2(R(1,3), R(3,3));
        Euler(3) = atan2(R(2,1), R(2,2));
    else
```

```
        if (Euler(1)>0)
            Euler(2) = atan2(-R(1,2), R(1,1));
        else
            Euler(2) = -atan2(-R(1,2), R(1,1));
        end
        Euler(3) = 0;
    end
    if (sum(abs(Euler)) > eps('single'))
        AnAngle = [Euler(2); Euler(1); Euler(3)];
        AnAngle = WrapEulerTo(AnAngle,LastValue);
    else
        AnAngle = Euler;
    end
    LastValue = AnAngle;
    LElbowAngle(i,:) = AnAngle';
end

%% ExoJC
flag = input('Which trial are you analyze? \nPress 0 for FREE test or 1
for EXO test: ');

if flag == 1
    LEXOp = Trajectories(:,54:56);
    LEXOu = Trajectories(:,57:59);
    LEXOl = Trajectories(:,60:62);
    REXOp = Trajectories(:,63:65);
    REXOu = Trajectories(:,66:68);
    REXOl = Trajectories(:,69:71);
    LEXOp = filtfilt(b,a,LEXOp);
    LEXOu = filtfilt(b,a,LEXOu);
    LEXOl = filtfilt(b,a,LEXOl);
    REXOp = filtfilt(b,a,REXOp);
    REXOu = filtfilt(b,a,REXOu);
    REXOl = filtfilt(b,a,REXOl);

    R_Xexo = REXOu-REXOp;
    R_Zexo = cross(R_Xexo,REXOu-REXOl);
    R_Yexo = cross(R_Zexo,R_Xexo);
    R_Xexo = R_Xexo./((sum((R_Xexo.^2),2)).^0.5);
    R_Yexo = R_Yexo./((sum((R_Yexo.^2),2)).^0.5);
    R_Zexo = R_Zexo./((sum((R_Zexo.^2),2)).^0.5);

    RExoJC = NaN(length(R_Xexo),3);
    RSJC_exo = NaN(length(R_Xexo),3);
    for i = 1:length(R_Xexo)
         Rot =[R_Xexo(i,:); R_Yexo(i,:); R_Zexo(i,:)];
         tmp = Rot*REXOp(i,:)';
         RExoJC(i,:) = tmp - [100;6+(MarkerDiameter/2)+2;0];
    end

    L_Xexo = LEXOu-LEXOp;
    L_Zexo = cross(L_Xexo,LEXOu-LEXOl);
    L_Yexo = cross(L_Zexo,L_Xexo);
    L_Xexo = L_Xexo./((sum((L_Xexo.^2),2)).^0.5);
    L_Yexo = L_Yexo./((sum((L_Yexo.^2),2)).^0.5);
    L_Zexo = L_Zexo./((sum((L_Zexo.^2),2)).^0.5);
```

```
    LExoJC = NaN(length(L_Xexo),3);
    LSJC_exo = NaN(length(L_Xexo),3);
    for i = 1:length(L_Xexo)
         Rot =[L_Xexo(i,:); L_Yexo(i,:); L_Zexo(i,:)];
         tmp = Rot*LEXOp(i,:)';
         LExoJC(i,:)  = tmp - [145;6+(MarkerDiameter/2)+2;0];
    end
end
```

```
function T = markerrec(I,J,K,delta)

    u = I - J;
    v = K - J;
    w = cross(u,v);
    v = cross(w,u);
    u = u./((sum((u.^2),2)).^0.5);
    v = v./((sum((v.^2),2)).^0.5);
    w = w./((sum((w.^2),2)).^0.5);

    Rot =[u; v; w];
    tmp = Rot*J';
    tmp = tmp-delta';
    tmp = Rot'*tmp;
    T(1,:)=tmp';

end
```

```
function Result = Chord(PointI, PointJ,PointK,iS)

         IJ = PointI - PointJ;
         KI = PointK - PointI;
         S = IJ./((sum((IJ.^2),2)).^0.5);
         T = cross(cross(KI,S),S);
         T = T./((sum((T.^2),2)).^0.5);
         cosalfa = (iS./((sum((IJ.^2),2)).^0.5));
         l = iS .* cosalfa;
         m = ((iS*iS) - (l.*l)).^0.5;
         Result = NaN(length(m),3);
         for i = 1:length(m)
             tmp = (T(i,:)'*m(i)) - (S(i,:)'*l(i));
             Result(i,:) = PointI(i,:) + tmp';
         end

  end
```

```
function Angle = SafeArcsin(Value)
      if(abs(Value) > 1)
            Value = max([min([Value 1]) -1 ]);
      end
      Angle = asin(Value);
end
```

```
function OutputAngles = WrapEulerTo( InputAngles, Dest )
      a = InputAngles;
      b = InputAngles;
      [d,a] = FixEuler(Dest,a);
      b = b.*[1;-1;1] + pi;
      [f,b] = FixEuler( Dest, b );
```

```
	if(f < d)
		OutputAngles = b;
	else
		OutputAngles = a;
	end
end
```

```
function [Distance,Changed] = FixEuler(Dest,Curr)
	Changed = Curr + pi*2 * floor((Dest - Curr + pi)./(pi*2));
	Distance = max(abs(Dest - Changed));
end
```